ESCOLA NAVAL

talant de bien faire

José Filipe Rodrigues Mendes

Impact of Atmospheric Propagation Effects on the Performance of Pulse Compression Techniques for Radar Systems

A dissertation submitted in partial fulfillment of the requirements for the degree of Marine Military Sciences, specialisation of Engenharia Naval Ramo de Armas e Eletrónica

Alfeite

2021

José Filipe Rodrigues Mendes

Impact of Atmospheric Propagation Effects on the Performance of Pulse Compression Techniques for Radar Systems

A dissertation submitted in partial fulfillment of the requirements for the degree of Marine Military Sciences, specialisation of Engenharia Naval Ramo de Armas e Eletrónica

Orientation of: Prof. Dr. Paulo Alexandre Carapinha Marques
Co-orientation of: Prof. Dr. João Manuel de Almeida Monteiro Felício
Co-orientation of: CFR EN-AEL João Luís Reis Fidalgo Neves

The Master Student,

José Filipe Rodrigues Mendes

José Mendes

The Supervisor,

Paulo Marques

Alfeite

2021

"The only limit to our realization of tomorrow will be our doubts of today."
Franklin D. Roosevelt

To my parents and brothers, for always giving me all the strength and support I needed.

Acknowledgement

On the first place, I want to express my gratitude to my thesis' supervisors, Professor Paulo Marques, Professor João Felício and Engineer João Neves, for always being present and helping me with every doubt that arose in my path.

Thank to Instituto de Telecomunicações de Aveiro, for having provided the laboratory, material and all kinds of equipment so that the practical tests could be made.

Thank every single member of the work group from Instituto de Telecomunicações de Aveiro, that always supported me and suggest new ways to suppress my difficulties with the thesis. It was a great opportunity and a true honor to feel as an important member of this EUSST project.

Nevertheless, it makes all sense to express my distinctive grattitude to João Pandeirada, also member of the Instituto de Telecomunicações de Aveiro work group, which was always available to help me. Without his help, I certainly would not achieve such good results.

Then I want to thank my friends and comrades, Nabais Lopes, Moreira Bastos, Santos das Neves, Ferreira Fachina, Batalha Francisco, Simas Costa, Malta Ribeiro, Silva Piteira, Gomes Moreira, Santos Bretes, Faria Pereira, Cabanita Raimundo, Vale Gonçalves, Manuel Manjate, Almeida Monteiro, Bento Baltazar, Pereira Mateus, Santos Barata, Teixeira Marques, Cabral Simões, Saraiva Vanzeller, Nicau Martins, Rocha Araújo, José Mendes, Nuno Pereira, Francisco Soares, Filipe Rosa, Rafael Morim, Mykola Nebylovych and Paulo Gonçalves, for having always being cheering for me. My sucess will always have a important contribution from them.

Finally, I want to thank my family for always supporting me on an unending way, giving me the strength I need to always keep on moving, no matter what the difficulties. I would never be who I am today without them.

Abstract

Currently, more than three tons of space debris are an integrate part of the low earth orbit, and exhibit a trend to increase, due to collisions and the constant inoperability of older satellite systems. The technological era that we are living, in which satellites are a major element of any Telecommunications service, it is necessary to make a sustainable use of Space, so that technology can keep improving.

The European Space Surveillance and Tracking support framework has as its main objective the catalogue and prediction of space debris' orbits, as a non-active approach to the space debris problem. The rAdio TeLescope pAmpilhosa Serra (ATLAS) is incorporated on this framework, giving Portugal the capability of performing space debris detection and tracking.

The main objective of this thesis was the creation of an Earth-space propagation simulator with frequency agility, so that it would be possible to simulate the propagation of many radar signals originated through pulse compression techniques and thus be able to quantify the impact of atmospheric propagation on its efficiency.

To prove the profitability of using these techniques, two types of tests were carried out: a test using the ATLAS radar receiver circuit, providing a familiarization with this type of systems and afterwards, the obtainment of True Positive Rate curves, where it was demonstrated the high target detention capability when using pulse compression techniques compared to unmodulated radar pulses, mainly with very low SNR around -20dB.

Keywords: Space Debris, Pulse Compression, Radar, Atmospheric Propagation

Resumo

Atualmente, mais de três toneladas de detritos espaciais são parte integrante da órbita baixa da Terra, apresentando uma tendência de aumento, devido à constante obsolescência de satélites mais antigos e possíveis colisões entre os mesmos. Na era tecnológica em que vivemos, em que os satélites são um elemento importante de qualquer serviço de telecomunicações, torna-se necessário fazer um uso sustentável do espaço, para que a tecnologia continue a evoluir.

A estrutura europeia de apoio à vigilância e rastreamento espacial (EUSST) tem como principal objetivo a catalogação e previsão das órbitas dos detritos espaciais, sendo por isso considerada com uma abordagem não ativa de combate aos detritos espaciais. O rAdio TeLescope pAmpilhosa Serra (ATLAS) está incorporado nesta estrutura, proporcionando a Portugal a capacidade de realizar deteção e rastreamento de detritos espaciais.

O principal objetivo desta tese passa pela criação de um simulador de propagação Terra-espaço, com agilidade em frequência, de forma a ser possível simular a propagação de vários sinais radar originados a partir de técnicas de compressão de impulsos, sendo assim capaz de quantificar o impacto da propagação atmosférica na eficiência dos mesmos.

Para comprovar a rentabilidade do uso destas técnicas, foram realizados dois tipos de testes: um teste utilizando o circuito recetor do radar ATLAS, proporcionando uma familiarização com este tipo de sistemas e, posteriormente, a obtenção das curvas de percentagem de verdadeiros positivos, onde foi demonstrado a elevada capacidade de deteção de alvos ao utilizar técnicas de compressão de impulsos em comparação com impulsos de radar não modulados, principalmente para valores de SNR muito baixos, sensivelmente em torno de -20dB.

Palavras-chave: Detrito Espacial, Compressão de Impulsos, Radar, Propagação Atmosférica

Contents

List of Figures

List of Tables

List of Equations

List of Symbols

L_{br}	radar free-space transmission loss	dB
σ	target radar cross-section	m^2
d	distance between the radar and the target	km
f	signal frequency	Hz
γ	specific gaseous attenuation	dB/km
γ_o	specific oxygen attenuation	dB/km
γ_w	specific water vapour attenuation	dB/km
N''_{Oxygen}	oxygen frequency-dependent complex refractivities imaginary part	
$N''_{WaterVapour}$	water vapour frequency-dependent complex refractivities imaginary part	
S_i	strength of the oxygen and water vapour spectral line	
F_i	oxygen and water vapour spectral line shape imaginary factor	
f_i	spectral line frequency	
Δf	width of the oxygen and water vapour spectral line	
δ	oxygen spectral line correlation factor	
N''_D	dry air continuum due to pressure-induced nitrogen attenuation imaginary part	
d_s	Debye spectrum's width parameter	
φ	specific gaseous phase dispersion	deg/km
φ_o	specific oxygen phase dispersion	deg/km
φ_w	specific water vapour phase dispersion	deg/km
N'_{Oxygen}	oxygen frequency-dependent complex refractivities real part	
$N'_{WaterVapour}$	water vapour frequency-dependent complex refractivities real part	
F'_i	oxygen and water vapour spectral line shape real factor	
N'_D	dry air continuum due to pressure-induced nitrogen absorption real part	
ΔL	exceeding radio path length	m

s	length of propagation path	m
n_e	electron concentration	$\mathrm{el/m^3}$
θ	Faraday angle of rotation	rad
B_{av}	Earth magnetic field	$\mathrm{Wb \cdot m^2}$ or T
N_T	Total Electron Content	$el \cdot \mathrm{m^{-2}}$
t	group delay	s
n	refractive index	
N	radio refractivity	
p	dry air pressure	hPa
e	water vapour partial pressure	hPa
T	temperature	K
h	height	km
ρ	water vapour density	$\mathrm{g\,m^{-3}}$
P_t	peak transmission power	W
G	antenna gain	
λ	signal wavelength	m
M	total number of integrated pulses	
m	number of integrated pulses	
$e(m)$	efficiency of pulse integration	
F	propagation loss factor	
R	target distance	m
N_F	receiver noise factor	
k	Boltzmann constant	$\mathrm{J\,K^{-1}}$
T	receiver temperature	K
B	receiver bandwidth	Hz
L_s	system loss factor	
SNR	signal-to-noise ratio	dB

List of Acronyms

AF	Ambiguity Function.
AQS	Acquisition Board.
ATLAS	rAdio TeLescope pAmpilhosa Serra.
AUC	Area Under the Curve.
AWG	Arbitrary Waveform Generator.
BIRALES	BIstatic RAdar for Leo Survey.
BIRALET	BIstatic RAdar for LEo Tracking.
COPUOS	Committee on the Peaceful Uses of Outer Space.
CW	Continuous Wave.
EISCAT	European Incoherent Scatter Scientific Association.
EU	European Union.
EUSST	European Space Surveillance and Tracking.
FFT	Fast Fourier Transform.
FGS	Fundamental Geodetic Stations.
FPR	False Positive Rate.
GEO	Geosynchronous Earth Orbit.
GESTRA	German Experimental Surveillance and Tracking Radar.
GPS	Global Positioning System.
GUI	Graphical User Interface.
HPBW	Half-Power Beamwidth.

ICT	Information and Communication Technologies.
IDAC	Inter-Agency Space Debris Coordination Committee.
IDE	Integrated Development Environment.
IF	Intermediate Frequency.
IFFT	Inverse Fast Fourier Transform.
IT	Instituto de Telecomunicações.
ITU	International Telecommunication Union.
ITU-R	International Telecommunication Union Radiocommunication Sector.
LEO	Low-Earth Orbit.
LFM	Linear Frequency Modulated.
LNA	Low Noise Amplifier.
LPI	Low Probability of Intercept.
LTI	Linear Time Invariant.
OCXO	Oven-Controlled Crystal Oscillator.
PACF	Periodic AutoCorrelation Function.
PAF	Periodic Ambiguity Function.
PRF	Pulse Repetition Frequency.
PRI	Pulse Repetition Interval.
PSLR	Peak-to-peak SideLobe Ratio.
RAEGE	Rede Atlântica de Estações Geodinâmicas e Espaciais.
RCS	Radar Cross Section.
ROC	Receiver Characteristic Operator.
SBC	Single Board Computer.
SNR	Signal-to-Noise Ratio.
SRT	Sardinia Radio Telescope.
SST	Space Surveillance and Tracking.
TEC	Total Electron Content.

TIRA	Tracking and Imaging Radar.
TPR	True Positive Rate.
TRF	Radio Frequency Transmitter.
UN	United Nations.

Chapter 1

Introduction

Decades ago, it was difficult to predict how space usage would evolve through all these years, because the knowledge about the conditions or its potential were far insufficient. A practical outer space industry was proven to be possible and highly profitable in 1965, based on Arthur Charles Clarke's conceptualization of communication satellites in Geosynchronous Earth Orbit (GEO). Nowadays, more than half a century later, every technology that we use and know, even the most present in our daily routine, just like the Global Positioning System (GPS), are depending on a space without accidents or any kind of event that could affect a satellite and consequently affect the related service.

The truth is in fact very clear, space systems turned out to be essential to our community, so essential that if suddenly a catastrophic phenomenon occurred and all our space-based technologies (like for navigation, weather forecasting, civil and military communications as many others) failed, we would probably witness the occurrence of diversified criminal events and harmful effects on many domains like economy, military and even socially.

1.1 Space Debris

Unfortunately, our satellites are increasingly at risk because of several factors including natural causes like the extreme solar flares and coronal mass ejections, but also because of human contribution, reflected on space debris, which is defined as being all man-made objects in Earth orbit or re-entering, including elements and fragments originated by those same objects, considered as being non-functional [2].

On an endeavor to reduce the creation of more space debris, specific guidelines were published by the Inter-Agency Space Debris Coordination Committee (IDAC) and by the United Nations (UN) Committee on the Peaceful Uses of Outer

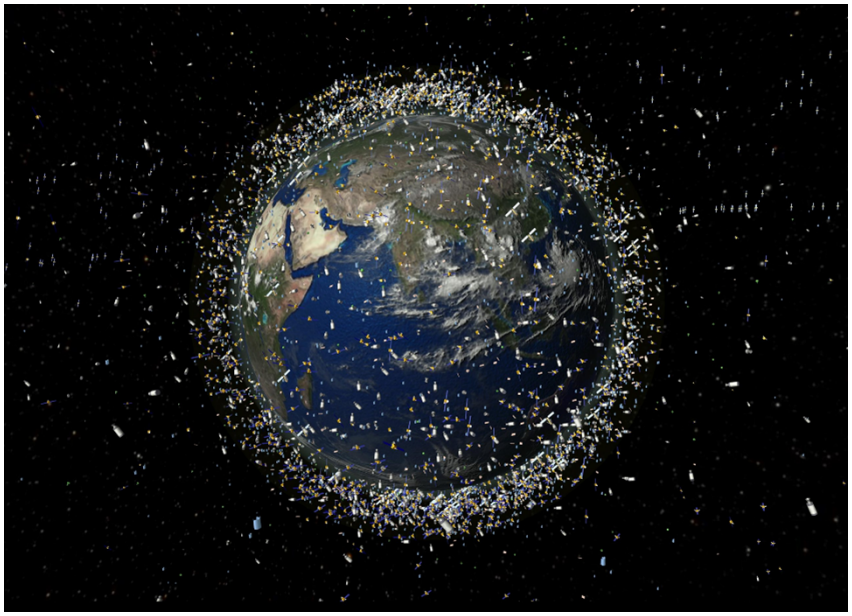

FIGURE 1.1: Satellites on Low-Earth Orbit.
Source: obtained from [1]

Space (COPUOS). Although these guidelines [2] are not the main subject for this dissertation, it is important to quote them:

- Guideline 1: Limit debris released during normal operations – Every space system should be designed on a way that ceased or at least cutted down the releasing of debris throughout normal operations.
- Guideline 2: Minimize the potential for break-ups during operational phases – Launch vehicles and spacecrafts orbital stages may be planned on a way to extinguish accidental break-ups or at least have disposal and passivisation measures to avoid them.
- Guideline 3: Limit the probability of accidental collision in orbit – During the development of the design and mission profile of spacecraft and launch vehicle stages, has to be considered the probability of accidental collisions with known objects during its launch phase and orbital lifetime on an endeavor to minimize those collisions.
- Guideline 4: Avoid intentional destruction and other harmful activities – Detrimental activities or even intentional destruction of any spacecraft and launch vehicles during its launch phase or orbital lifetime, which would produce long-lived debris, must be avoided.
- Guideline 5: Minimize potential for post-mission break-ups resulting from

stored energy – Every on-board source of accumulated energy should be depleted or kept on a safe way when no longer needed for mission operations or post-mission disposal, on an effort to reduce the risk of accidental break-ups to other spacecrafts and launch vehicles.

- Guideline 6: Limit the long-term presence of spacecraft and launch vehicle orbital stages in the Low-Earth Orbit (LEO) region after the end of their mission – After finishing operational phases in orbits that intercept LEO region, spacecrafts and launch vehicles should be removed from orbit in restrained way.
- Guideline 7: Limit the long-term interference of spacecraft and launch vehicle orbital stages with the GEO region after the end of their mission – Spacecraft and launch vehicle orbital stages that have finished their operational phases in orbits that intercept GEO must be kept far away from them in a strategy to minimize long-term interference.

These guidelines are limited and do not guarantee that orbital debris build up would not expand drastically, something that could result on disastrous consequences.

Just to have a quick outlook of the current situation, there are more than six tons of space debris, which approximately 45 % of them are in LEO and polar orbits. In addition to this, it is unavoidable the increasing risk of collisions in between the many satellites in orbit, what could in some way create an exponential growth of space debris. Analyzing now two specific cases from recent years [3], one of them being the collision of the inoperative Russian weather satellite Cosmos 2551 with the active LEO mobile communications satellite Iridium 33, in February of 2009, that had created around 1300 of space debris items [4]; the other one is the intentional destruction of the defunct Chinese weather satellite Fen Yun by the Chinese military, in January of 2007, that were testing the efficiency of anti-satellite missile, regardless of creating something like 2800 space debris items [4].

This problematic is so important that if space debris would ever achieve such colossal proportion and consequently make a sufficiently dense layer in space, it would not even be secure to launch a spacecraft considering the risk of being hit and seriously damaged.

Consequently, efforts have been made to develop projects for space debris active removal (Figure 1.2), which are relied on state-of-the-art space technologies, being obviously tremendously expensive, slow and hence very inefficient. All of

these techniques and projects that were already applied over the past years using diversified capturing methods, among which are tentacles, net capturing, tether grippers, harpoons, among others [5]. Although being obviously important, these projects and techniques will not be subject of focus in the extent of this dissertation, instead the emphasis will rely on ground-based approaches for collision avoidance.

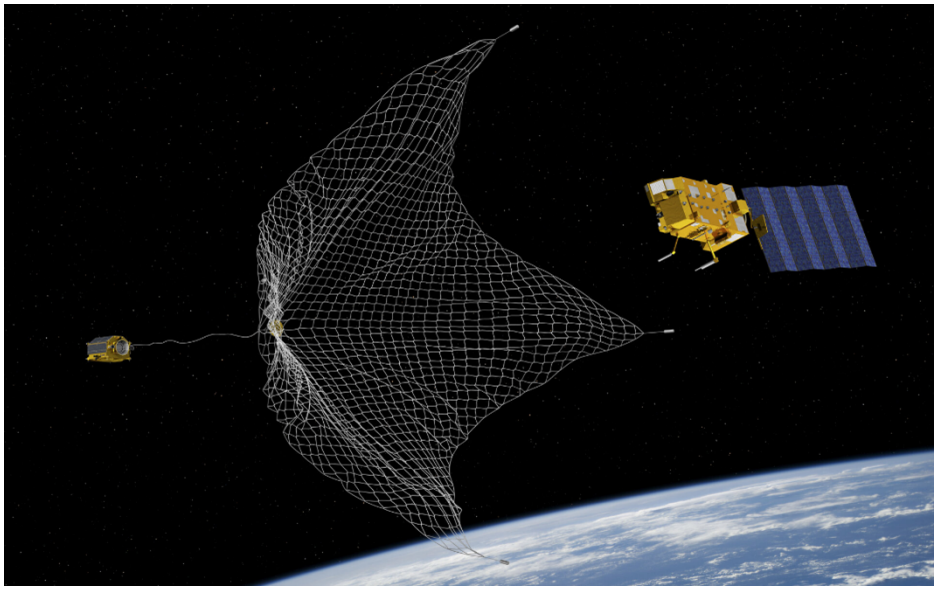

FIGURE 1.2: Active space debris removal using a net.
Source: obtained from https://www.esa.int/

1.2 Ground-Based Approaches for Collision Avoidance

A capable and efficient ground-based network of sensors is indispensable for space surveillance and hence preventing new collisions to occur, that is why European Space Surveillance and Tracking (EUSST) Support Framework was established in 2014, by the European Union (EU) [6]. Afterwards it was also created a Space Surveillance and Tracking (SST) Consortium with the participation of five EU member states, which were United Kingdom, Italy, Germany, France and Spain, with Portugal, Romania and Poland joining four years later. A SST capability acknowledges a high performance detection, catalogue and prediction of orbits from space objects of any kind.

To achieve these main objectives in terms of performance, it is imperative to have a great network of sensors in terms of quantity and also in quality, which have to be capable of accurately determine the state of the orbiting space objects. For

that reason, the EUSST already incorporates 51 sensors including radars, telescopes and laser ranging stations, whose main purpose is to survey and track space objects in all orbital regimes.

Our centre of attention will be directed toward radars, whose main features and advantages, in comparison to telescopes, is to be available to perform its task 24 hours a day, being much less affected by meteorological conditions and are able to perform with very high sensitivity.

1.3 Motivation and Objectives

The main objective of this dissertation is the development of an Earth-space propagation simulator, which it is capable of evaluate the impact of atmospheric propagation in radar pulses. Every considered phenomenon has its origin on the atmosphere, ionosphere, troposphere and free-space propagation attenuation. There is also a incorporation of pulse compression techniques with the goal of directly evaluate the impact of propagation on radar systems, providing a worthy estimation of the expected signal-to-noise ratio of a real target detection, considering the natural environment used during the simulation, proving that way the efficiency of pulse compression techniques in radar systems.

It is also be necessary to consider the importance of these topics in terms of national defense. For the armed forces be able to exercise their functions, there must be a situational awareness of everything that surrounds them, whether in land, sea, air and even space, as shown in figure 1.3. Therefore, by having radar systems capable of perform space debris detection and tracking, the armed forces are able to obtain situational awareness and control of every object and potential threat that is located hundreds of kilometers above the national territory.

FIGURE 1.3: Situational awareness representation.
Source: obtained from https://blog.usni.org/

1.4 Thesis Organization

This dissertation is divided into 5 chapters, with chapter 1 being the introduction. In chapter 2 it is intended to introduce some analytical background related with radar systems, such as European radar systems currently in operation and pulse compression techniques. Chapter 3 is devoted to the development of the Earth-space propagation simulator, where every used function is described and all interconnections between scripts inside the simulator are explained. In the following chapter, are performed tests to the Earth-space propagation simulator. Firstly, by carrying out several simulations in which the propagation conditions are sequential changed, what will influence the shape of the received signal. This received signal, without the addition of any noise, is saved and then injected into the radar receiver circuit, using attenuators to obtain the previously calculated Signal-to-Noise Ratio (SNR) for each of these simulations, which possibilities a familiarization with the radar and the opportunity to correlate the signal taken from the radar receiver circuit, with the one that is initially transmitted in the simulator. Afterwards, True Positive Rate curves will also be calculated, which will demonstrate the efficiency of the use of pulse compression techniques in radar systems, especially for very low values of SNR, around -20 dB. Finally, chapter 5 aims to the discussion of results obtained on the previous tests and the conclusions to be extracted from the dissertation.

Chapter 2

Analytical Background

2.1 Propagation Simulators

Developing a propagation simulator is not a trivial task, reality that is supported on the fact that so few simulators examples exist, and even the existing ones do not emphasize radar pulses propagation with all the capabilities that we search for this simulator.

Nevertheless, there was one that stood out for its references and functionality, which was ITU-Rpy [7]. The main task of this simulator is to evaluate the attenuation that a electromagnetic wave undergoes during its propagation through slant or horizontal paths in the atmosphere.

This simulator takes into consideration the attenuation originated by free-space propagation, atmosphere and even by periodic events like rain, clouds, etc. On the other hand, it has a critical weakness, related to the fact that all phenomena are just computed for a single frequency, forbidding the possibility of analysing the propagation effects for a wide bandwidth, which is a needed feature in order to simulate the propagation of signals modulated making use pulse compression techniques. Therefore, with the development from scratch of this new Earth-space propagation simulator, this frequency agility will be now available.

2.2 Radar Fundamental Concepts

Before entering directly into some examples, it is important to have a brief review of some features to have in consideration during the conceptualization and development of radar systems [8]. The main property to be considered is the antenna radiation pattern that is defined as a graphical or mathematical representation of the antenna's radiation properties, which include the radiation intensity, power flux

density, field strength, directivity, polarization or phase. Plotting the radiation pattern is a useful way to easily visualize the radar main and side lobes, being the main lobe the one that carries most of the energy radiated on a certain direction, and then the side lobes being the ones that carry some residual energy. It is important to refer that on a perfect but impossible scenario, side lobes should not exist. Other characteristic that is easy to visualize through the radiation pattern and has a key role on a radar system for this purpose is the antenna beamwidth or Half-Power Beamwidth (HPBW). For a better perception of this phenomenon, look over figure 2.1. Briefly, the antenna beamwidth is defined as the angular aperture between two identical half-power points, which have half the power (which corresponds to -3dB) relatively to the maximum power value of the main lobe. To have an exceptionally precise system it is fundamental to have the slightest antenna beamwidth possible.

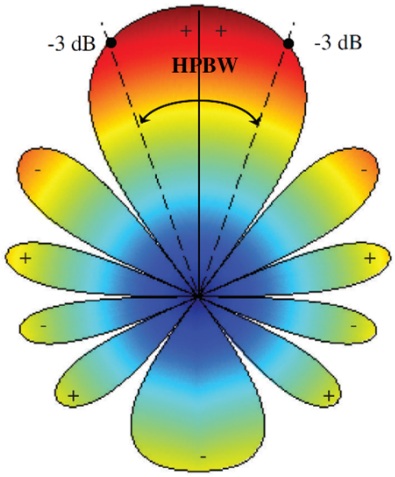

FIGURE 2.1: HPBW representation.
Source: obtained from [8]

Antennas are also characterized by their directivity, which is defined as the ratio of the radiation intensity that is radiated on the main lobe direction to the radiation intensity averaged over all directions of propagation. To design antennas with very large directivities, which would obviously benefit the radar tracking capabilities, it is essential to conceptualize antennas with a higher electrical size, which can be defined as a ratio between the antenna dimension and the pulse wavelength.

Another helpful characteristic that classifies the antenna performance is the gain, that is defined as being the ratio between the radiation intensity on the direction that corresponds to the main lobe and the radiation intensity that would be obtained if the antenna radiated the power isotropically. Although being closely related to directivity, is a parameter that measure the efficiency of the antennas as well its directional capabilities.

After all, the last figure-of-merit to be mentioned is the polarization. The polarization of an antenna is defined as being the polarization of the electromagnetic wave radiated by the antenna, which is defined as being a property of an electromagnetic wave that describes the direction and relative magnitude of the electric-field vector variation in time.

2.2.1 EUSST Radars

We will now introduce some radars that are included in the EUSST sensor network and their main characteristics [9] [10]. Starting off with the European Incoherent Scatter Scientific Association (EISCAT)[11], shown in figure 2.2, that is constituted by three distinct sites: the monostatic VHF radar operating at 224 MHz, located in Tromsø (Norway); the monostatic double antenna EISCAT Svalbard radar operating at 500 MHz, located in Longyearbyen (Svalbard); and the tristatic UHF EISCAT radar, with its transmitter located in Tromsø and its three receivers, one of them in the same location, one at Kiruna (Sweden) set apart 206 kilometers from the transmitter, and the other one in Sodankylä (Finland) set apart 398 kilometers from the transmitter.

FIGURE 2.2: EISCAT radar system.
Source: obtained from
https://www.linkedin.com/company/eiscat-scientific-association

Germany have also its radar located near Bonn called Tracking and Imaging Radar (TIRA), which is a powerful pulsed bistatic radar used as transmitter, and Max-Planck-Institute Effelsberg Radio Telescope used as the receiver [9]. The system operates at 1.333 GHz (L-band), being capable of detect space objects with a minimal size of 1 centimeter. On a monostatic configuration, has the capability

of detect objects down to 2 centimeters at a range of 1000 kilometers. It is also important to refer the transmitter peak power of 1 MW, with an antenna gain of 49.7 dB and a antenna beamwidth of 0.50º.

Germany it is also working on the development of a close monostatic pulsed phased array named German Experimental Surveillance and Tracking Radar (GESTRA) [9] [12], operating in L-band between 1280 MHz and 1400 MHz, with a peak power of more than 1 kW and the capability of performing digital beamforming, on an endeavour to improve observation and detection of space objects up to 3000 kilometers altitude.

At last, mention also two Italian radars, the BIstatic RAdar for LEo Tracking (BIRALET) and the BIstatic RAdar for Leo Survey (BIRALES), both being the receivers of each radar system, but using the same transmitter designated as Radio Frequency Transmitter (TRF) based in Sardinia (Figure 2.3) [9]. TRF have a 7 meters diameter dish parabolic antenna, which operates in Continuous Wave (CW) mode, being able to achieve a continuous peak power of 14 kW, in the bandwidth between 410 MHz and 415 MHz, exhibiting an antenna gain close to 27 dBi.

FIGURE 2.3: TRF radar antenna.
Source: obtained from https://www.researchgate.net/

BIRALES uses as a receiver a section of the Northern Cross radio telescope (Figure 2.5), located 580 kilometers apart from TRF in Bologna, which is capable of monitoring the space environment in survey mode and simultaneously, making the most of a multi-beam configuration, measure space objects characteristics like its

EUSST Radars					
Radar System	Operating Frequency	Operating Bandwidth	Peak Power	Antenna Gain	Waveform type
EISCAT	930 MHz	-	1.5 kW	48.1 dBi	Pulsed
TIRA	1.333 GHz	250 kHz	1 MW	49.7 dBi	Pulsed
GESTRA	1340 MHz	120 MHz	> 1 kW	-	Pulsed
BIRALET	412.5 MHz	5 MHz	14 kW	27 dBi	Continuous
BIRALES	412.5 MHz	5 MHz	14 kW	27 dBi	Continuous

Table 2.1: EUSST Radars.
[9] [12]

Doppler shift, SNR and estimate its orbit. It is also important to refer that because of the CW configuration, it is not possible to measure the space object range.

Figure 2.4: BIRALES receiver antennas.
Source: obtained from https://www.semanticscholar.org/

On the other hand, BIRALET system uses the Sardinia Radio Telescope (SRT) as a mono-beam P-band receiver, set apart only by 20 kilometers, being appropriate to measure Doppler shifts and the received SNR in tracking mode, being now used for space debris monitoring.

The BIRALET system, based on its available receivers (Figure 2.5), can operate on diverse range of frequencies such as between 305 MHz and 410 MHz (P-band), between 1300 MHz and 1800 MHz (L-band), between 5.7 GHz and 7.7 GHz and between 18 GHz and 26.5 GHz, being receivers for others ranges of frequency under development.

In table 2.1 it is shown a summary with the characteristics of the referred radars.

FIGURE 2.5: BIRALET receiver antenna on a bistatic configuration.
Source: obtained from https://www.researchgate.net/

2.3 Pulse Compression Techniques

When developing a radar system, the engineers must have in consideration the hardware features and limitations, which will affect the efficiency and performance of the radar. On a conceptual way, every engineer already knows what type of pulse he would like to transmit in order to have the best detection possible. On time domain, it would be a pulse that went from zero to maximum power and back down again instantaneously, usually designated as a *delta dirac*, originating an infinite frequency spectrum, which is impossible to achieve considering the existing hardware.

It is true that the efficiency of detection is directly connected, in most cases, to the pulse's energy compared to the receiver's thermal noise level, but it is also true that the pulse waveform performance is closely connected with its ambiguity function, accuracy and resolution that the radar can perform while determine the range and radial velocity of the object. These two values can be obtained from the received signal, whereas range is related to the delay of the received signal and the radial velocity to the Doppler shift [13].

The object range is given by the relation between time and propagation velocity, expressed by $\frac{\Delta t_{propagation} \times c}{2}$, with c being the velocity of propagation of light on vacuum, considering that the pulse has to reach the target and then go back to the receiver. It is also important to highlight that the propagation velocity is not

constant along the path, being influenced by the atmosphere and its characteristics.

On the other hand, Doppler shift is defined as being the difference between the received frequency and the transmitted frequency. If this difference has a positive value, it means that the target is approaching the radar at a certain velocity, otherwise if the value is negative, it means that the target is moving away from the radar at a certain velocity.

In radar systems, the radiated signal is never constituted by just only one pure harmonic (with a well-defined frequency), instead the signal has frequency components with different amplitudes, along a certain bandwidth, in order to be able to apply pulse compression techniques and increase its detection efficiency. For Doppler shift measurements, it is important to evaluate if a signal has a narrowband or wideband; the most used rule to evaluate if a bandwidth is narrow or wide is seeing if it has less than one-tenth of the carrier frequency, which being the case it means that it is considered as a narrowband and the Doppler measurement can be calculated by using only the carrier frequency. On the other hand, if the signal has a wideband, other factors should be considered, such as time scaling (changing the signal sampling rate due to the wide range of frequencies [14]).

2.3.1 Matched Filters

It is important to have in mind that in every radar system, a pulse is radiated by a transmitter to the receiver via a propagation channel. This channel modifies the initial pulse with a white Gaussian noise, distributed by all frequencies equally. To overcome this fact, one of the biggest features that is used is the matched filter [13]. The matched filter job is to maximize the SNR, increasing that way the probability of the receiver to be able to distinguish the detection of a target from the propagation channel noise. Its designing is relatively simple, being the time-inverted and delayed complex-conjugate of the signal envelope, for which is being designed. In figure 2.6, it is possible to visualize how a matched filter h(t) would look like for a given signal s(t).

After receiving and convolution the pretended signal (plus the unwanted Gaussian white noise) through the matched filter (characterized by its own transfer function), the SNR will be maximized at its output. This improvement can be calculated on a theoretical way by making the correlation of the expected received signal with the matched filter, resulting on a SNR equal to $2E/N_0$, being E the power of the received signal and N_0 the power of the white Gaussian noise.

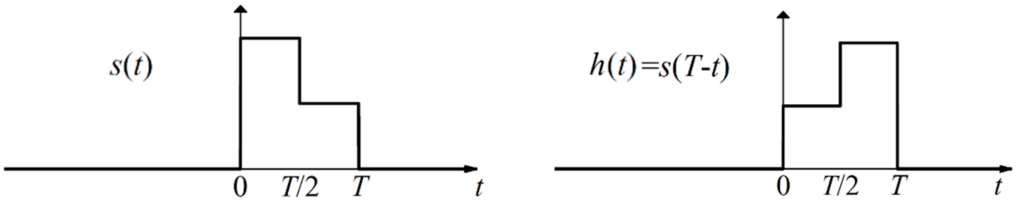

FIGURE 2.6: Matched filter representation.
Source: adapted from [13]

2.3.2 Ambiguity Function

The Ambiguity Function (AF) (Figure 2.7) is the graphical representation of the time response of a given finite energy signal with its matched filter, having the signal a delay and a Doppler shift associated to it [13].

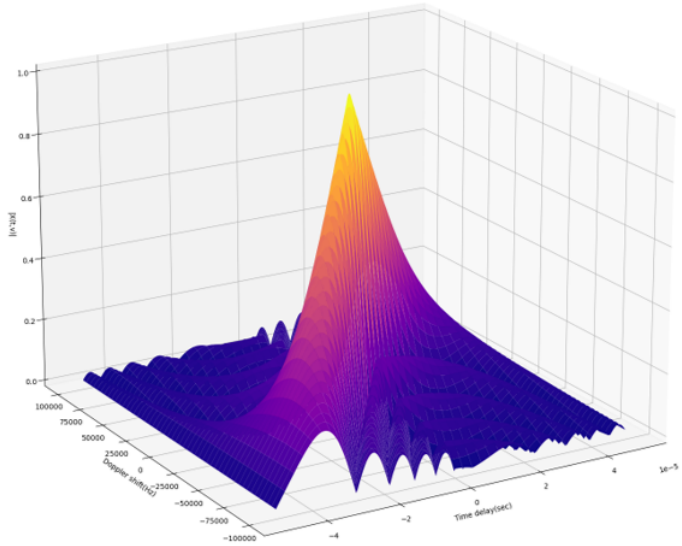

FIGURE 2.7: Ambiguity function of an LFM pulse.

The AF properties[13] are:

- Maximum at (0,0) – The amplitude of the AF can nowhere be higher than for delay and Doppler shift equal to zero.
- Constant volume – The volume under the normalized AF surface (squared) is always equal to one.
- Symmetry with respect to the origin – When plotting the AF, it is noticeable that there is a perfect symmetry regarding the origin point.
- Linear Frequency Modulated (LFM) effect – Attaching a LFM leads to the formation of a ridge passing from the first quadrant to the third quadrant of the

delay-Doppler space (for a positive LFM slope ($k > 0$, where k is a modulation constant)). This results on the AF being sheared, shifting the coordinate of maximum delay from zero Doppler to $k \cdot \tau$ Doppler, improving the delay resolution (figure 2.8). This also indicates that when determining the target range, a positive error will occur, giving the impression of the target being farther than it really is, resulting also on a lower closing velocity (negative Doppler).

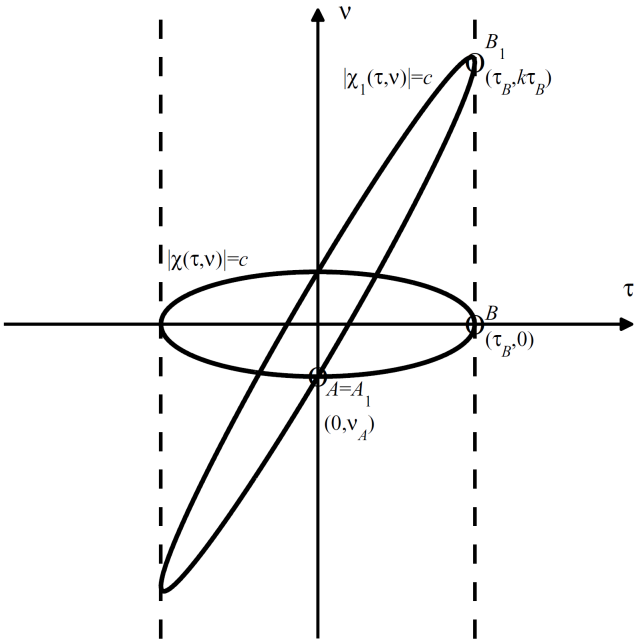

FIGURE 2.8: LFM shearing effect on the AF.
Source: obtained from [13]

The AF with ideal characteristics would exhibit a single sharp peak at the origin and have its level the closest to zero possible. With this AF pattern, after receiving the signal reflected from a target, we would have an undoubtedly determination of the target Doppler shift and delay, it would only be necessary to analyse in what coordinates would that sharp peak be. Furthermore, because of the near-zero level at every other points apart from the origin, there would be no sidelobes to undercover some other targets, which could have a smaller Radar Cross Section (RCS) or be at a higher distance, resulting on a peak with a meaningful lower level.

2.3.3 Main Radar Signals

Most modern pulse radar use pulse compression techniques to maximize their performance [13]. These techniques main purpose is to achieve pulses with

higher time-bandwidth products (energy) compared to unmodulated pulses (Figure 2.9), meaning that for the same bandwidth it is possible to get pulses with a lower duration in time, resulting on a higher range resolution without giving up on maximum range.

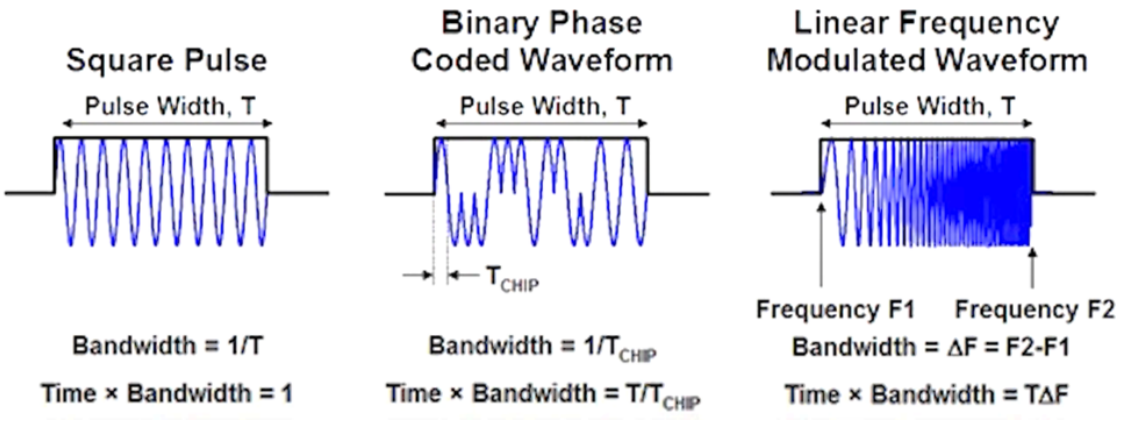

FIGURE 2.9: Time-Bandwidth product comparison.
Source: adapted from https://www.youtube.com/watch?v=PmEHxluUWuc

After understanding all these key concepts, it is important to analyse also the most used radar signals, in order to know what type of pulse would benefit more our particular case, studying all the advantages and disadvantages that each one of them has to offer.

Unmodulated Signal

Preliminary to analyse the signals produced by pulse compression techniques, we will briefly refer why an unmodulated pulse cannot perform good enough as a radar system signal. The first factor is exactly related to the signal energy, as the unmodulated pulse has only a $Time \times Bandwidth = 1$, as shown in figure 2.9; The other factor is the velocity resolution V_{null}, characterized by the value where the Doppler shift equals to zero for the first time, given by

$$V_{null} = \frac{1}{T} \cdot \frac{c}{2 \cdot f_c} \ . \tag{2.1}$$

For a pulse with $T = 5\mu s$ and $f_c = 5.56GHz$ would exhibit a $V_{null} = 5.4 km\,s^{-1}$, covering a high variety of velocity values, which could represent targets from terrestrial objects till satellites, which is clearly not acceptable. Reasonable range resolution can be achieved using pulse compression techniques, likewise velocity resolution can be achieved using a coherent pulse train.

Linear Frequency Modulated Signal

Starting off with the most common pulse compression technique, the LFM pulse 2.10, also known as chirp. Its concept is to linearly shift the signal frequency, during the pulse duration T, along a established bandwidth B. The complex envelope of the LFM pulse [13] can be characterized by

$$u_N(t) = \frac{1}{\sqrt{T}} rect\left(\frac{t}{T}\right) exp(j\pi k t^2), \quad where \quad k = \pm\frac{B}{T} \ . \tag{2.2}$$

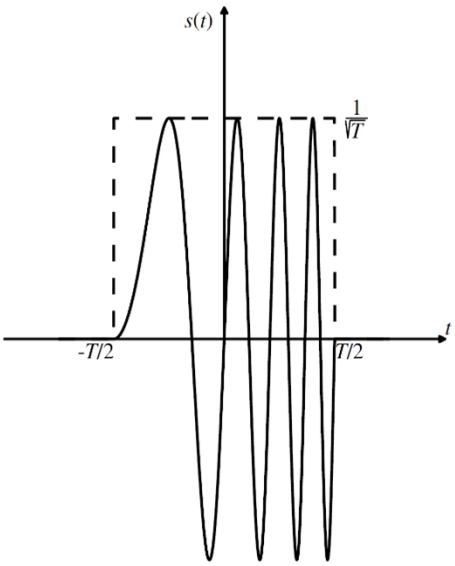

FIGURE 2.10: Linear frequency modulated signal.
Source: obtained from [13]

The frequency slope k (s^{-2}) is a relevant value, being used to calculate the time-bandwidth product, which is given by $kT^2 = BT$. If this time-bandwidth product is higher than 4, it is possible to assume that the first null on the time delay axis, from the AF, it is given by $1/B$ [13]. To understand the advantages of the usage of these pulse compression techniques, lets analyse range resolution: if we want an unmodulated pulse to achieve a range resolution equal to the one achieved when using a LFM pulse with a certain bandwidth B, that unmodulated pulse must have a pulse width equal to $1/B$ of the LFM pulse width. This would require an unmodulated pulse with a short pulse width, what would obviously imply a much larger bandwidth and a lower radiated power, resulting on a lower SNR.

However, this improvement on the range resolution brings out a handicap, related to the delay-doppler coupling. For small Doppler shifts v, the delay location

of the peak response is displaced from true delay τ_{shift}, given by

$$\tau_{shift} = \frac{v}{k} \ , \tag{2.3}$$

occurrence that can be verified by the oblique ridge on the LFM three-dimensional AF (Figure 2.11). The physical explanation for this phenomenon, considering that the signal modulation starts from a lower frequency to a higher frequency (k > 0), is that for targets with positive doppler, the distance seems to be less than its true distance. It is also important to refer that this misconception is acceptable for most applications.

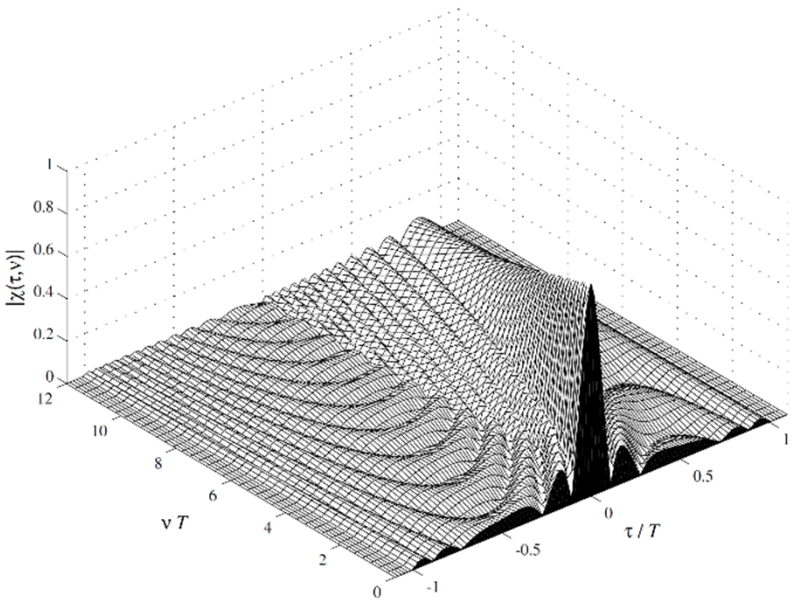

FIGURE 2.11: Partial AF of LFM pulse (BT = 10).
Source: obtained from [13]

Coherent Train of Identical Unmodulated Pulses

In addition to these two types of signals, that similarly centralize the AF volume near the origin, we will analyse the coherent train of identical unmodulated pulses. This technique will spread the AF volume away from the origin, nevertheless having the main narrow peak at the origin, respecting obviously the AF properties. This particular technique uses similar unmodulated pulses during the pulse train, but that cannot always be the case, as some other techniques can be added in order to achieve other type of advantages.

The complex envelope of a train with M similar unmodulated pulses, transmitted with a certain Pulse Repetition Interval (PRI), can be characterized by

$$u_M(t) = \frac{1}{\sqrt{M}} \sum_{m=1}^{M} u_1 \left[t - (m-1)PRI \right] \ . \tag{2.4}$$

The unmodulated nature of each pulse can be obtained by

$$u_1(t) = \frac{1}{\sqrt{T}} rect\left(\frac{t}{T}\right) \ . \tag{2.5}$$

On top of that, the AF of a coherent pulse train (Figure 2.12) is often named a bed of nails [13], which refer to the number of lobes that occur at PRI intervals in delay and at $\frac{1}{PRI} = PRF$ in Doppler. The zero-Doppler cuts can be clearly seen along the triangles formed on the AF, which have a base dimension of 2T and a lobe amplitude sequentially lower. This reduction of amplitude can be simply explained by the fact that for a train of M pulses, around the delay $\tau = 0$, each one of the M received pulses overlap the M reference pulses; for the delay $\tau = PRI$, only M-1 pulses will overlap each other, which will obviously result on a lower amplitude, and so on. The correlation between similar pulses justifies the shape of the peaks being close to a triangle.

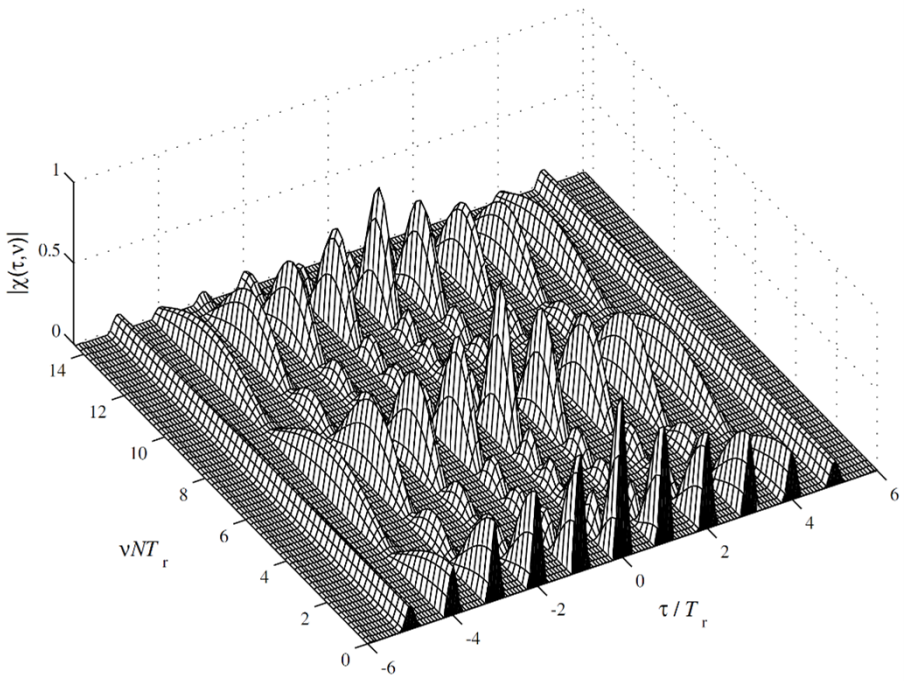

FIGURE 2.12: Partial AF of a coherent train of M = 6 pulses.
Source: obtained from [13]

On the other hand, in figure 2.13 it is possible to see the zero-delay cut of a single pulse, represented by the dashed line, and the zero-delay cut of a train of similar pulses, all coherently processed, represented by the solid line. This representation shows the improvement that is possible to make in Doppler resolution as the Doppler nulls are now located at $\frac{1}{M \cdot PRI}$

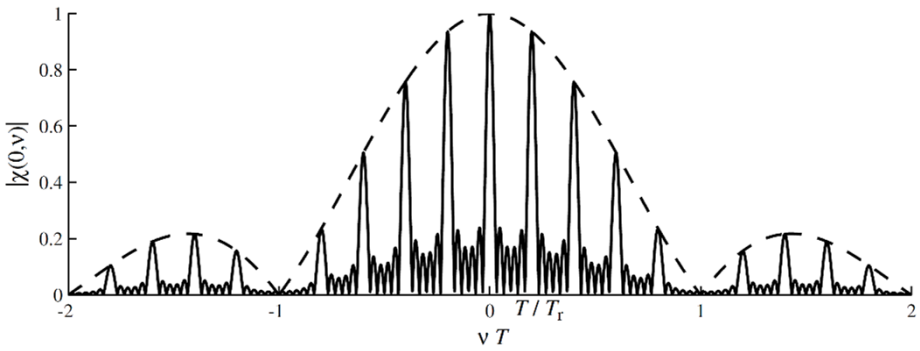

FIGURE 2.13: Zero-delay cut of the AF of a coherent train of M = 6 pulses.
Source: obtained from [13]

In brief, it was possible to verify that this technique allows the delay and Doppler control on an independent way, which was not possible in single pulse techniques. The delay resolution is only dependent of the pulse duration T, while the Doppler resolution is affected by the total signal length $M \cdot PRI$.

Coherent Train of Identical LFM Pulses

With this two pulse compression techniques well understood, it will be interesting to analyse a pulse compression technique that is the conciliation of both, a coherent train of identical LFM pulses. With this solution it is possible to achieve acceptable doppler and range resolutions. The complex envelope of a train with M similar pulses can be characterized by

$$u(t) = \frac{1}{\sqrt{M}} \sum_{m=1}^{M} u_m \left[t - (m-1)PRI \right] \ . \tag{2.6}$$

The LFM nature of each pulse can be obtained by

$$u_1(t) = \frac{1}{\sqrt{T}} rect\left(\frac{t}{T}\right) exp(j\pi k t^2), \quad where \quad k = \pm\frac{B}{T} \ . \tag{2.7}$$

In figure 2.14 it is possible to visualize the signal in its time domain. In this case, all pulses have the same initial phase, but this is not an imperative condition for coherence, which can be preserved as long as the receiver knows each one of the pulses initial phase. For reference, it is also important to mention that for pulse durations $T < \frac{PRI}{2}$, the additional phase element will only influence the AF on its recurrent lobes, specifically for $|\tau \pm m \cdot PRI| \leq T$, which can lead towards the investigation of different solutions by only alternate the initial phase of the pulses, despite that only apply a variation on the recurrent lobes.

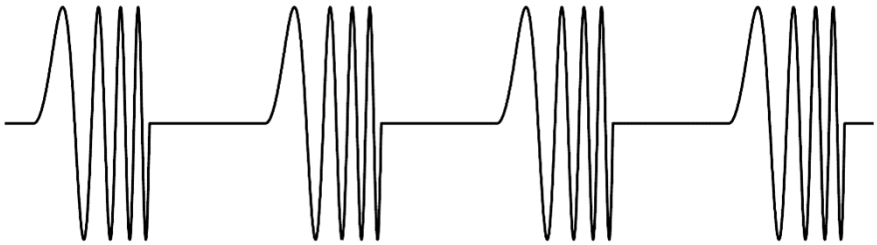

FIGURE 2.14: Coherent train of identical LFM pulses.
Source: obtained from [13]

Figure 2.15 represents the AF of a coherent train with 8 identical LFM pulses, with a Pulse Repetition Frequency (PRF) of 1.25Hz, a duty cycle of 1/9 (=11.(1)%) and a time-bandwidth product of each pulse equal to 20. The first Doppler null is located at $\frac{1}{Tc} = \frac{1}{8 \cdot PRI}$, where T_c is the coherent processing time. As it is already known from the coherent train of identical unmodulated pulses, the lobes in doppler occur in steps defined by the PRF, which also occurs here. Other fact to consider is that the recurrent doppler peaks have a minimal decrease in amplitude and are slightly delayed when compared to the main lobe.

Phase-Coding Pulses

Other important pulse compression technique is based on phase coding. A phase coded pulse is a pulse of duration T, divided into M bits of the same duration t_b ($t_b = T/M$), which are thereupon coded with a different phase value. The complex envelope of a phase coded pulse can be characterized by

$$u(t) = \frac{1}{\sqrt{T}} \sum_{m=1}^{M} u_m rect\left[\frac{t-(m-1)t_b}{t_b}\right] , \tag{2.8}$$

where $u_m = exp(j\phi_m)$ and all M phases $[\phi_1, \phi_2, ..., \phi_M]$ is the phase code associated with $u(t)$.

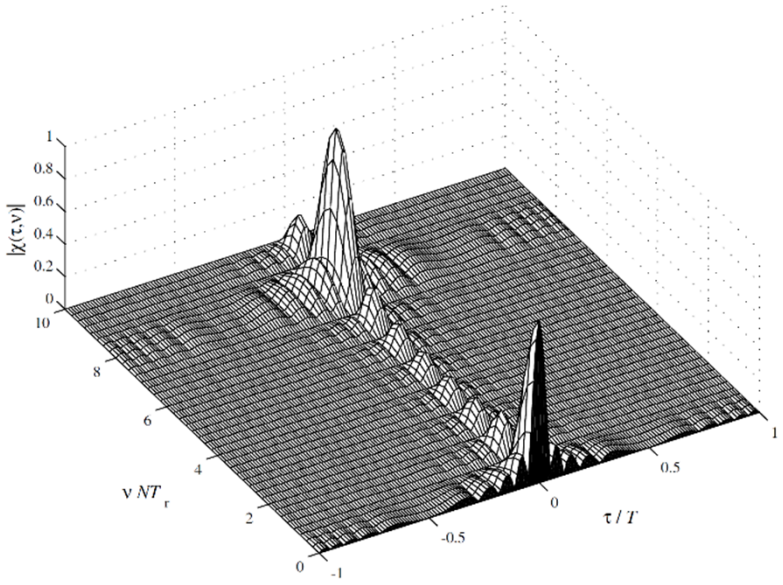

FIGURE 2.15: Partial AF of a coherent train of 8 LFM pulses (BT = 20).
Source: obtained from [13]

Code Length	**Code**
2	11 or 10
3	110
4	1110 or 1101
5	11101
7	1110010
11	11100010010
13	1111100110101

TABLE 2.2: All known binary Barker codes.
[13]

For this specific type of pulse compression technique, we will focus our attention at one of the most popular, the Barker codes (table 2.2). They were developed by Ronald Hugh Barker in 1953 and are a combination of M binary phases that produce a Peak-to-peak SideLobe Ratio (PSLR) of M. This PSLR, for a Barker code of 13 elements, can be clearly seen by its autocorrelation (figure 2.16).

Another relevant aspect in phase-coded signal is that this sudden phase switching generates extended spectral sidelobes, perfectly perceptible in figure 2.16. For a Barker 13 signal, it is expected to have a sidelobe amplitude of $20\log(1/13) = -22.3$dB.

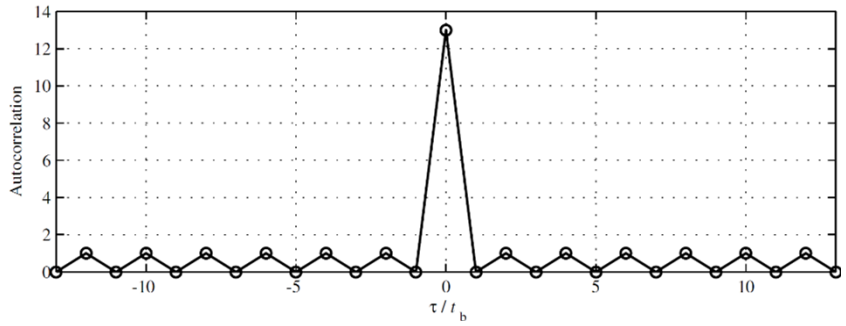

FIGURE 2.16: Autocorrelation function of phase-coded pulse using a 13-element Barker code.
Source: obtained from [13]

The major handicap of phase-coded signals is related to their response towards Doppler shift. When a target induces a Doppler shift, the interference level and expected sidelobes arise to much higher amplitudes than for the zero-Doppler cut, which can be seen in figure 2.17. In this same figure, there is also represented the 1/13 amplitude level (corresponding to the sidelobes amplitude at the zero-Doppler cut) with a solid contour line, making possible the visualization of this aforementioned fact.

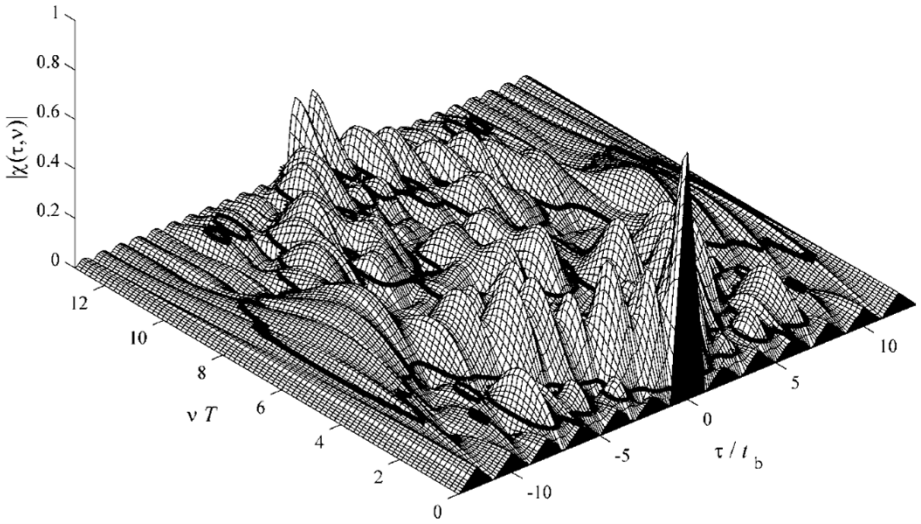

FIGURE 2.17: Partial AF of the 13-element Barker code.
Source: obtained from [13]

Continuos-wave signals

After all, we will describe CW signals, which are also vastly used in radar systems, offering helpful target velocity measurements. Compared with pulsed signals, there is a substantial barrier to intercept the CW signal if the receiver does

not have a matched filter to the expected signal, making the CW waveforms to be mentioned as Low Probability of Intercept (LPI) waveforms.

This continuous transmission of the signal has obviously an implicit issue attached to it, the separation and discrimination of the transmitted and received signal. The most frequently used solution is to have bistatic configuration, i.e. having two isolated antennas, one that works as the transmitter and the other one as the receiver; most of the times, it is also used pulse modulation to guarantee this separation.

On a CW signal, the Doppler resolution is associated with the signal duration that is coherently processed by the receiver. Considering that the receiver can be always receiving the signal, it is valid to affirm that it could remain doing the processing infinitely, but to simplify our analysis, we will assume that the receiver is matched to a signal of duration of $M \cdot PRI$, as if the transmitter radiates M consecutive pulses, with a determined PRI, without any space or time between them. This processing has a response that can be analysed making use of a Periodic Ambiguity Function (PAF), which has a similar role that regular AF has with finite energy signals.

The biggest benefit in using a CW signal is the fact of having a theoretical perfect Periodic AutoCorrelation Function (PACF), with zero sidelobes. The best option is to explore this feature and then combine it with other type of pulse modulation to achieve the best solution.

Chapter 3

Development of the Earth-Space Propagation Simulator

Incorporated on an endeavour to improve the EUSST sensor network capability, Instituto de Telecomunicações (IT) has started the development of its own radar for space debris tracking in LEO named rAdio TeLescope pAmpilhosa Serra (ATLAS) [15]. This system operates on a monostatic configuration, using a cassegrain antenna with 9 meters of diameter, located in Pampilhosa da Serra. It transmits pulses on C-band, more precisely at 5.56 GHz with a bandwidth of 80 MHz, and use a solid state power amplifier that provides the system with a peak transmission power of 5kW, producing consequently an antenna gain of 46 dBi. It is entirely coherent with detection and processing thoroughly in the digital domain with a bandwidth of 50 MHz and have the capability to detect Doppler velocities till 10.79 km/s.

To precisely determine the system capabilities and consequent performance, it is extremely helpful to create an earth-space propagation model, which would give us all the information needed such as ionospheric phenomenons caused by the electron density over the atmosphere, atmospheric attenuation due to oxygen and water vapour, excess path length due to refractive index alteration, among others.

To develop this earth-space propagation simulator, it was considered that all system's features are categorized as being a Linear Time Invariant (LTI) system, producing an output $y(t)$ from any arbitrary input $x(t)$ that can be directly calculated using convolution: $y(t) = x(t) * h(t)$, where $h(t)$ is the system's transfer function and $*$ represents the convolution. This technique is illustrated in figure 3.1, making us establish as our main task the determination of all propagation feature's frequency response (transfer function).

FIGURE 3.1: Simulator mechanism illustrated.

3.1 Atmospheric Propagation Phenomena

The performance of a radar system does not only depend on the hardware and transmitting/receiving sites and structures, but also on a variety of phenomena that affect the electromagnetic waves propagation [16] [17]. It is important to be aware that all these phenomena foisted by the natural environment are highly dependent on the electromagnetic wave frequency, on the directivity and consequential gain of the transmitting and receiving antennas, as on the distance between each other and the target. For this simulator, only the constant phenomena were considered, i.e. phenomena like ionospheric scintillation created by inhomogeneities in the medium, rain, snow, clouds or fog attenuation, auroral absorption, polar cap absorption, signal enhancement or multipath fading caused by surface and elevated ducts, among others, were not take into consideration. These considered phenomenons are divided by its origin, as illustrated in figure 3.2.

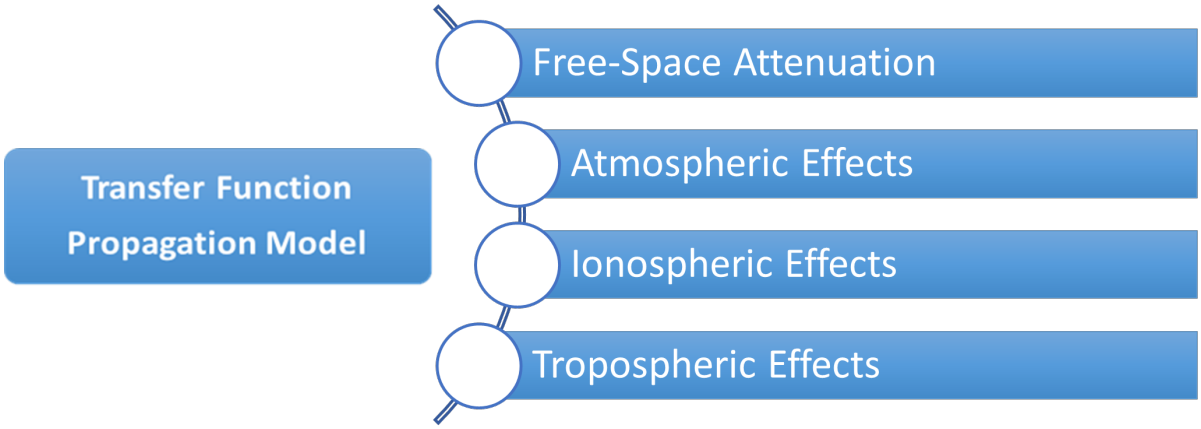

FIGURE 3.2: Atmospheric propagation phenomena.

3.1.1 Free-Space Attenuation

Free-space is a medium with perfect vacuum by definition [18], which for radiocommunication purposes is considered as being infinite in all directions, being

the free-space attenuation established as the loss of power of the electromagnetic wave foisted by its omnidirectional propagation through this free-space.

3.1.2 Atmospheric Effects

The electromagnetic signal it is affected by atmospheric effects during its propagation, whose effects rely on the presence of oxygen and water vapour on the atmosphere [19]. Water vapour is one of the most influent gases when talking about attenuation and dispersion on electromagnetic waves, due to molecular absorption in many frequencies [20] [21], which correspond to the number of water vapour molecule frequencies of resonance, known as water vapor spectral lines, being obviously important to consider the high geographical, seasonal and daily variability it has. On the other hand, oxygen also has a big influence in this attenuation and dispersion process due to its molecule ressonant complex (spectral lines) in many frequencies as well [20].

All these spectral lines can be seen in figure 3.3, where the blue line represents the dry atmosphere with absence of water vapor, being possible to verify the oxygen spectral lines. On the other hand, the standard atmosphere is represented by the red line, and because the water vapour attenuation and dispersion contribution is higher than oxygen (for most frequencies), it is possible to see the water vapour spectral lines with a standard atmosphere, nevertheless the presence of oxygen as well.

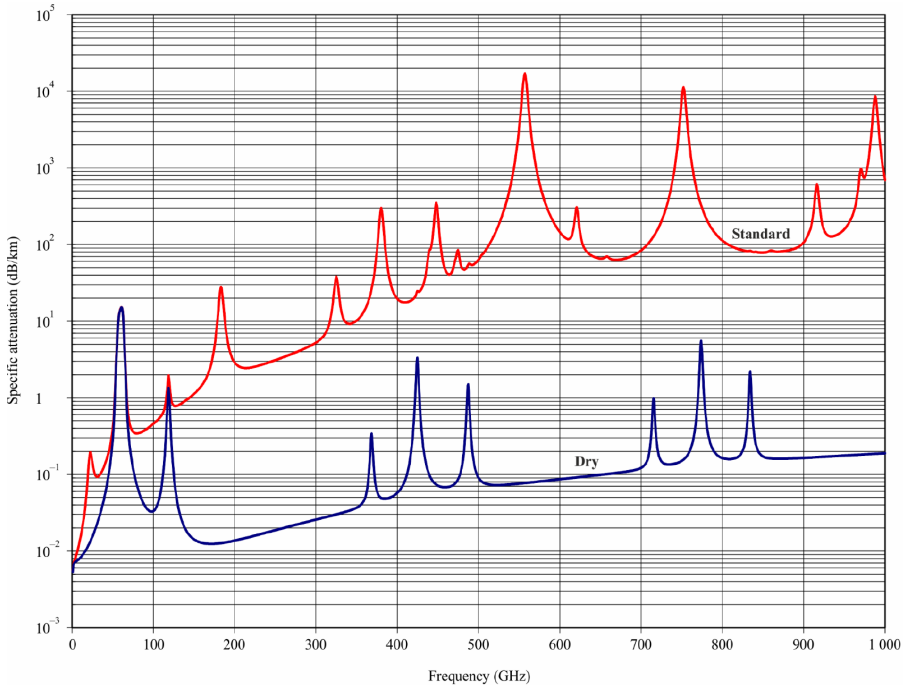

FIGURE 3.3: Specific attenuation due to atmospheric gases.
Source: obtained from [20]

Besides the electromagnetic wave frequency, atmospheric attenuation and dispersion is also dependent of temperature, pressure and water vapour density, establishing a crucial point to consider in order to achieve a meticulous propagation simulator.

3.1.3 Ionospheric Effects

To evaluate the ionospheric propagation effects on a electromagnetic wave, it is important to understand what is in fact the ionosphere [16]. The most important characteristic from this layer is that it is ionized by solar radiation, so dependently on the solar radiation intensity at a certain time of the day, season or even for different sun cycles, its height and electron density may vary. For example, during the day, it is probable that ionosphere lodges between 90km and 1000km above earth's surface, having a electron density between 10^{10} and 10^{12} electrons per cubic meter.

Ionosphere is also divided in three main distinguished layers named D, E and F layers, as illustrated in figure 3.4. This same figure has the daytime and nighttime representation made by two distinctive lines, where it is possible to see that during nighttime, the D layer disappears, and on the daytime, the F layer splits into two layers F1 and F2.

During the propagation through the ionosphere, the electromagnetic wave undergoes through many phenomena as [22]:

- Faraday rotation: defined as the polarization rotation due to interactions with the ionized medium in the Earth's magnetic field.
- Group delay and phase advance: result of the Total Electron Content (TEC) along the path.
- Scintillations: fast variation of the wave amplitude and phase due to irregularities in the ionosphere.
- Doppler effects: result of non-linear polarization rotations and time delays.
- An apparent modification on the arrival angle due to refraction.

For reference, it is known that for electromagnetic waves with frequency above 40 MHz [16], the wave will pass through the ionosphere. For frequencies much higher than that, the ionospheric effects are much less perceptible, but still significantly occur until 12 GHz [22], making important to consider all these phenomena during the development of the propagation simulator.

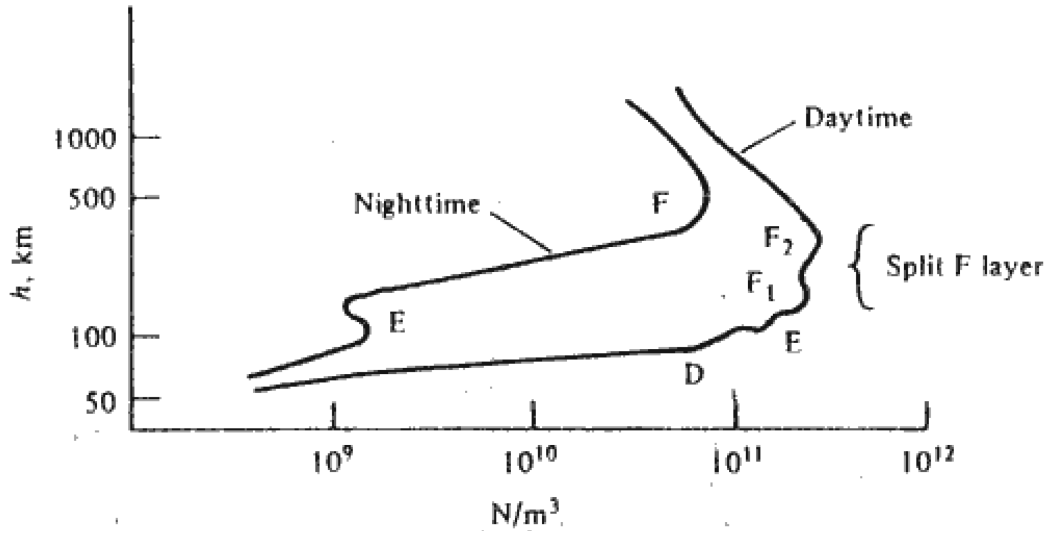

FIGURE 3.4: Typical variation of electron density in function of height.
Source: obtained from [16]

3.1.4 Tropospheric Effects

Lastly, troposphere is a Earth's atmosphere layer that exhibits a high complex time-space dependence [23], making temperature, water vapour density and

pressure very important values in order to evaluate the effects produced by the changes on the refractive index during the propagation, which can be ray bending, ducting layers, excess path length, among others.

As an example, in figure 3.5 it is possible to see the average excess path length for January (at the top) and July (at the bottom) along the globe, which demonstrates the time-space dependence that tropospheric effects have in propagation.

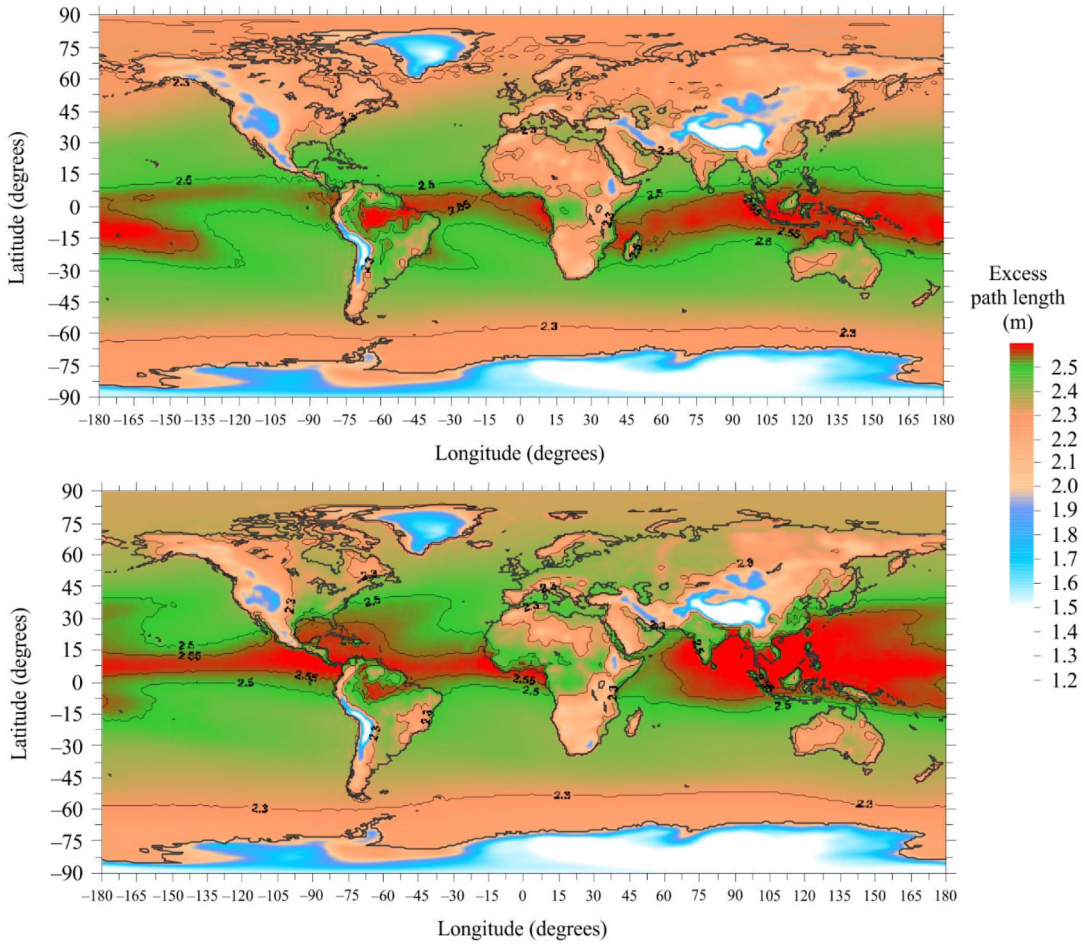

FIGURE 3.5: Average excess path length along the globe for January and July.
Source: obtained from [24]

3.2 International Telecommunication Union Recommendations

With the goal of developing the Earth-space propagation simulator, some recommendations from the International Telecommunication Union Radiocommunication Sector (ITU-R) were considered.

The International Telecommunication Union (ITU) is the UN specialized agency for Information and Communication Technologies (ICT), it was founded in 1865 to ease international connectivity in communications networks, establishing the technical standards that guarantee that all technologies and networks interconnects perfectly, determining the use of global radio spectrum and satellite orbits, and also working on the access improvement to all ICTs by the underserved communities worldwide.

On a world highly-dependent on telecommunication systems, where it is possible to manage almost every business through the internet, learn about a culture from the other side of the world, that have all kind of entertainment content or simply check the weather forecast, ITU played a crucial role in connecting the world.

Looking in specific now for the ITU-R, its mission goes through the management of the radio-frequency spectrum, establishing the equitable, reasonable, efficient and economical use of it by all kind of radiocommunication services. This effort is crucial considering that this spectrum is a natural resource, which is limited and with an increasingly demand for it, which is justified by the growing number of features such as mobile phones, broadcasting, emergency telecommunications, space research, global positioning systems, meteorology, environmental monitoring and many others.

In order to guarantee radiocommunications systems free of interferences, it was been implemented the Radio Regulations and Regional Agreements, which are constantly updated due processes of the World and Regional Radiocommunication Conferences, which are also responsible for all the regulatory and policy functions. For assuring the necessary quality and performance through all radiocommunication systems, there was established “Recommendations” for standardization, which will be used on this simulator.

It is also important to refer that ITU-R Recommendations are approved by ITU Member States. Their contemplation and consequent implementation is not imperative, nevertheless they are developed by experts from the industry, operators,

administrations and other organizations that deal with all kind of radiocommunication matters, making them a resource with high reputation.

3.3 Analytical Formulation

In order to develop the earth-space propagation simulator, we started by looking at recommendation ITU-R P.619-4 [25], which gives all the information needed in order to evaluate the propagation losses and interferences between earth and space stations. This recommendation is valid for a frequency range between 100 MHz and 100 GHz, except for a negligible amount of lower frequencies. Additionally, it is also referred which ITU-R recommendations should be used for each type of propagation phenomena.

3.3.1 Free-Space Attenuation

To calculate how the radar signal will be affected by free-space during its propagation, we followed ITU-R P.525-4 - "Calculation of free-space attenuation" [18]. In this recommendation, expression 3.1 is used to calculate the free-space basic transmission loss for a radar system, which takes into consideration the propagation of the signal on the way to the target and back, and also that the antenna used is a common one (not a phased-array antenna, for example).

$$L_{br} = 103.4 + 20 \log f + 40 \log d - 10 \log \sigma \qquad \text{dB} , \tag{3.1}$$

where:

- σ: RCS from the target (m^2).
- d: distance between the radar and the target (km).
- f: signal frequency (MHz).

3.3.2 Atmospheric Effects

With the purpose of calculating the effects that will affect a radar signal during its propagation through the atmosphere, recommendation ITU-R P.676-12 [20] was used.

Atmospheric Attenuation

This recommendation gives two methods to determine the atmospheric attenuation, both available to use on earth-space paths, but because one is given as being more accurate, we choose that one, that determines the specific gaseous attenuation relying on the summation of individual absorption spectral lines, valid for frequencies up to 1000 GHz. To accurately apply this method, it is important to know the temperature, water vapour density and pressure, as a function of height, along the path.

The specific gaseous attenuation γ is given by

$$\gamma = \gamma_o + \gamma_w = 0.1820 f \left(N''_{Oxygen}(f) + N''_{WaterVapour}(f) \right) \qquad \text{(dB/km)} \ , \tag{3.2}$$

where γ_o and γ_w are the oxygen and water vapour specific attenuation, determined for a f frequency (GHz), being the $N''_{Oxygen}(f)$ and $N''_{WaterVapour}(f)$ the imaginary parts of the frequency-dependent complex refractivities given by

$$N''_{Oxygen}(f) = \sum {}_{i(Oxygen)} S_i F_i + N''_D(f) \ , \tag{3.3}$$

$$N''_{WaterVapour}(f) = \sum {}_{i(WaterVapour)} S_i F_i \ . \tag{3.4}$$

These two frequency-dependent complex refractivities are the product of the affiliation between the strength of the i^{th} oxygen spectral line S_i given by

$$S_i = a_1 \times 10^{-7} p \cdot \theta^3 exp\left[a_2(1-\theta)\right] \ , \tag{3.5}$$

and water vapour spectral line S_i given by

$$S_i = b_1 \times 10^{-1} e \cdot \theta^{3.5} exp\left[b_2(1-\theta)\right] \ , \tag{3.6}$$

where:

- p: dry air pressure (hPa).
- e: water vapour partial pressure (hPa), given by

$$e = \frac{\rho T}{216.7} \ . \tag{3.7}$$

- Total barometric pressure $= p + e$.
- $\theta = 300/T$.
- T: temperature (K).

On the other hand, the oxygen and water vapour spectral line shape imaginary factor F_i is given by

$$F_i = \frac{f}{f_i}\left[\frac{\Delta f - \delta(f_i - f)}{(f_i - f)^2 + \Delta f^2} + \frac{\Delta f - \delta(f_i + f)}{(f_i + f)^2 + \Delta f^2}\right] , \tag{3.8}$$

where f_i is the spectral line frequency and Δf the width of the oxygen spectral line given by

$$\Delta f = a_3 \times 10^{-4}\left(p \cdot \theta^{(0.8-a_4)} + 1.1e \cdot \theta\right) , \tag{3.9}$$

and the width of the water vapour spectral line given by

$$\Delta f = b_3 \times 10^{-4}\left(p \cdot \theta^{b_4} + b_5 \cdot e \cdot \theta^{b_6}\right) . \tag{3.10}$$

However, oxygen spectral line width is readjusted thanks to Zeeman splitting, whose readjustment leads to a complementary expression of Δf given by

$$\Delta f = \sqrt{\Delta f^2 + 2.25 \times 10^{-6}} . \tag{3.11}$$

On the other hand, water vapour spectral line width is also readjusted thanks to Doppler broadening of water vapour spectral lines, whose readjustment also leads to a complementary expression of Δf given by

$$\Delta f = 0.535\Delta f + \sqrt{0.217\Delta f^2 + \frac{2.1316 \times 10^{-12} f_i^2}{\theta}} . \tag{3.12}$$

The oxygen complex refractivity is also influenced by the dry continuum due to pressure-induced nitrogen absorption and the Debye spectrum $N''_D(f)$, given by

$$\delta = (a_5 + a_6\theta) \times 10^{-4}(p + e)\theta^{0.8} . \tag{3.13}$$

This δ factor is equal to zero for water vapour spectral lines.

As referred earlier in subsection 3.1.2, for frequencies starting from 100GHz,

the oxygen's complex refractivity is affected by the pressure-induced nitrogen attenuation and also, for frequencies up to 10GHz, by the dry air continuum originated by the oxygen non-resonant Debye spectrum N''_D, given by

$$N''_D(f) = fp\theta^2 \left[\frac{6.14 \times 10^{-5}}{d_s \left[1 + (\frac{f}{d_s})^2\right]} + \frac{1.4 \times 10^{-12} p \cdot \theta^{1.5}}{1 + 1.9 \times 10^{-5} f^{1.5}} \right] , \tag{3.14}$$

where d_s is the Debye spectrum's width parameter, given by

$$d_s = 5.6 \times 10^{-4}(p + e)\theta^{0.8} . \tag{3.15}$$

Note that all a_n and b_n are predefined values related to the spectroscopic data of oxygen and water vapour respectively, which can be found in annex I and also on ITU-R P.676-12 [20].

Atmospheric Dispersion

On the other hand, recommendation ITU-R P.676-12 [20] also discloses the dispersive effects that occur during the propagation of an electromagnetic wave through the atmosphere, which are associated to the real part of the frequency-dependent complex refractivity and represented by the specific gaseous phase dispersion φ given by

$$\varphi = \varphi_o + \varphi_w = -1.2008 f \left(N'_{Oxygen}(f) + N'_{WaterVapour}(f) \right) \qquad (deg/\text{km}) , \tag{3.16}$$

where φ_o and φ_w are the oxygen and water vapour specific phase dispersion, given by determined for a f frequency (GHz), being the $N'_{Oxygen}(f)$ and $N'_{WaterVapour}(f)$ the real parts of the frequency-dependent complex refractivities given by

$$N'_{Oxygen}(f) = \sum {}_{i(Oxygen)} S_i F'_i + N'_D(f) , \tag{3.17}$$

$$N'_{WaterVapour}(f) = \sum {}_{i(WaterVapour)} S_i F'_i . \tag{3.18}$$

Similarly to the atmospheric attenuation, S_i is also the strength of the i^{th} oxygen and water vapour spectral lines respectively, as described in equation 3.5 and equation 3.6. On the other hand, F'_i is the real part of the oxygen and water

vapour spectral line shape factor, given by

$$F_i' = \frac{f}{f_i}\left[\frac{(f_i - f) + \delta\Delta f}{(f_i - f)^2 + \Delta f^2} + \frac{(f_i + f) + \delta\Delta f}{(f_i + f)^2 + \Delta f^2}\right] , \tag{3.19}$$

where Δf is defined in equation 3.12 and equation 3.11 and δ is defined in equation 3.13.

Lastly, as it is already known, the dry air continuum also affects the oxygen's complex refractivity due to pressure-induced nitrogen absorption, being represented by its real part $N_D'(f)$, given by

$$N_D'(f) = \frac{-6.14 \times 10^{-5} p \cdot \theta^2 f^2}{f^2 + d_s^2} , \tag{3.20}$$

where d_s is defined in equation 3.15.

3.3.3 Ionospheric Effects

As referred earlier, the Earth's ionosphere appears from influence of solar radiation, creating many ionization regions that consequently will be the source of many ionospheric effects during the propagation of electromagnetic waves, described in recommendation ITU-R P.531-14 [22]. These effects are directly associated to the TEC, represented as N_T, which can be determinated by

$$N_T = \int_s n_e(s) ds , \tag{3.21}$$

where:

- s: propagation path (m).
- n_e: electron concentration (el/m^3).

During the propagation of a linearly polarized electromagnetic wave through the ionosphere, as a consequence of the TEC presence, geomagnetic field and all the inhomogeneities of the medium, a gradual rotation of the polarization plane occurs, known as Faraday rotation θ, which is given by

$$\theta = 2.36 \times 10^{-14} \frac{B_{av} N_T}{f^2} \qquad \text{(rad)} , \tag{3.22}$$

where:

- θ: Faraday angle of rotation (rad).

- B_{av}: Earth magnetic field ($\mathrm{Wb} \cdot \mathrm{m}^2$ or T).
- f: frequency (GHz).
- N_T: TEC ($el \cdot \mathrm{m}^{-2}$).

In addition, the presence of electrons in the ionosphere also slows down the propagation velocity of electromagnetic waves, which obviously induce a time delay when comparing the real propagation path with a propagation path on full vacuum, which will interfere with the signal phase. This excess time delay, mentioned as group delay t, is determinated by

$$t = 1.345 \cdot N_T / f^2 \times 10^{-7} \ , \tag{3.23}$$

where:

- t: group delay (s).
- f: frequency (Hz).
- N_T: TEC ($el \cdot \mathrm{m}^{-2}$).

3.3.4 Tropospheric Effects

As mentioned before, when analysing the influence of troposphere in the propagation of electromagnetic waves, the main phenomenon to consider is the excess radio path length ΔL, when comparing to the geometrical path length, as an outcome of the variation of the refractive index along the path, as described in recommendation ITU-R P.834-9 [24]. The exceeding radio path length is given by

$$\Delta L = \int_A^B (n-1) ds \ , \tag{3.24}$$

where

- s: length of propagation path.
- n: refractive index.
- A and B: path extremities.

To accurately determine the refractive index value, recommendation ITU-R P.453-14 [26] was used, where it was possible to perceive that the refractive index is given by

$$n = 1 + N \times 10^{-6} \ . \tag{3.25}$$

Equally, N is the radio refractivity given by:

$$N = 77.6\frac{P_d}{T} + 72\frac{e}{T} + 3.75 \times 10^5 \frac{e}{T^2} \ , \tag{3.26}$$

where:

- P_d: dry atmospheric pressure (hPa).
- $P = P_d + e$: total atmospheric pressure (hPa).
- e: water vapour pressure (hPa).
- T: absolute temperature (K).

3.4 Simulator

This section describes the simulator's functions and respective interdependences. In figure 3.6 is represented the block diagram of the simulator, being all source code accessible on the simulator GitHub link [27].

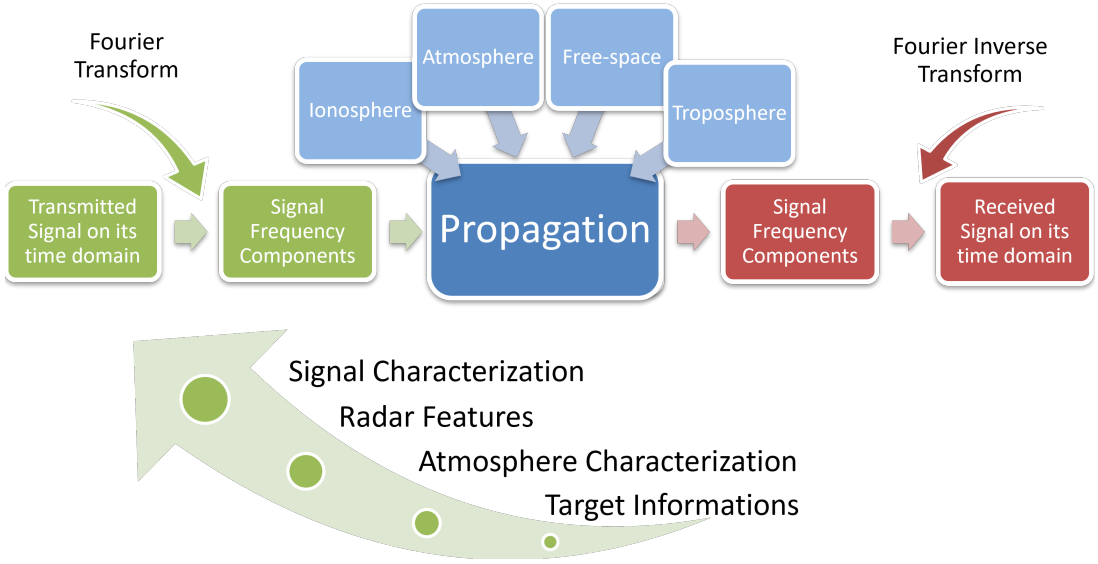

FIGURE 3.6: Simulator block diagram.

3.4.1 Main Script

The simulator's operation is managed by a main script, which can do the interface with the user using the compiler's console or using a Graphical User Interface (GUI), notwithstanding both do the exact same thing.

Compiler's Console

When using the compiler console, the user will have to introduce some inputs related to the pulse to be transmitted, as well as related to the transmission conditions, which will be requested sequentially. It is important to mention that for each of the inputs, there will be a verification so that incompatible data with the simulator would not be allowed; if an incompatible input is given, the simulator will ask for a new one.

Depending on which pulse the user wants to transmit, distinct inputs will be requested, including: number of pulses to be transmitted, carrier frequency, signal bandwidth, PRF and duty cycle.

In terms of transmission conditions, it will be requested the azimuth and elevation to which the radar points, the shape and dimensions of the target in order to calculate its RCS, its expected height, as well as the season of the year and time of day for which the user wants to run the simulation.

After having all the simulation features established, the script will run all other functions sequentially and thus simulate the atmospheric propagation for that specific radar pulse.

GUI

On the other hand, a GUI was developed in order to offer the user a more attractive way of interacting with the simulator, allowing the user to choose some of the main features of the radar, like its peak power, system losses and noise factor (that are predefined for the ATLAS case), nevertheless the functionalities are exactly the same. The layout is shown in figure 3.7.

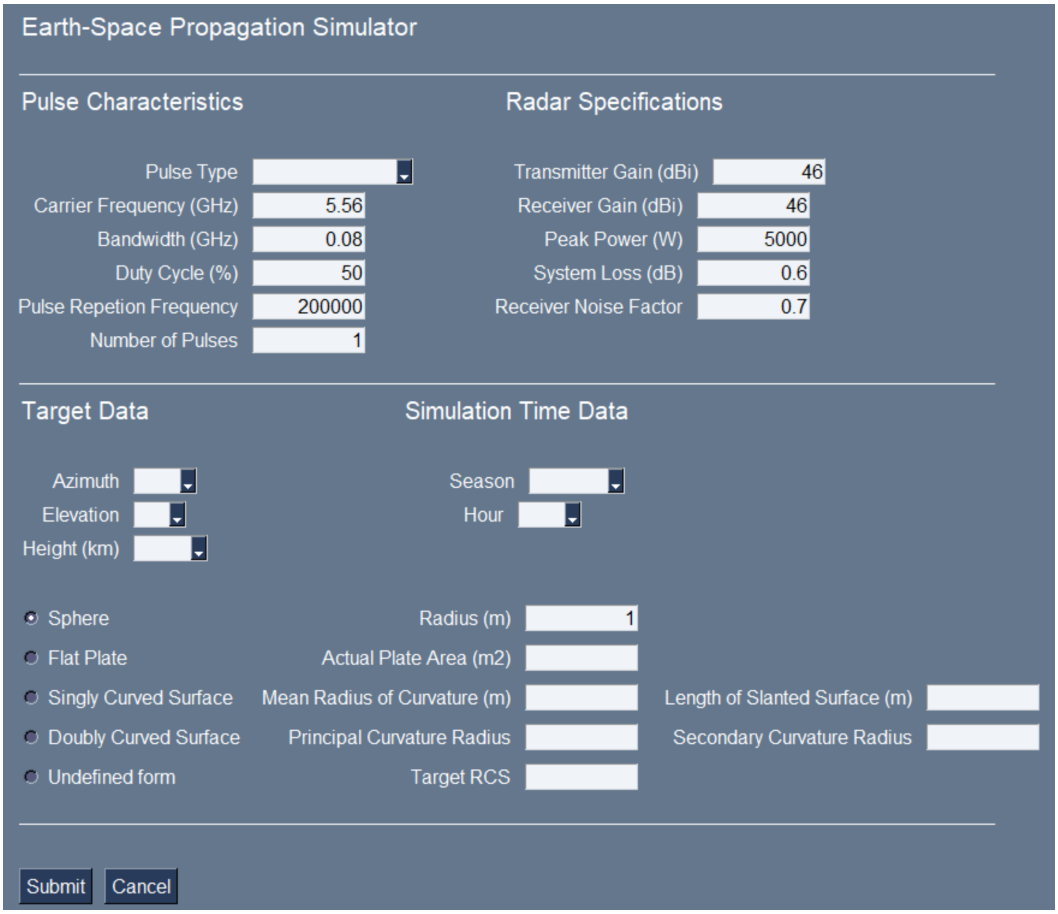

FIGURE 3.7: GUI layout.

The only disadvantage it offers is the fact that there are unnecessary parameters for some radar pulses, which are not updated during the inputs acquirement, there are simply parameters that, even when filled in, will not be considered if the chosen radar pulse does not require them.

3.4.2 Waveform Characterization

The conceptualization of the waveform that will caracterize the radar signal is the main responsible for the radar detection and tracking capabilities, influencing its accuracy, resolution and ambiguity [13]. It is obviously a challenging task, as most times it is majority relied on the engineer experience, knowledge and ability to manipulate the signal's waveform and its parameters in order to achieve the best features for our specific case. Different signal's waveforms are required for different situations, there is not a perfect scenario or signal for every situation.

To compute some of the most used radar signals, we had access to a GitHub repository [28], where it was possible to a get a script named "ambpy", which would

be used to create the signal on its time domain, as well as creating the zero doppler cut afterwards.

LFM Pulse

To compute a LFM pulse, the user will choose some fundamental features considering the signal to be transmitted, which are: the carrier frequency in GHz, the signal bandwidth in GHz, the PRF and the duty cycle in percentage.

It is important to refer that initially only the modulated signal will be created, not considering the carrier frequency, which frequencies will vary from $-\frac{bandwidth}{2}$ to $\frac{bandwidth}{2}$. Considering the given PRF and duty cycle, the time array in which our modulated signal will be introduced is also calculated.

By using the "chirp" function from the "scipy.signal" library, it is possible to create the real (in blue) and imaginary (in orange) components of the signal as is possible to see in figure 3.8, which will be used to create the array with the complex signal with the help of the "ambpy" script, which returns its amplitude and time arrays, procedure that will be done for all signals.

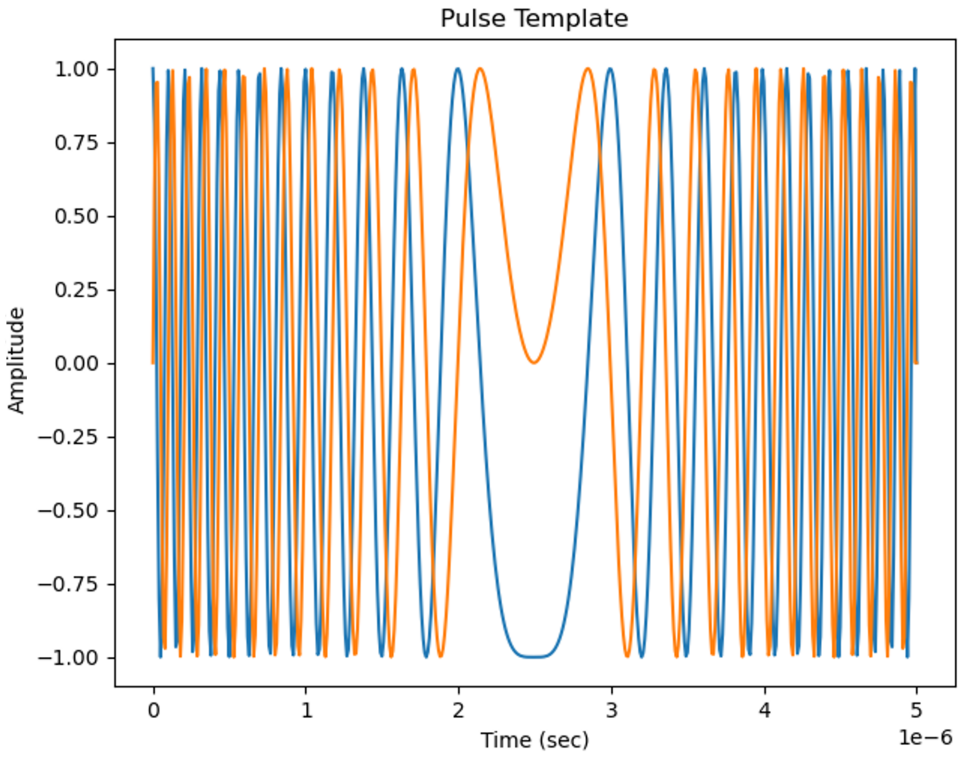

FIGURE 3.8: LFM Pulse.

LFM Train

To compute a LFM train, the inputed data will be practically the same as for a LFM pulse, except for the number of identical pulses that the user wants to transmit, so he has to input the following features: the carrier frequency in GHz, the signal bandwidth in GHz, the PRF, the duty cycle in percentage and the number of pulses.

Analogously to the LFM pulse, initially only the modulated signal will be created, varying from $-\frac{bandwidth}{2}$ to $\frac{bandwidth}{2}$. Relatively to the time array creation, the chosen PRF and duty cycle will correspond to only one pulse, so if the user wants to transmit m pulses, the time array will be determined for a total duration of m/PRF. An example of a transmission using a LFM train modulation can be seen in figure 3.9

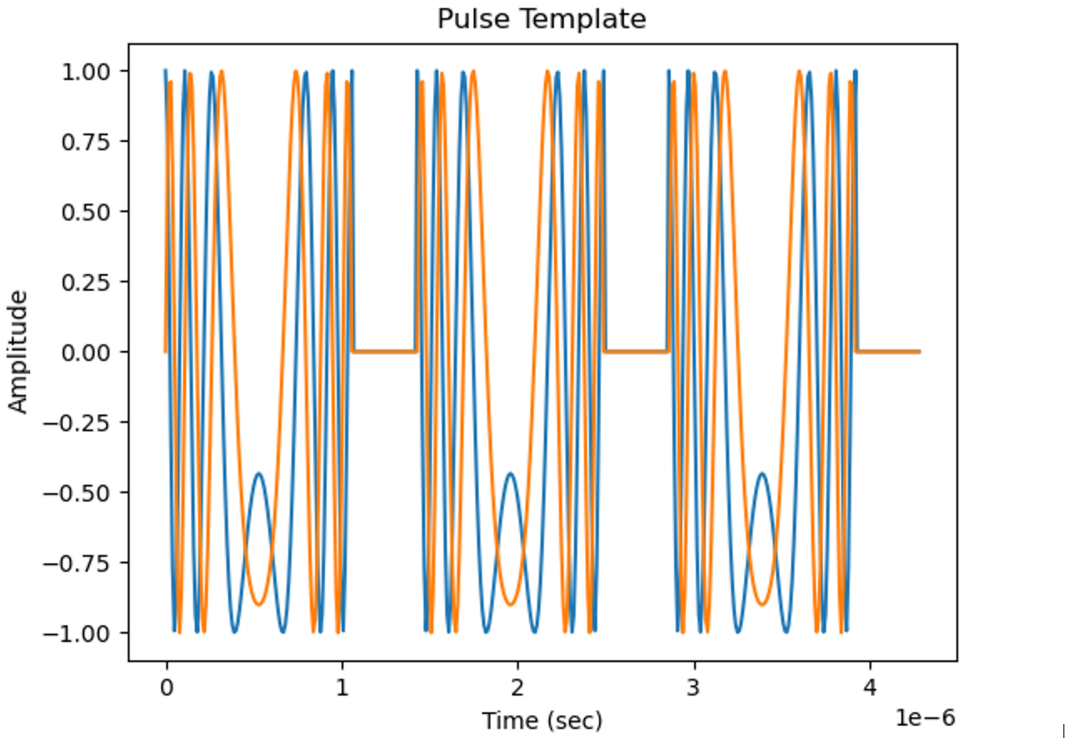

FIGURE 3.9: LFM Train.

Stepped FM

The inputs needed in order to compute a stepped FM signal are exactly the same as for the LFM train, which are: the carrier frequency in GHz, the signal bandwidth in GHz, the PRF, the duty cycle in percentage and the number of pulses.

On the other hand, the modulation of the n pulses to be transmitted is slightly different from the one that is done for a LFM train, as the n pulses will no longer be identical, dividing the bandwidth included between $-\frac{bandwidth}{2}$ to $\frac{bandwidth}{2}$ into n discrete values of frequency and then compute those m pulses with a sinusoidal wave with the respective frequencies, which have their real (in blue) and imaginary (in orange) components computed using a cosine and sine function respectively, as represented in figure 3.10.

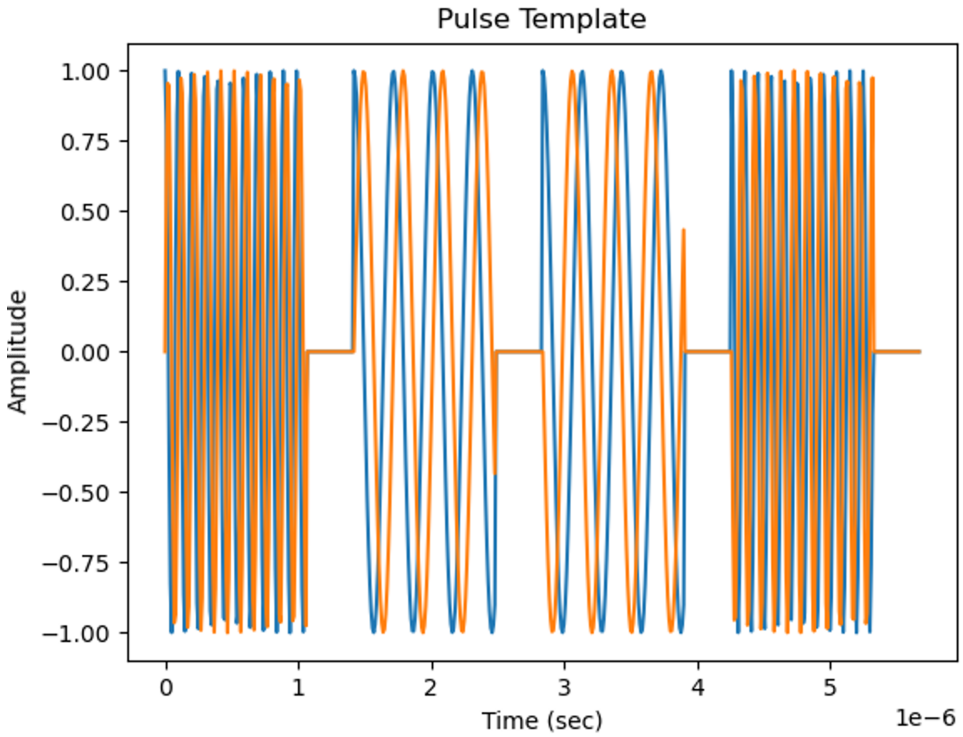

FIGURE 3.10: Stepped FM.

Barker Code

Alternatively to the frequency modulations previously discussed, barker codes are a pulse compression technique that uses phase modulation. There are only seven barker codes defined, which were described previously in table 2.2 at subsection 2.3.3, and it is believed that no more can be discovered. Therefore, in order to compute this signal, the user needs to give these inputs: barker code order, the carrier frequency in GHz, the PRF and the duty cycle in percentage.

To compute the barker code, it is important to determine first the pulse width, given by duty cycle/PRF, so then it is possible to figure out the time that every element of the code will occupy. It is essential to understand that a barker code is a binary code, but the 0's are in reality -1's, in order to maintain the mean

signal power while a phase rotation of π is applied. For example, in figure 3.11 it is shown the barker13 on its baseband, where is possible to see the consecutive binary changes. In addition, in figure 3.12 it is possible to see the result of the addiction of the barker code to its carrier, where we can see the sinusoidal wave divided into 13 equal time intervals, allowing that way a full wave cycle for each code element.

The main concept on barker codes is to create a phase inversion on the computed sinusoidal wave when one element of the code is different form the previous one. The complex signal and its time array will also be calculated using the "ambpy" script, which can be seen in figure 3.12.

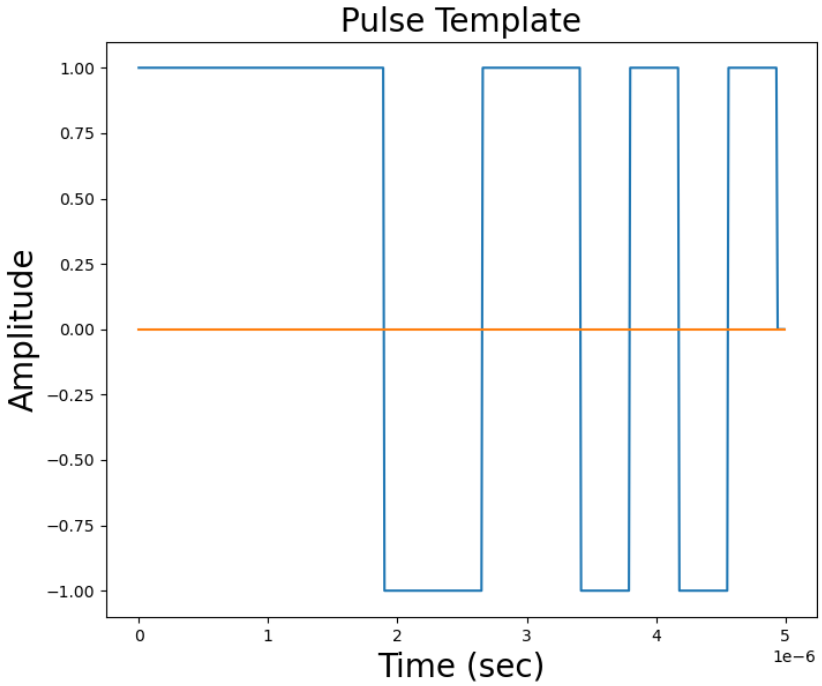

FIGURE 3.11: Barker13 code.

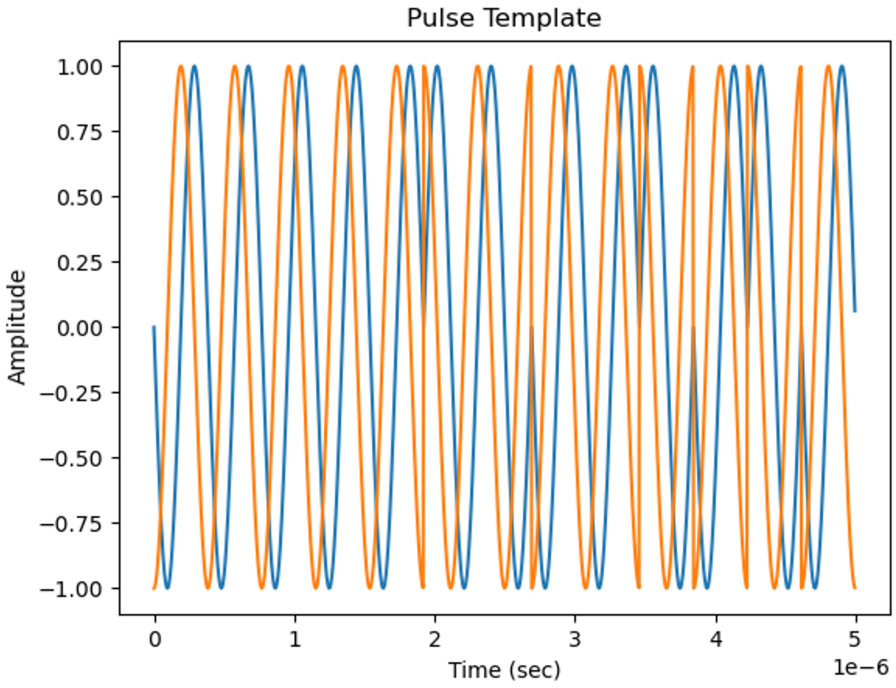

FIGURE 3.12: Barker13 code applied to a carrier.

Signal Fast Fourier Transform

Finally, the Fast Fourier Transform (FFT) of the signal is calculated, producing a complex array with the same dimension as the signal on its time domain, which will be used to determining the amplitude and phase of each of the frequency components of the signal in question (figure 3.13 and later to calculate the impact that atmospheric propagation causes on the signals.

3.4.3 Signal Propagation

The propagation effects that will be induced on the transmitted signal will be introduced on the frequency spectrum, i.e. all propagation effects on the considered frequency range ($f_{carrier} - \frac{bandwidth}{2}$ to $f_{carrier} + \frac{bandwidth}{2}$) will be calculated and then added to the signal frequency spectrum.

Atmospheric Effects

As already described in 3.3.2, in order to accurately determinate the attenuation imposed by atmospheric gases on the transmitted signal, it is imperative to know the atmosphere variables, like its temperature, water vapour density and dry hair pressure, along the path.

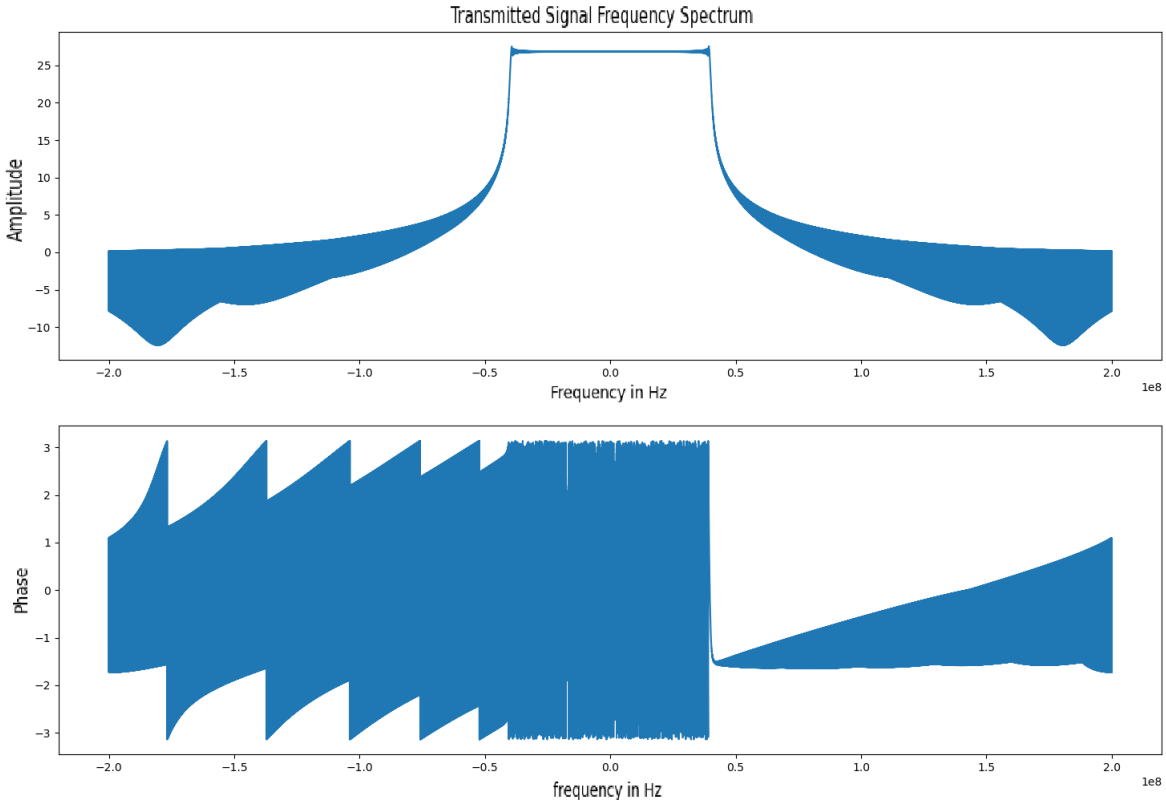

FIGURE 3.13: Signal frequency domain after FFT.

With that objective, ITU-R P.835-6 [29] provides calculation methods for mid-latitudes atmospheres, available in annex II, making that way possible the calculation of the height profiles of those three variables, which can correspond to summer or winter.

Known the vertical profiles of the atmosphere variables, it remains to be known for how many heights it will be necessary to calculate the specific gaseous attenuation and phase dispersion (equation 3.2 and equation 3.16), information that is described in recommendation ITU-R P.676-12 [20], which declares that for slant paths, the layers' thickness must increase exponentially and that for the calculation of the specific gaseous attenuation and phase dispersion, considering that atmosphere has its maximum height at 100km, $i = 922$ layers should be established, whose respective height is given by

$$h_i = 0.0001 \frac{e^{\frac{i-1}{100}} - 1}{e^{\frac{1}{100}} - 1} \ , \tag{3.27}$$

which respective layer thickness is given by

$$h_i = 0.0001 e^{\frac{i-1}{100}} \ . \tag{3.28}$$

At this point, we know exactly at what heights it is necessary to calculate the temperature, dry air pressure and water vapour density, values that will be saved on a three-dimensional array, just like exemplified in figure 3.14. Each column will have a single height associated to it from the 922 needed, which will be constituted by six rows: from the first to the last row, it has the height of the layer, its thickness, temperature, dry air pressure, water vapour density and the frequency that is being considered while determining the specific gaseous attenuation and phase dispersion. This frequency only changes when going trough the third index of the array.

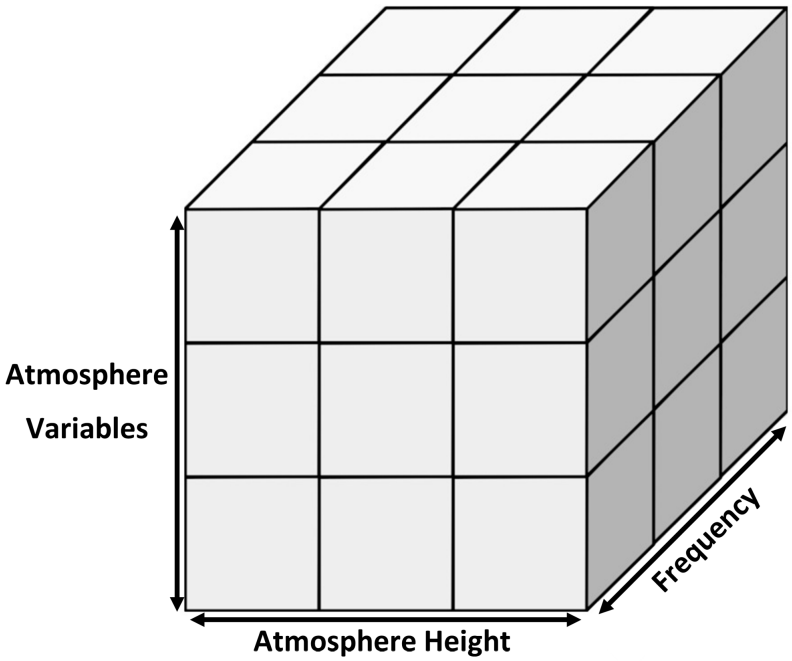

FIGURE 3.14: Atmospheric effects array conceptualization.

Therefore, the calculation of the specific gaseous attenuation and phase dispersion becomes simple to determine. As illustrated in figure 3.15, initially it is determined the frequency for which the attenuation and dispersion will be calculated.

Within that frequency, it will be calculated the specific gaseous attenuation and phase dispersion that each layer will induce on the transmitted signal, represented in green in figure 3.16, being the total specific gaseous attenuation and phase dispersion, for the considered frequency, the sum of contributions from all layers.

The total of frequencies for which specific gaseous attenuation and phase dispersion needs to be calculated will be defined by the size of the signal array on its frequency domain, since every frequency on the range between $f_{carrier} - \frac{bandwidth}{2}$ and $f_{carrier} + \frac{bandwidth}{2}$ will be affected.

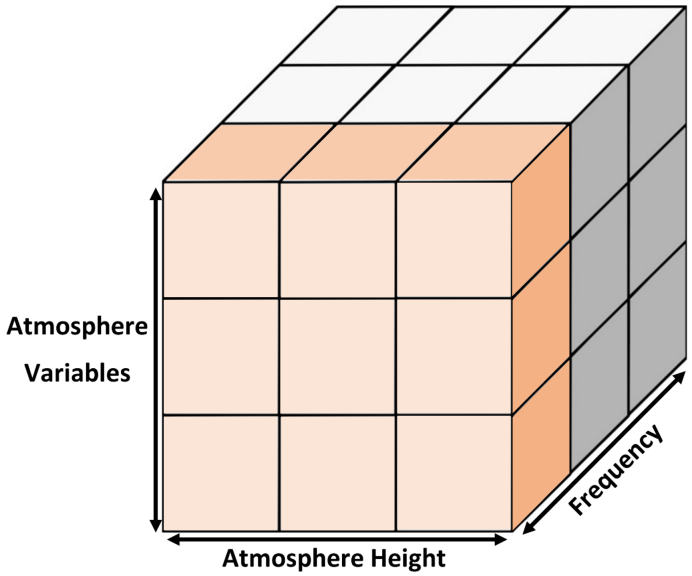

FIGURE 3.15: Atmospheric effects array considered frequency.

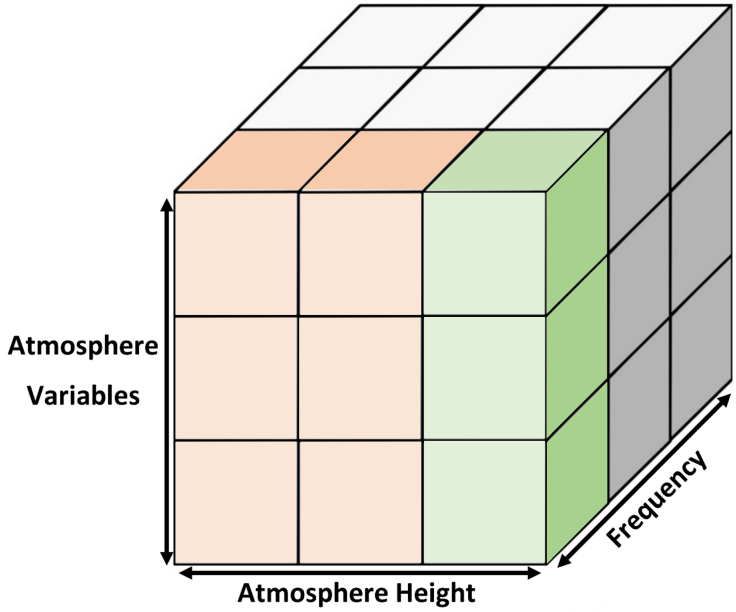

FIGURE 3.16: Atmospheric effects array considered height.

In figure 3.17 and 3.18 is possible to see the calculated atmospheric effects that will affect a radar pulse during its propagation for the ATLAS radar and also for a wide frequency which is from 0 Ghz to 100 GHz

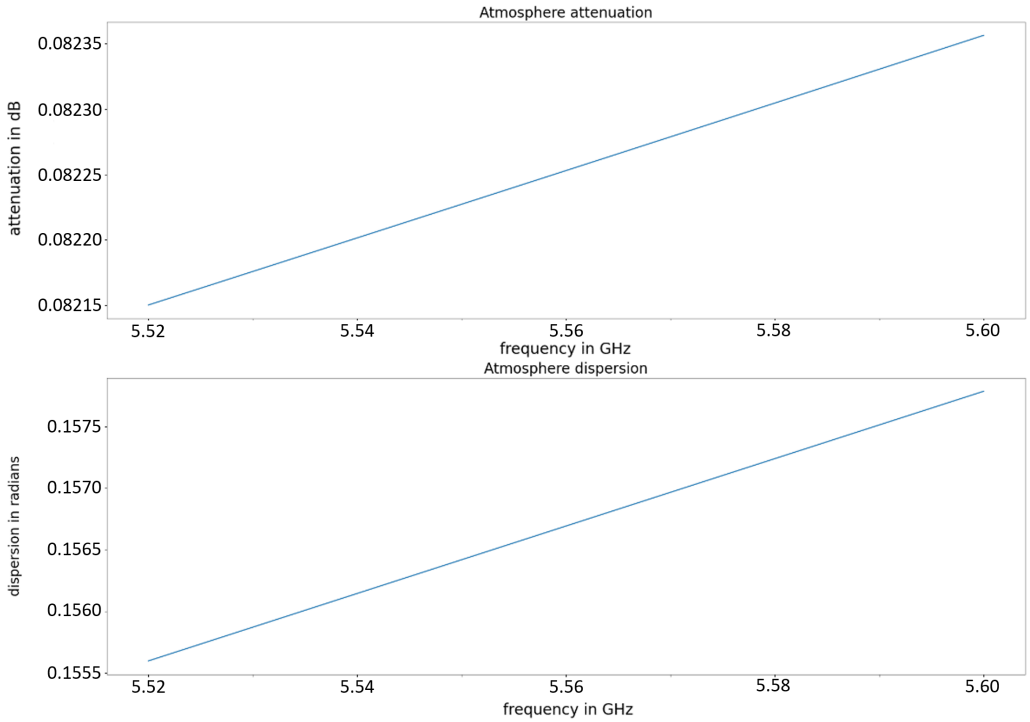

FIGURE 3.17: Atmospheric effects calculated for ATLAS bandwidth.

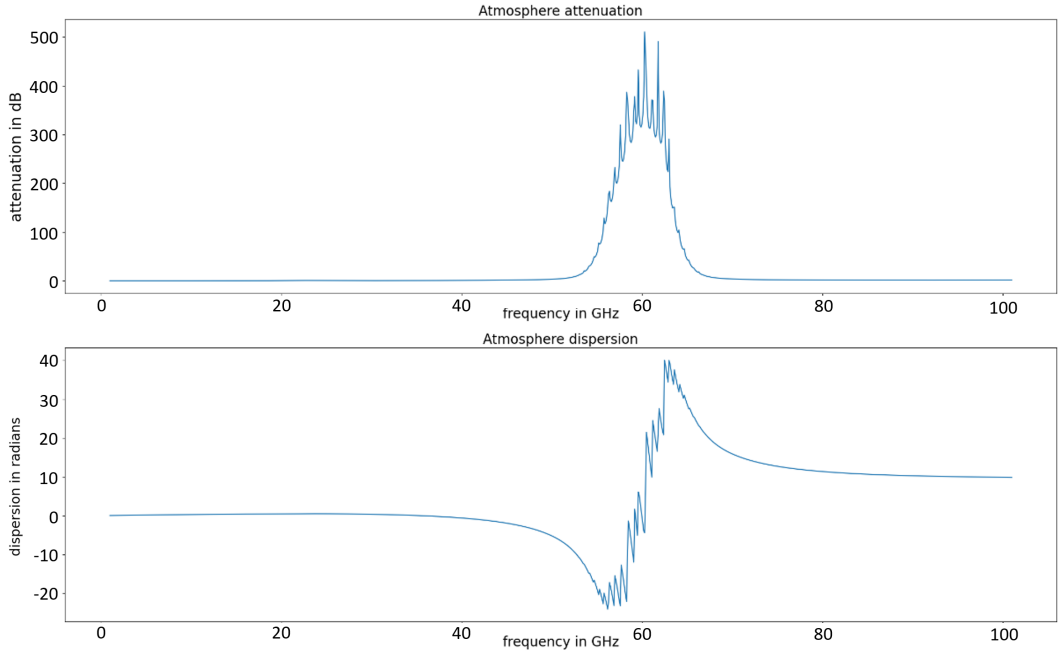

FIGURE 3.18: Atmospheric effects calculated for a 100GHz bandwidth.

Ionospheric Effects

On the other hand, to calculate the ionospheric effects induced on the transmitted signal during its propagation there is no need to divide the atmosphere into layers, which makes unnecessary the creation of a three-dimensional array, instead only a two-dimensional array will be created, where the columns represent the frequency for which the ionospheric effects are being calculated, being the first row that frequency, the second row it is the Faraday rotation and the last row is the group delay, as represented in figure 3.19, therefore the ionospheric effects will be calculated column by column, for each frequency.

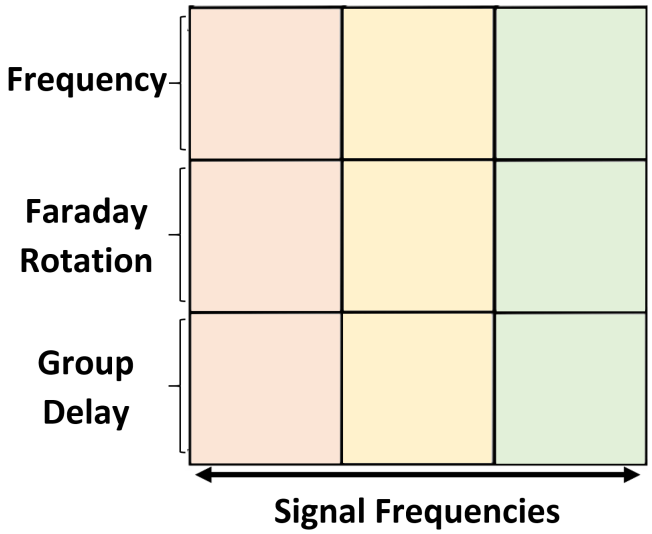

FIGURE 3.19: Ionospheric effects array.

For that calculation, the only variable needed is the TEC. With the objective of determine the TEC value, recommendation ITU-R P.531-14 [22] mentions a method that can be used to calculate it, using an existing database, which requests some of the inputs collected by the main script, such as: the azimuth and elevation to which the radar points, the target expected height, the season of the year and time of day for which the simulation is being made.

Unfortunately, it was not possible to use the original code considering that it was written in Fortran 77 and there are no longer any compilers for it. There was also an attempt to create a script that would automatically link the simulator to the online version of the model and thus get the TEC value, but this attempt would have high similarities with a hacking attack to the site, making it impossible to apply. A important note to add, is that this lack of discrimination is not imperative considering the low influence that ionospheric effects have in this bandwidth. This

fact is proven by figure 3.20, that is computed for a ionosphere with a high TEC and by figure 3.21, that is computed for a ionosphere with low TEC, showing that the signal would have a Faraday rotation of 0.0145 radians on the worst case scenario, so if a different TEC value was admitted, the resulting difference could be negligible.

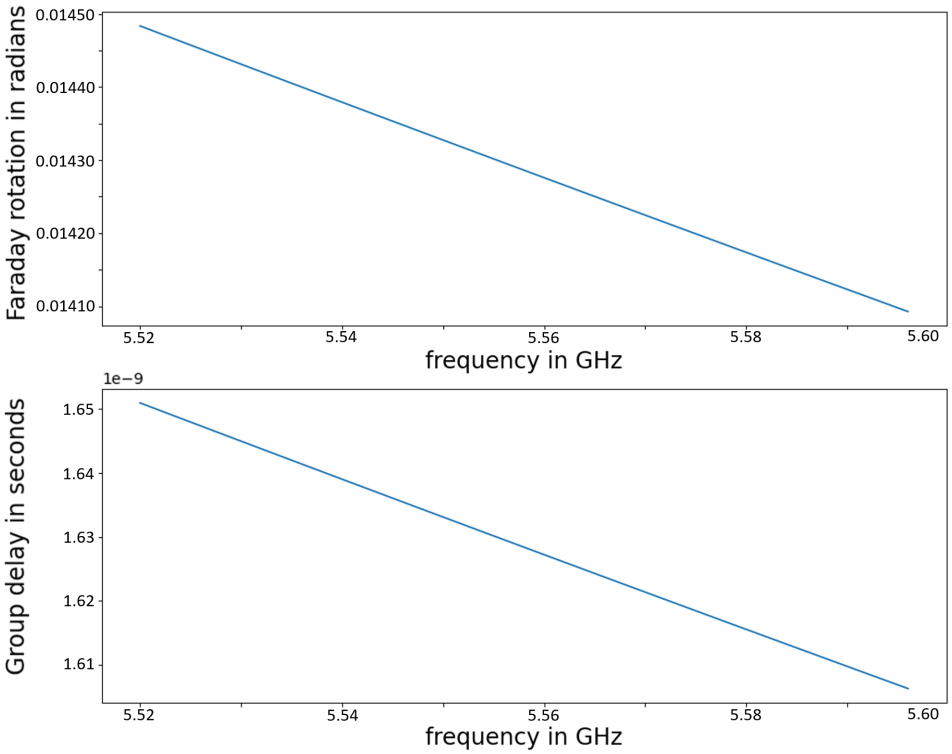

FIGURE 3.20: Ionospheric effects calculated for a high electron density ionosphere.

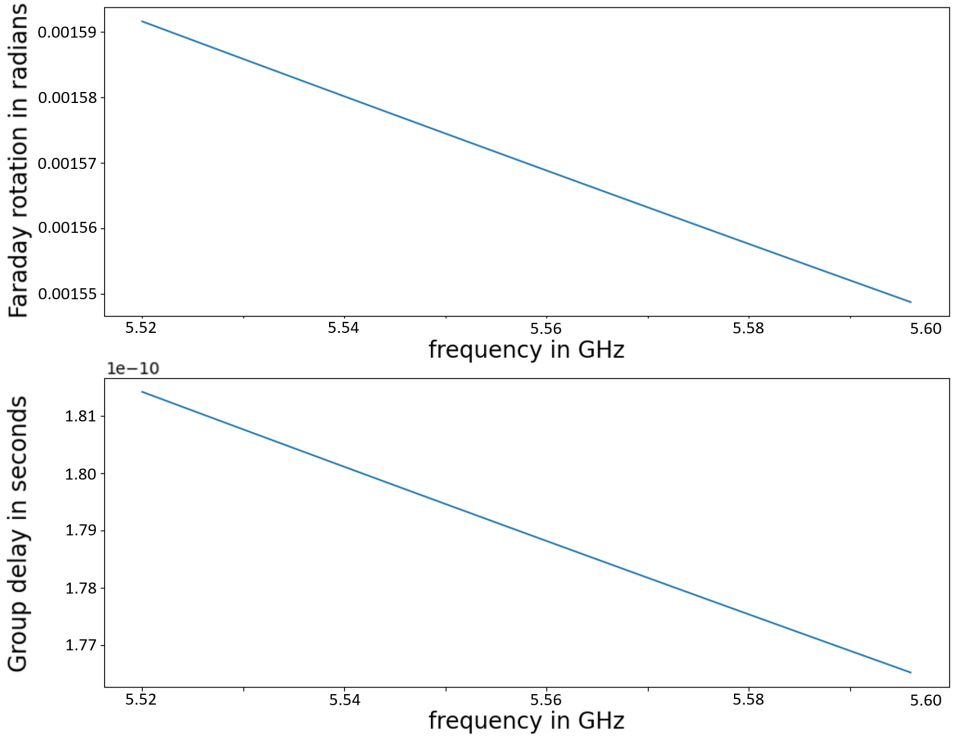

FIGURE 3.21: Ionospheric effects calculated for a high electron density ionosphere.

The implemented solution was the creation of a database in Excel, using the online model [30] and simulate it manually, keeping fixed the values related to the location of the radar, which are represent in green in figure 3.22 (those values were established considering the ATLAS radar of Pampilhosa da Serra) and changing the remaining variables, represent in red in figure 3.22 also:

- Antenna azimuth, starting from 000 to 330, with steps of 30º.
- Antenna elevation, starting from 10º to 90º, with steps of 10º.
- Target Height, starting from 500km to 1300km, with steps of 200km.
- Two months, January and July, which represent winter and summer respectively.
- Four different hours, 06h, 12h, 18h and 24h.

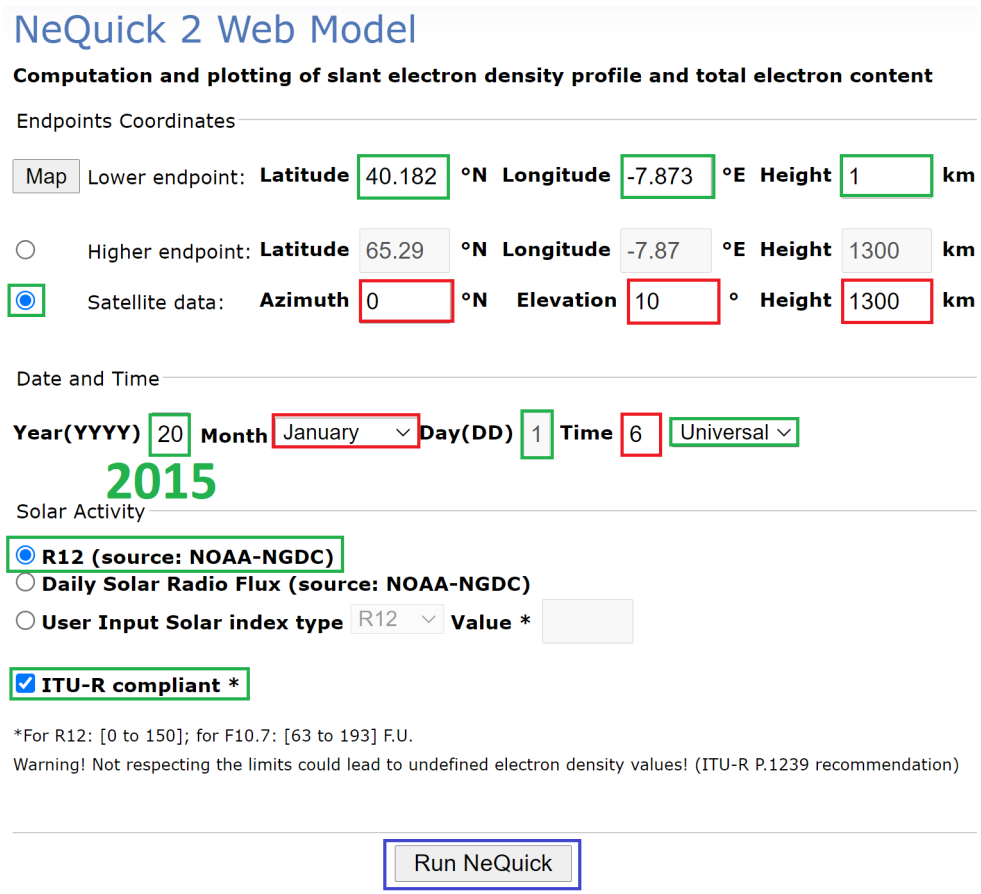

FIGURE 3.22: NeQuick2 web model.

The user will only have to input those variables using the considered values for the creation of the database in excel and then the script will access database and save the TEC value, allowing that way the determination of the ionospheric effects described in 3.3.3.

Tropospheric Effects

The method used to calculate the excess path length is a combination of the one used on the calculation of atmospheric effects with the one used on the calculation of ionospheric effects. This time, it was necessary to stratify the troposphere in layers in order to calculate the excess path length that each one of those layers would impinge on the transmitted signal, due to having a refractive index greater than one.

Consequently, a two-dimensional array was created (figure 3.23) in order to calculate the refractive indices and the excess path length for each layer, using the

method described in 3.3.4, and then adding sequentially the obtained value to the previous ones, determining that way the total excess path length.

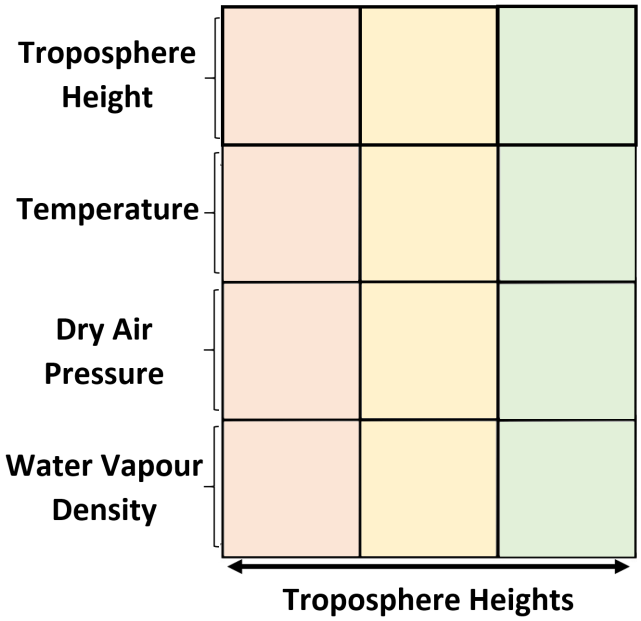

FIGURE 3.23: Tropospheric effects array.

Free-Space Attenuation

The attenuation from free-space propagation, described in 3.3.1 is calculated sequentially for the frequencies between ($f_{carrier} - \frac{bandwidth}{2}$ to $f_{carrier} + \frac{bandwidth}{2}$), using the inputs given on the main script relative to the antenna elevation, target altitude and its RCS.

Prosecution of the Determined Propagation Effects

Having already calculated all effects caused by the propagation of the radar signal through the atmosphere, it is now necessary to apply them to the initially transmitted signal. For this, those effects divided into two categories: those that affect the signal amplitude and those that affect the signal phase.

Relatively to the amplitude, from the initial amplitude components obtained from the FFT of the transmitted signal, we have subtracted twice the amplitude of the attenuation from atmospheric gases and once the amplitude of the attenuation from free-space propagation, thus obtaining the amplitude spectrum of the received signal.

On the other hand, relatively to the phase, from the initial phase components obtained from the FFT of the transmitted signal, we added twice the phase

obtained from the Faraday rotation, converted the group delay (in seconds) into distance and consequently into wavelengths relative to the considered frequency and add it twice, converted the excess path length (in meters) into wavelengths relative to the considered frequency and added it twice and, finally, added twice the dispersion obtained from the influence of atmospheric gases.

3.4.4 Signal Reception

Signal Inverse Fast Fourier Transform

In this phase of the simulation, it was already quantified all propagation effects that will affect the radar signal, so the main objective at the moment will be to be able to interpret the received signal, a process that will be done when we determine the received signal on its time domain from its own frequency domain.

Using the Inverse Fast Fourier Transform (IFFT), it is possible to transform the signal' frequency domain to its temporal domain, thus allowing the visualization of the simulated received signal and to carry out tests with it, specifically with the ATLAS radar receiver. In figure 3.24 it is illustrated a received signal on its time domain having a SNR of -32dB.

SNR Calculation

The last step in order to correctly determine the time domain of the signal that will reach the receiver is the calculation of the SNR, which is defined as the ratio between the total energy of the received signal and the noise power per unit bandwidth of the receiver [31]. This calculation makes possible the addition of the white gaussian noise that characterizes the atmosphere to the clean received signal. There are several ways to calculate the SNR, but we chose the one already used by the ATLAS project developers [15], which is

$$SNR = \frac{P_{av} G^2 \lambda^2 \sigma n e(n) F^4}{4\pi^3 \tau f_p R^4 N_F k T B L_s} \ . \tag{3.29}$$

Considering the data available on distinct articles and papers, which refer only the peak transmission power P_t, and knowing that $P_t = \frac{P_{av}}{\tau f_p}$ [31], we used an adapted version of equation 3.29 given by

$$SNR = \frac{P_t G^2 \lambda^2 \sigma m e(m) F^4}{4\pi^3 R^4 N_F k T B L_s} \ , \tag{3.30}$$

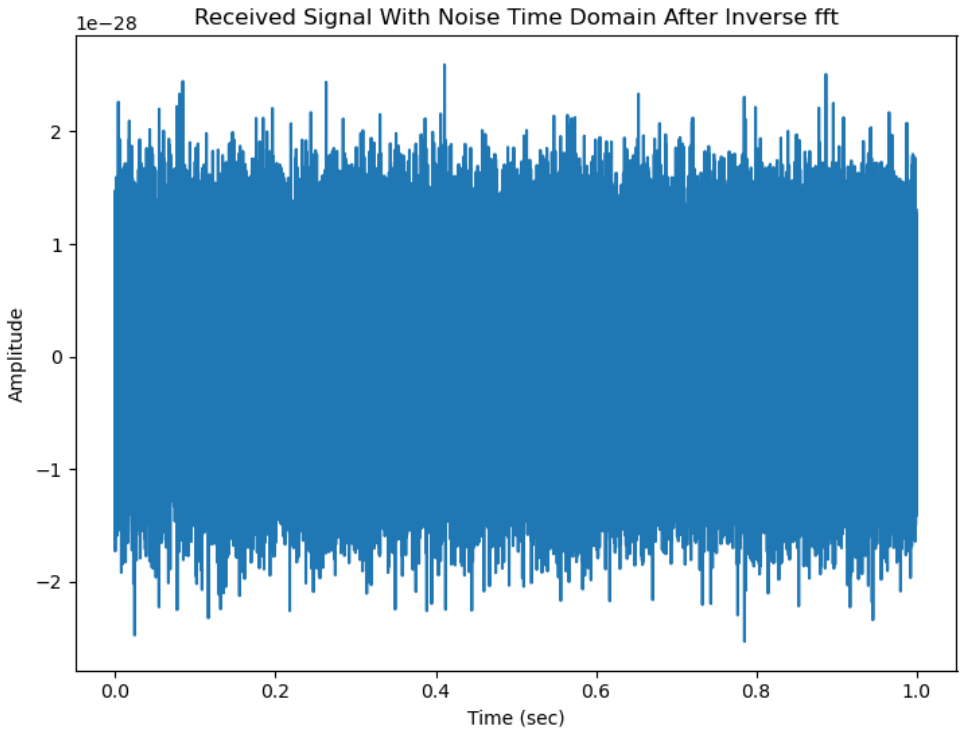

FIGURE 3.24: Received signal time domain after Inverse FFT.

where:

- P_t is the peak transmitted power (W).
- G is the antenna gain.
- λ is the signal wavelength (m).
- σ is the target RCS (m^2).
- m is the number of integrated pulses.
- $e(m)$ is the efficiency of the pulses integration.
- F is the propagation loss factor.
- R is the target distance (m).
- N_F is the receiver's noise factor.
- k is the Boltzmann constant ($J\,K^{-1}$).
- T is the receiver temperature (K).
- B is the receiver bandwidth (Hz).

- L_s is the system loss factor.

Having already calculated the SNR value, and knowing that the energy of a discrete time signal is given by

$$E_s = \sum_{n=-\infty}^{\infty} |x(n)|^2 \ , \tag{3.31}$$

it is possible to characterize the white Gaussian noise using a Gaussian/normal distribution, as represented in figure 3.25, where μ represents the distribution mean and σ represents the standard deviation.

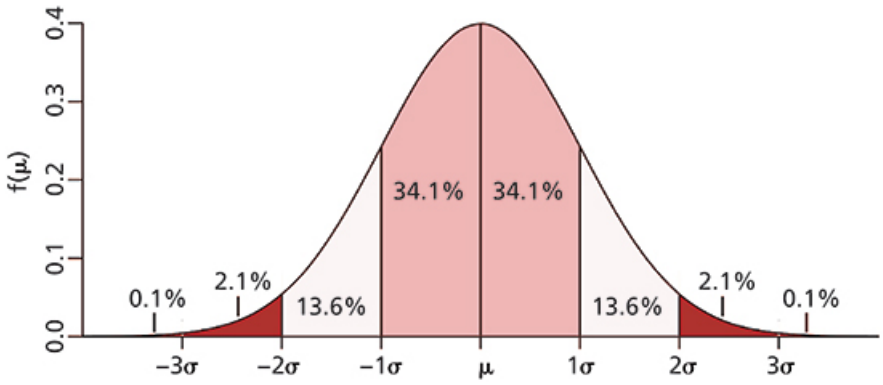

FIGURE 3.25: Gaussian distribution.
Source: https://www.chromatographyonline.com

With this objective, we defined the distribution mean $\mu = 0$ as we want as many positive amplitude noises as negative ones. In order to determine the standard deviation, we followed

$$\sigma = \sqrt{\frac{E_s}{N_{frequencies}} \times \frac{1}{SNR}} \ , \tag{3.32}$$

where:

- E_s is the received signal energy.
- $N_{frequencies}$ is the number of discrete frequencies that characterize the received signal.

With this approach, it is possible to simulate the white Gaussian noise relating it on the energy of the received signal, as well as the intended SNR ratio, which will be afterwards added to the clean received signal, generating that way the correct and accurate received signal.

Numerical Assessment of Simulation Tool

The most used tool to process and determine the quality of the received signal is the ambiguity function, already referenced in chapter 2.3.2.

Considering the fact that targets in orbit with a defined speed were not contemplated, merely static targets, it was decided to use only one of the one-dimensional cuts of the ambiguity function, which was the zero-Doppler cut.

Using this tool, it is possible to calculate the response of the received signal in range. The zero-Doppler cut that we would like to get would have a main lobe as narrow as possible and low-amplitude sidelobes, so we would indisputably be able to affirm how far away the detected target would be, as well as having a high level of confidence that no sidelobe would hide a lower amplitude received signal.

In figure 3.26 is possible to see the zero-Doppler cut of the received signal, which as computed for a carrier frequency of 5.56 GHz, a bandwidth of 80 MHz, a PRF of 2000Hz and a duty cycle of 40%, detecting a target with a RCS of 1 m^2 at a distance of 900 km from the antenna, resulting on a SNR of -32dB, which demonstrates how useful pulse compression techniques can be, allow us to identify a target from a received signal with such low SNR.

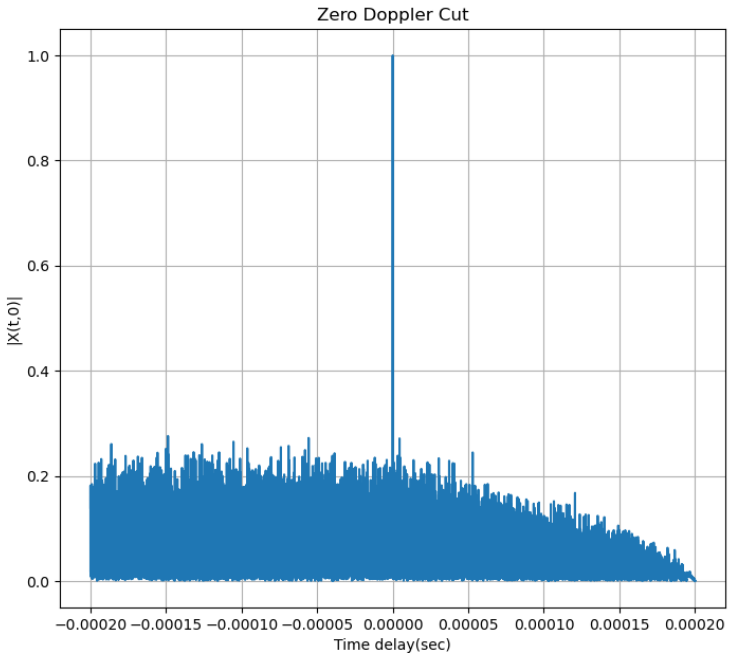

FIGURE 3.26: Received signal zero-Doppler cut.

3.5 Simulator Executable

Considering the versatility and usefulness of the simulator and also a possible future use of it by other users, we chose to create an executable file with it, which is available on the simulator's GitHub link [27]

The creation of this executable file carries some associated advantages:

- If others engineers wanted to make use of the simulator, they will not have to have a Integrated Development Environment (IDE) for Python, like Spyder, which was the IDE used during the development of this simulator. Instead they will just need to install the executable file on the computer and then install on the simulator folder all fundamental packages used, using the command-line interface. All these needed packages are described on the "requeriments.txt".
- The final exposed information is the only one that is necessary and its very summarized, thus avoiding the obtainment of several graphics that can later drop the user's efficiency in obtaining the truly important information.

The executable file uses the GUI exhibited on section 3.4.1 as an interface with the user, showing in the end of the simulation a output figure as represented in figure 3.27 and 3.28, which shows exactly how simply and resumed it is the displayed information.

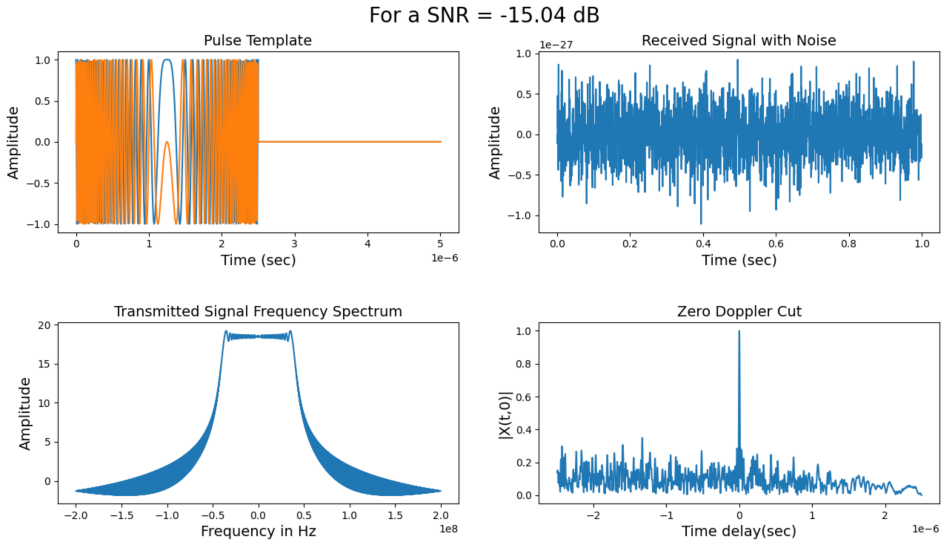

FIGURE 3.27: Simulator output figure with a low SNR simulation.

It is also important to mention if the user wants to access all the simulator's source code more deeply, especially the graphics related to the atmospheric

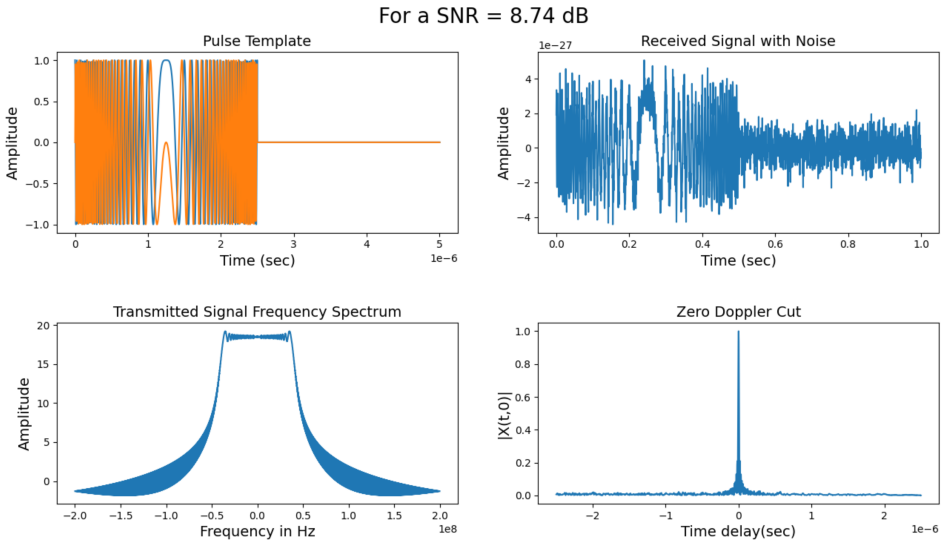

FIGURE 3.28: Simulator output figure with a high SNR simulation.

propagation effects, it is still possible to do it, as all the source code comes with the executable.

Chapter 4

Experimental Results

With the conclusion of the development of to Earth-Space propagation simulator, the main objective would be the comparison of the simulator results with a real detection. Unfortunately, due to the global pandemic that affected the entire population and technological sectors, there were delays during the obtainment of materials by the companies in charge of the production of certain components of the radar, namely the power amplifiers, thus making it impossible to complete the assembling of the radar, and consequently the possibility of carrying out real detections.

4.1 Signal Reception Simulation

The implemented solution was the use and test of the radar receiver circuit, benefiting from the features of an Arbitrary Waveform Generator (AWG), which permitted us to inject the simulated received signal into the receiver circuit, thus allowing the acquisition and understanding of specific concepts related to the radar functionality.

Firstly, it is necessary to generally know the constituents of the ATLAS radar [15] (figure 4.1), which are:

- 1 - Reference module: Where the clocks used to produce the 5.56 GHz carrier wave are, which also allows phase coherence between the carrier generated in the radar transmitter and the carrier generated in the AWG, making use of a 100 MHz output port that is shown in the bottom left corner of figure 4.2.
- 2 - Receiver circuit: Through RF-in connected to the antenna, the received signal will reach the receiver circuit, where it will be downconverted to the baseband and separated into its respective phase and quadrature components.

- 3 - Transmitter circuit: Where the 5.56 GHz carrier wave is generated, being afterwards passed through the RF-out connected to the power amplifier, which then connects to the antenna.
- 4 - Controller board: Where all the system software is kept, and is responsible for the configuration of the waveform, for number of pulses, for the activation/deactivation timings of the transmitter/receiver circuit, and other managing tasks.
- 5 - Data acquisition board: Conversion of the signal phase and quadrature components from analog to digital, frequently controlled by an external trigger from the AWG, which guarantees the correct synchronisation.

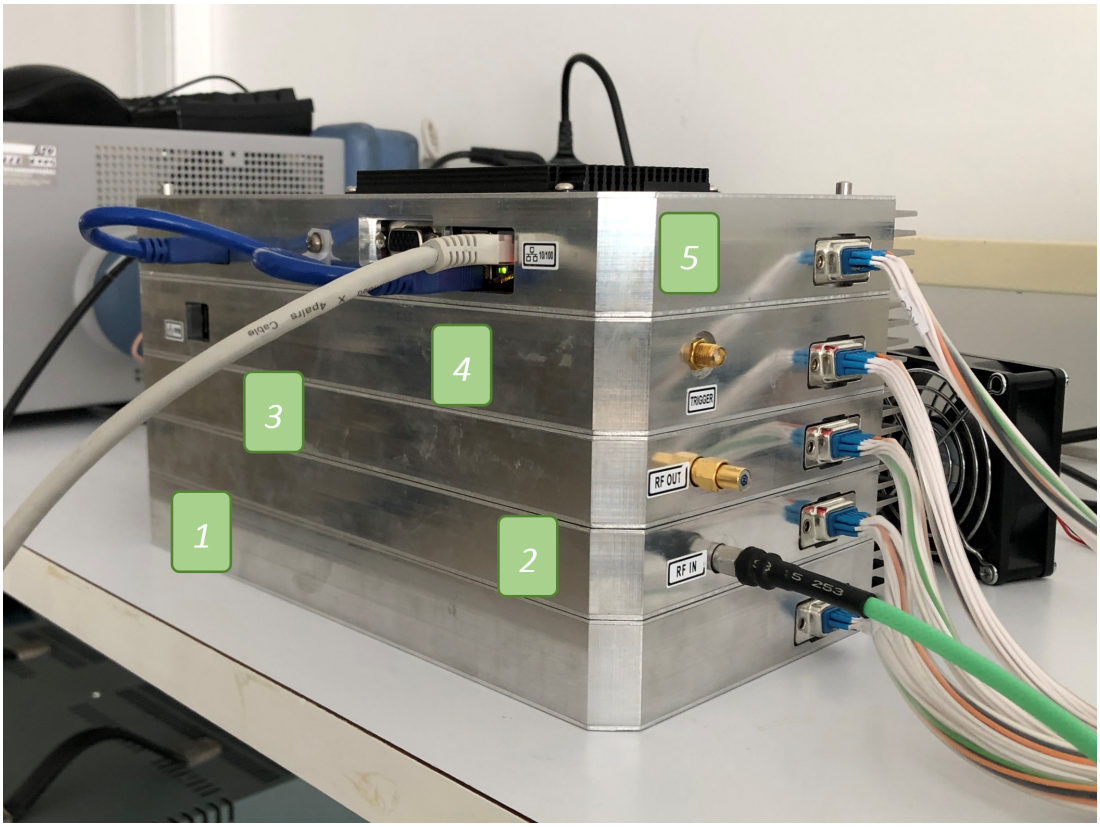

FIGURE 4.1: ATLAS Radar.

In figure 4.2 it is shown how the different modules are connected between each other, where we should give special attention to the 100 MHz output port in the bottom left corner and the input trigger in the C pin at the top, as previously mentioned.

For a better understanding of the radar structure, in figure 4.3 it is possible to see the ATLAS block diagram.

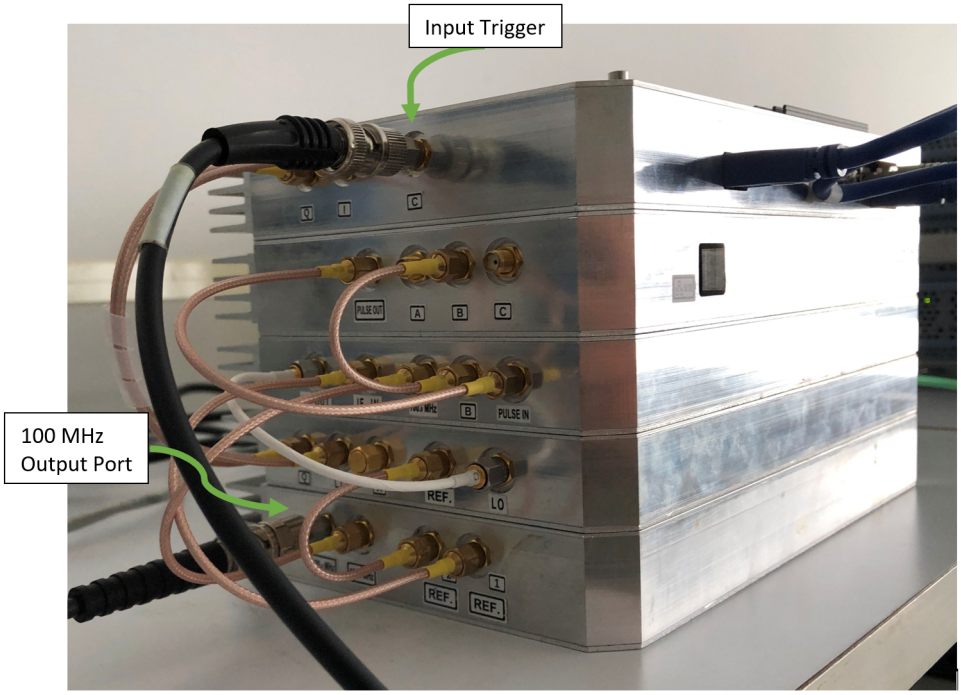

FIGURE 4.2: ATLAS Radar.

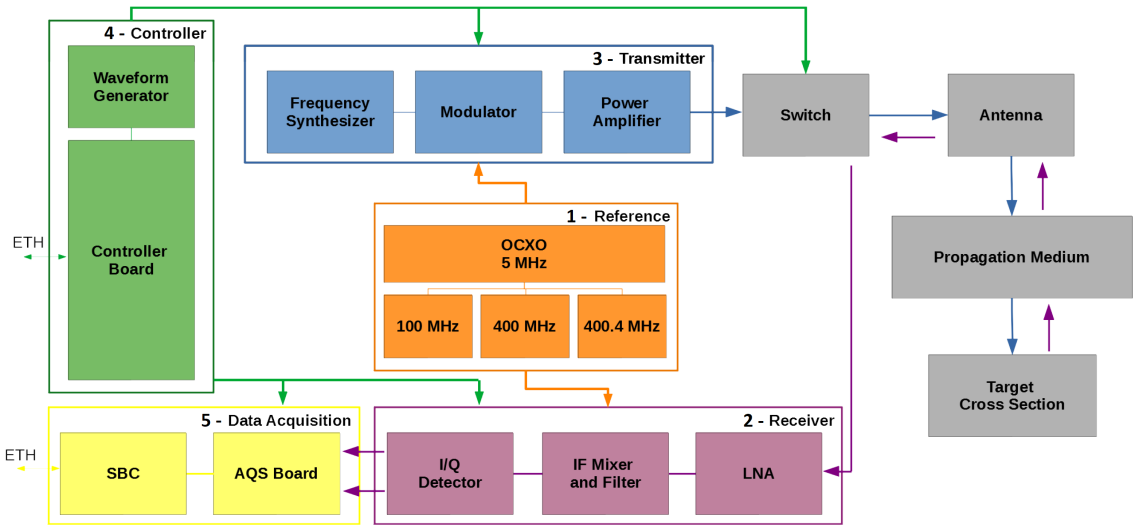

FIGURE 4.3: ATLAS block diagram.
Source: Obtained from [15]

where:

- Oven-Controlled Crystal Oscillator (OCXO).
- Intermediate Frequency (IF).
- Low Noise Amplifier (LNA).

- Single Board Computer (SBC).
- Acquisition Board (AQS).

For the following tests, the Earth-space propagation simulator was used in order to determine the received signal without any white Gaussian noise added to it. For each of the following scenarios, two different timings of simulation were considered, one in which the atmosphere is characterized by the summer season and have a high concentration of electrons (the first three simulations), and another in which the atmosphere is characterized by the winter season and have a low concentration of electrons (the last three simulations). Subsequently, within each three simulations, the distance and target RCS were changed in order to evaluate what these features can change on the detection of space debris. All simulation features are clearly described in appendix A, such all zero-Doppler cuts calculated.

Considering that the inputted signal on the AWG is normalized and unmixed with white Gaussian noise, in order to achieve the previously calculated SNR for each one of the pulses, the required attenuators were attached to the AWG RF-output, which are highlighted in yellow in figure 4.4. It is also very important to contemplate the intrinsic noise floor of the receiver, which in this case is -94dBm, meaning that if the determined SNR was of -25dB, it is necessary to add attenuators capable of producing a attenuation of 119dB.

FIGURE 4.4: Simulation setup.

Figure 4.5 demonstrates the ease with which the signal reception simulation is performed, being only necessary to work with the AWG.

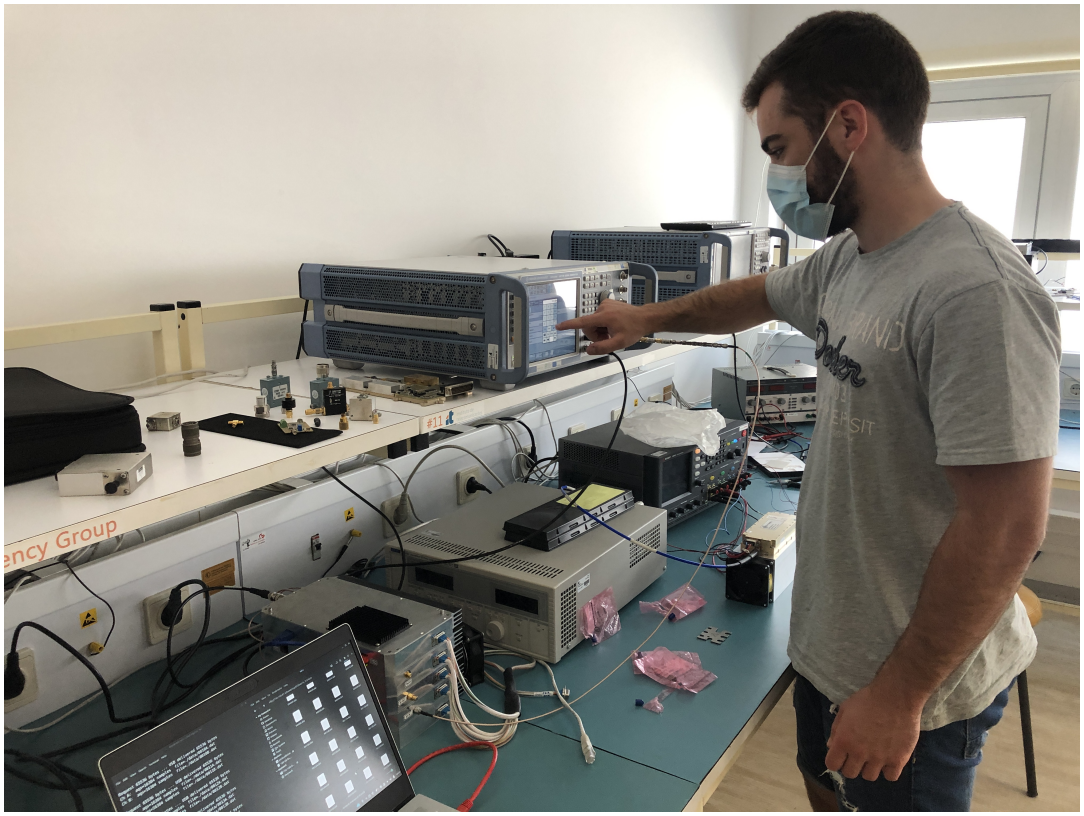

FIGURE 4.5: Simulations with the receiving circuit.

LFM on the ATLAS Case Scenario

As previously referenced in chapter 3, ATLAS transmits pulses with a carrier frequency of 5.56 GHz with a bandwidth of 80 MHz. Unfortunately, the used AWG just supports sampling frequencies up to 100 MHz and in order to have a even higher ratio than the one referenced on the Nyquist theorem, where the sampling frequency must be at least two times higher than the signal frequency, we chose to settle the bandwidth to 20 MHz and the sampling frequency to 100 MHz.

For this scenario, we present two zero-Doppler cuts, corresponding to the simulations with the highest (figure 4.6) and lowest (figure 4.7) calculated value of SNR. The simulation with the highest SNR (SNR = -7.16 dB) was obtained for a winter atmosphere and with a target with a RCS of 1 m^2, which was in a relative elevation of 90° to the antenna site and at 300 km of altitude. On the other hand, the simulation with the lowest SNR (SNR = -26.25 dB) was obtained for a summer atmosphere and with a target with a RCS of 1 m^2, which was in a relative elevation of 90° to the antenna site and at 900 km of altitude.

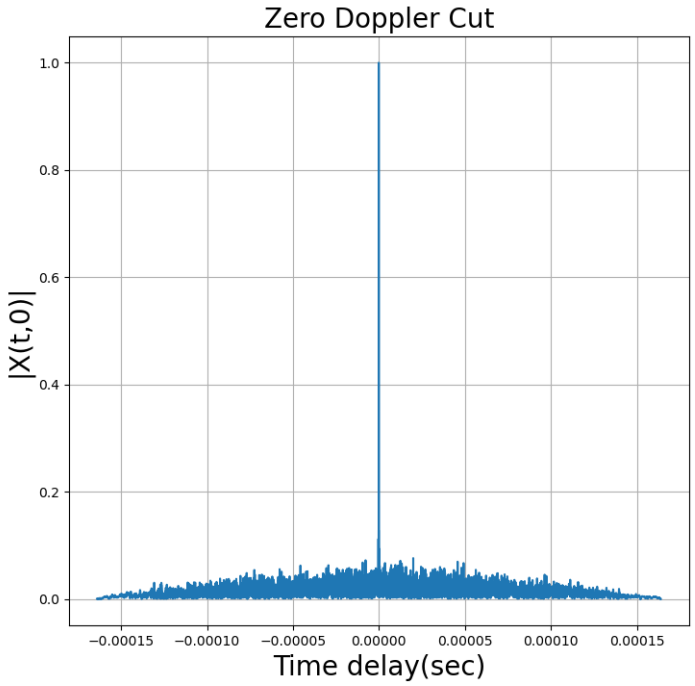

FIGURE 4.6: Zero-Doppler cut of a LFM signal for the ATLAS case scenario with SNR = -7.16 dB.

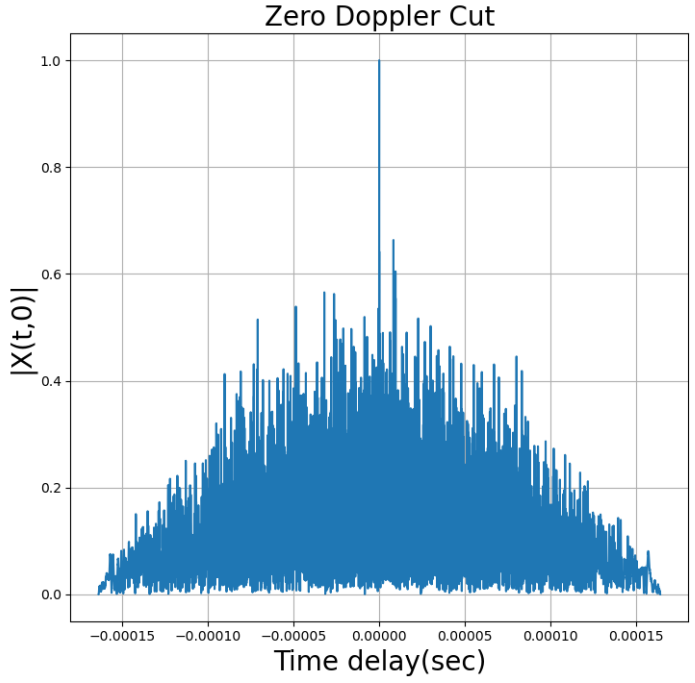

FIGURE 4.7: Zero-Doppler cut of a LFM signal for the ATLAS case scenario with SNR = -26.25 dB.

The obtained results, mainly the zero-Doppler cut acquired for a SNR = -26.25 dB (figure 4.7), demonstrate that there is a decent capacity to detect targets with a RCS of 1 m^2 at 900 km of altitude, which is practically the upper limit of height of LEO, while using a LFM pulse.

LFM on the Flores SST Case Scenario

Integrated on the Rede Atlântica de Estações Geodinâmicas e Espaciais (RAEGE) project, whose main objective is the construction and operation of a network of four Fundamental Geodetic Stations (FGS) in both Portugal and Spain, it was created in the Açores island of Flores (Lajes) a monopulse tracking radar [32]. This radar has a 13.2 meters diameter antenna with a gain of 64.32 dB, which transmits a carrier frequency of 16.7 GHz with a bandwidth of 610 kHz, having a transmitting peak power of 50 kW.

We will add the Flores SST study case as it offers different data, as for the antenna sites and even for the waveform characteristics, which will complement the analysis of experimental results from the simulator.

Considering the fact that this radar has much more favorable initial features for a effective target detection, such as its transmitting peak power and antenna gain, the obtained results show much higher SNR values than those previously obtained on the ATLAS case scenario. Thus we present two zero-Doppler cuts that were simulated for the same scenario (target with a RCS of 1 m^2, in a relative elevation of 90° and at 900 km of altitude) except for the chosen season atmosphere. In figure 4.8 it is represented the zero-Doppler cut that was obtained on a simulation carried out for a winter atmosphere, which resulted on a SNR = 25.64 dB, and on figure 4.9 it is represented the zero-Doppler cut that was obtained on a simulation carried out for a summer atmosphere, which resulted on a SNR = 25.07 dB.

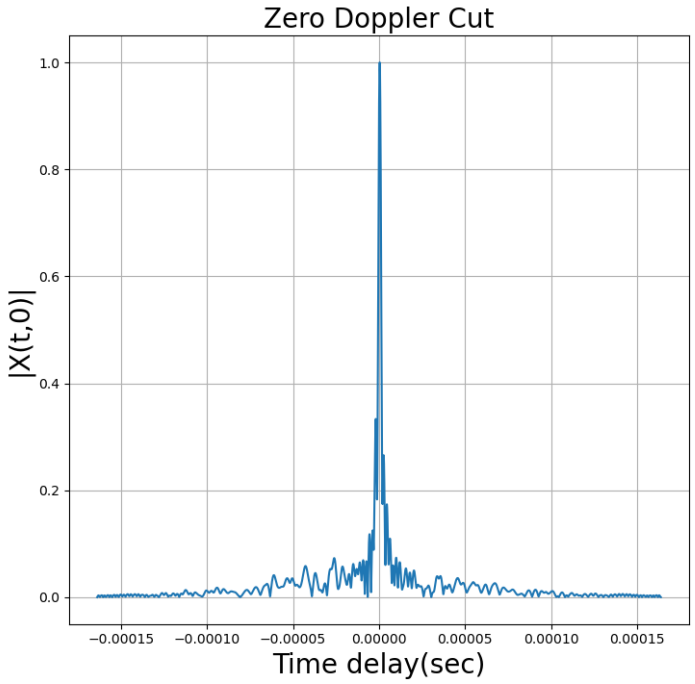

FIGURE 4.8: Zero-Doppler cut of a LFM signal for the ATLAS case scenario with SNR = 25.64 dB.

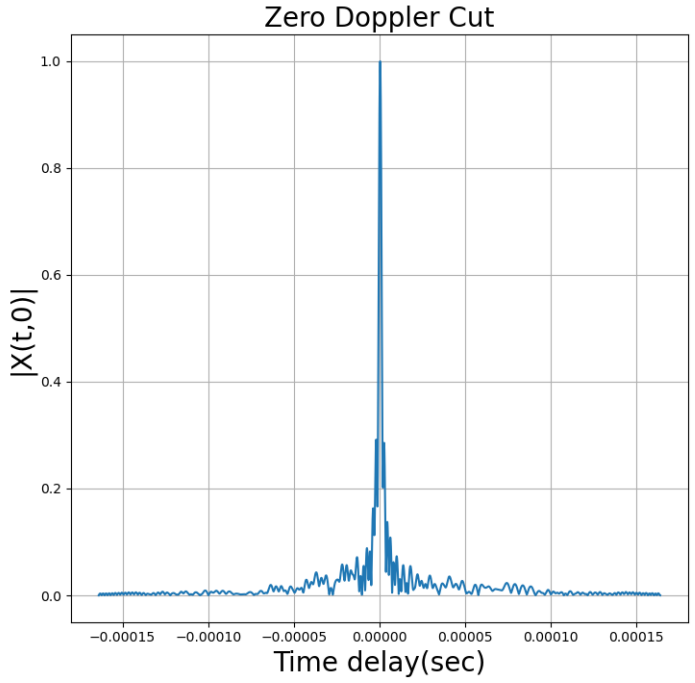

FIGURE 4.9: Zero-Doppler cut of a LFM signal for the ATLAS case scenario with SNR = 25.07 dB.

Regardless of the initial conditions from the radar system, with these simulations it was possible to verify that it is not only important to quantify the losses imposed on the radar signal using a uniform atmosphere along the path, but also study the temperature, water vapor density and pressure values, which will also influence the obtained results. This difference was also leveraged by the carrier frequency, which is higher and suffers more atmospheric attenuation, resulting on a difference of 0.57 dB between the simulation for summer and winter, considering the standard atmosphere used for each season.

LFM on a Highly Attenuating Atmosphere Case Scenario

In order to verify the influence of the carrier frequency on the atmospheric attenuation that affect the radar signal during its propagation, we chose to perform other simulations using all the features previously used in the ATLAS case scenario, changing only the carrier frequency from 5.56 GHz to 22 GHz, which is a frequency close to 22.235 GHz which corresponds to the frequency of the first water vapour spectral line.

As expected, all SNR values obtained are very low, so it is very difficult to get a zero-Doppler cut where we could distinguish a detection of a target. Consequently, identically to the Flores SST case, we show two zero-Doppler cuts that were simulated for the same scenario (target with a RCS of 1 m^2, in a relative elevation of 90° and at 300 km of altitude) except for the chosen season atmosphere. In figure 4.10 it is represented the zero-Doppler cut that was obtained on a simulation carried out for a winter atmosphere, which resulted on a SNR = -21.33 dB, and on figure 4.11 it is represented the zero-Doppler cut that was obtained on a simulation carried out for a summer atmosphere, which resulted on a SNR = -26.01 dB.

Using a carrier frequency that is highly susceptible to atmospheric attenuation allowed us to verify, on a more expressive way, that the atmosphere used during the propagation simulation is determinant for the achieved SNR. In this case, we see again that the SNR obtained for winter is higher than that obtained for summer, but this time 4.68 dB higher, which means that the power of the received signal for the winter simulation will be approximately 2.94 times higher that the power of the received signal for the summer simulation. Nevertheless, we achieve such low SNR values, that we could just detect a target with a RCS of 1 m^2, in a relative elevation of 90° at 300 km of altitude, which is practically the minimum height of LEO, while using a carrier frequency so susceptible to atmospheric attenuation.

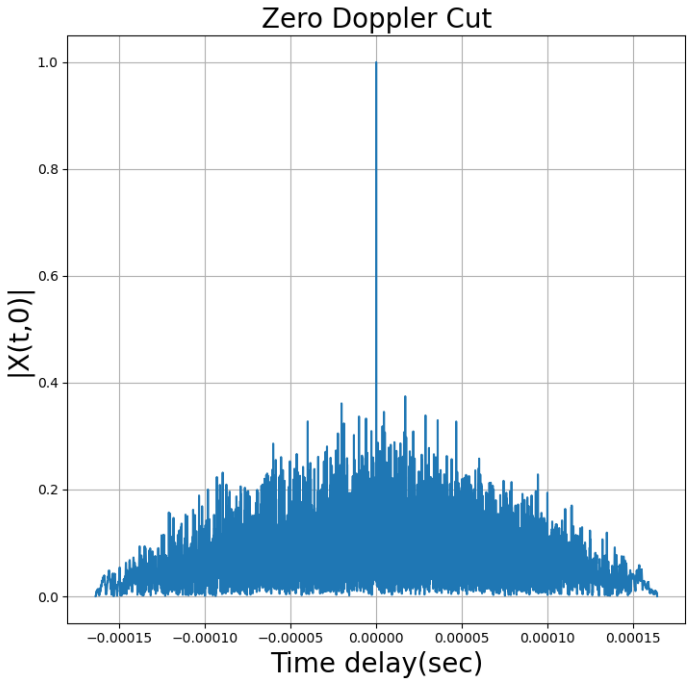

FIGURE 4.10: Zero-Doppler cut of a LFM signal for a Highly Attenuating case scenario with SNR = -21.33 dB.

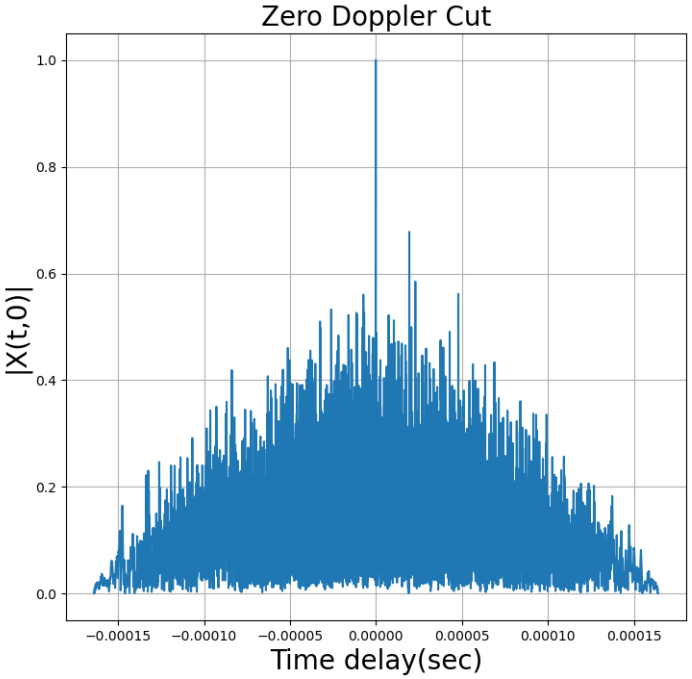

FIGURE 4.11: Zero-Doppler cut of a LFM signal for a Highly Attenuating case scenario with SNR = -26.01 dB.

LFM Train Case Scenario

In order to analyse now the LFM train pulse and the influence of its propagation on the atmosphere, we have performed other simulations using all the features previously used in the ATLAS case scenario, with the only difference of transmitting three pulses with a duty cycle of 50%, instead of only one pulse.

As expected, for the same propagation scenarios as the ones used on the simulations of only one LFM pulse transmission, all SNR values obtained were optimised as three pulses were coherently integrated. Thus we will show the two zero-Doppler cuts obtained for the same propagation scenarios of figure 4.6) and figure 4.7). This time, the simulation with the highest SNR went from -7.16 dB to -2.39 dB, and the simulation with the lowest SNR went from -26.25 dB to -21.48 dB, showing that the coherent integration of three pulses have optimised the SNR in 4.77 dB, which means that we have now received a signal with three times more power when compared with a single LFM pulse, as expected considering equation 3.30 in chapter 3.4.4. The zero-Doppler cut obtained with the simulation with the highest SNR (SNR = -2.39 dB) is shown in figure 4.12), and the one obtained with the simulation with the lowest SNR (SNR = -21.48 dB) is shown in figure 4.13).

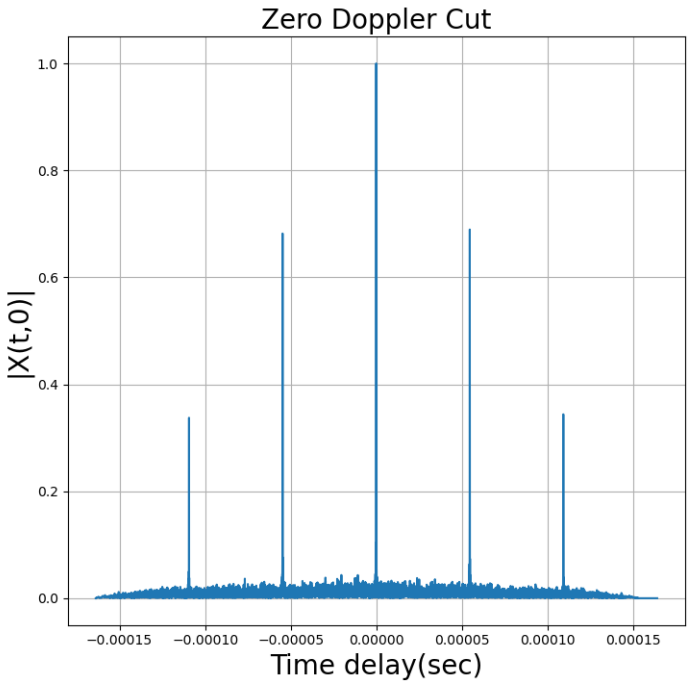

FIGURE 4.12: Zero-Doppler cut of a LFM Train signal with SNR = -2.39 dB.

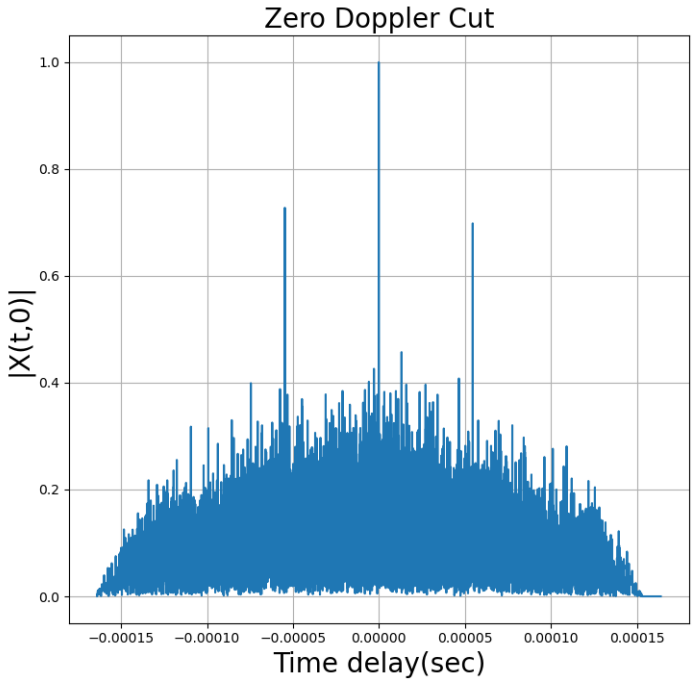

FIGURE 4.13: Zero-Doppler cut of a LFM Train signal with SNR = -21.48 dB.

Once again, we can confirm that using this pulse compression technique, we will be able to detect targets with a RCS of 1 m^2 at 900 km of altitude. In addition to the effectiveness of detection, is it also necessary to highlight that we could verify the bed of nails on both zero-Doppler cuts, as previously referred in chapter 2.3.3, confirming all analytical background of this pulse compression technique. We have performed these simulations with a PRF of 18310Hz, meaning that $PRI = \frac{1}{PRF} =$ 54.6µs, which is the value of time that separates the main peaks on both zero-Doppler cuts.

Stepped FM Case Scenario

For the stepped FM signal case, we used all initial features used on the LFM signal case, transmitting also three pulses per simulation, which resulted on the exact SNR values for each simulation. Therefore, the zero-Doppler cut obtained with the simulation with the highest SNR (SNR = -2.39 dB) is shown in figure 4.14), and the one obtained with the simulation with the lowest SNR (SNR = -21.48 dB) is shown in figure 4.15).

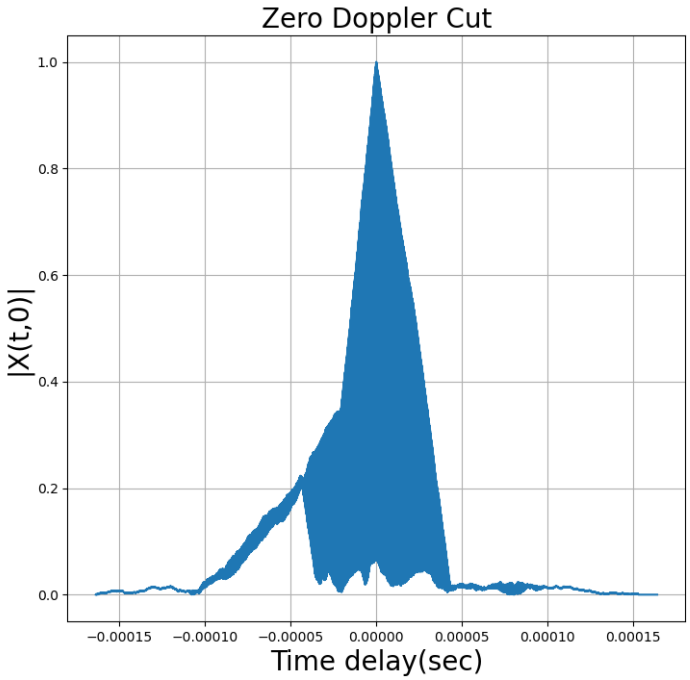

FIGURE 4.14: Zero-Doppler cut of a Stepped FM signal with SNR = -2.39 dB.

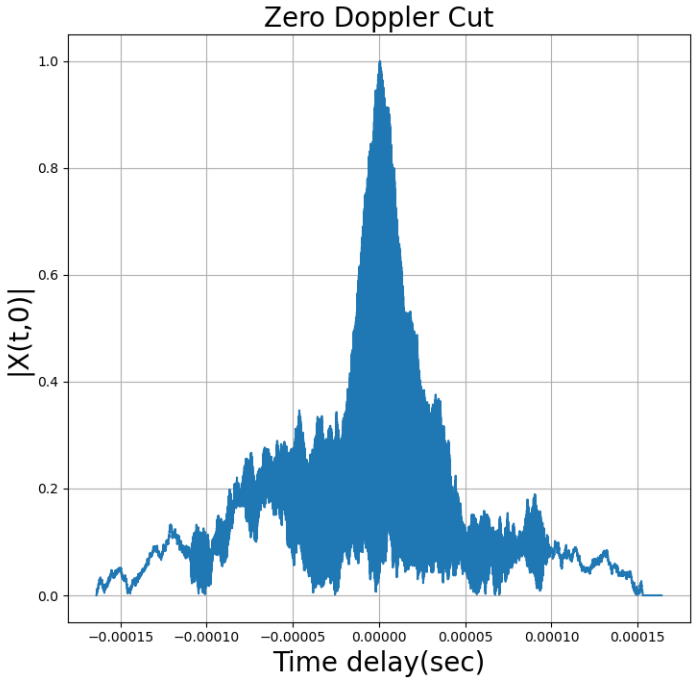

FIGURE 4.15: Zero-Doppler cut of a Stepped FM signal with SNR = -21.48 dB.

This pulse compression technique, considering that it consecutively changes the pulse frequency within an established bandwidth, presents a zero-Doppler cut with a triangular shape, which is a result of the integration of a train of non-identical pulses, showing a asymmetry that can also be explained by the fact that the middle pulse has a frequency of 0Hz and the radar data acquisition board has a cut-off frequency at 9 kHz, which makes it behave like a high-pass filter from this frequency. Although, it is obviously a better result than a zero-Doppler cut of an unmodulated pulse as it is as narrow in time as a zero-Doppler cut obtained with a LFM train signal. Nevertheless, it is fair to affirm that this technique can also effectively detect a targets with a RCS of 1 m^2 at 900 km of altitude.

Barker Codes Case Scenario

In the barker codes simulations, it was necessary to consider that the radar data acquisition board has a cut-off frequency at 9 kHz, it was necessary to add a sine wave with a frequency higher than 9 kHz to its baseband to be able to proceed with the simulations. For this pulse compression technique, we will show two zero-Doppler cuts obtained for the same simulation conditions, changing only the type of barker code used, thus obtaining the same SNR (SNR = -23.24 dB) for both cases. The zero-Doppler cut obtained for a Barker13 code is shown in figure 4.16 and the one obtained for a Barker5 code is shown in figure 4.17

With the presented results, we can affirm that the use of barker codes will allow us to make an effective detection of targets with a RCS of 10 m^2 at 900 km of altitude, but also that the higher the type of barker code used, the better the zero-Doppler cut obtained will be, as evidenced by the narrower main peak obtained while using a baker13 code when compared with the one obtained while using the barker5 code.

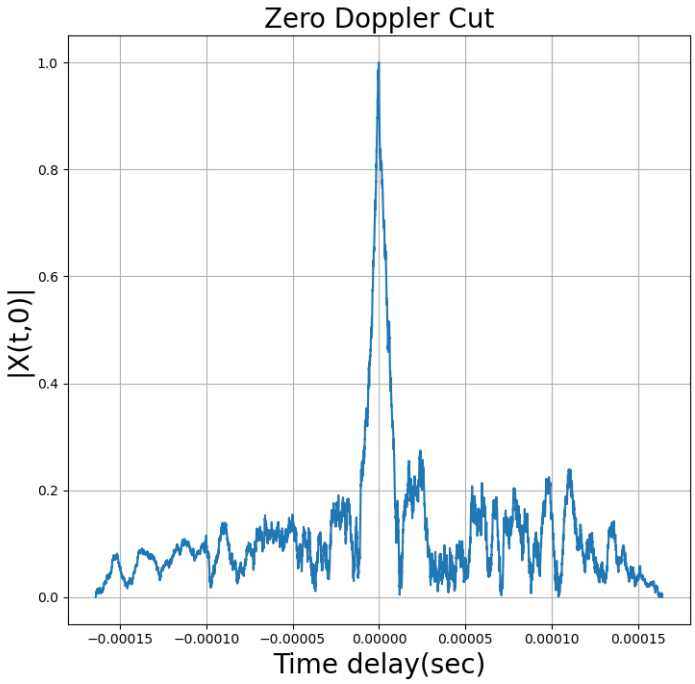

FIGURE 4.16: Zero-Doppler cut of a Barker13 signal with SNR = -23.24 dB.

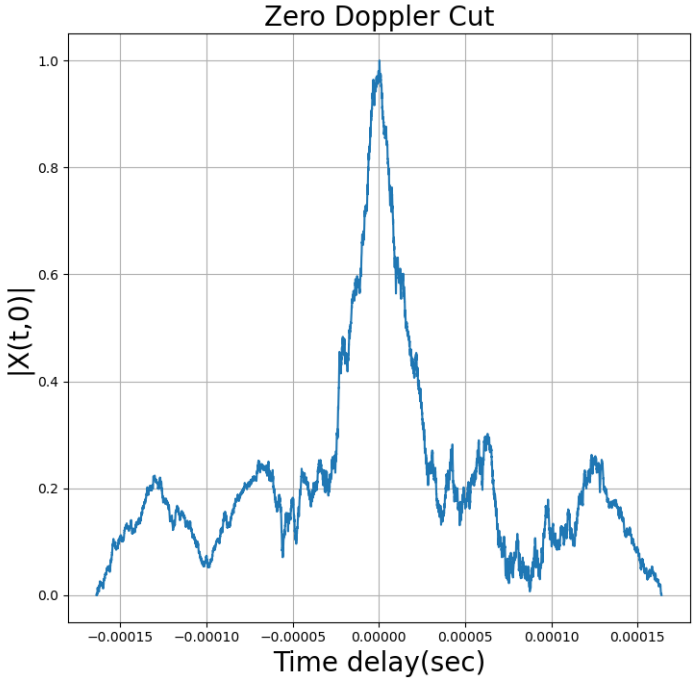

FIGURE 4.17: Zero-Doppler cut of a Barker5 signal with SNR = -23.24 dB.

Simulation Conclusions

With the obtained results, it is possible to verify that from all the considered effects, excepting obviously the attenuation caused by the propagation of the signal in free space, it is the atmospheric gases attenuation that has the most influence on the target detection effectiveness. For the studied frequencies, the dispersion introduced by ionospheric and tropospheric effects ends up not being relevant. Thus, the radar will be limited by the distance and dimension of the objects to be detected, where the SNR levels must not be less than sensibly -27 dB in order to be able to achieve a reasonable correlation between the transmitted and received signal.

4.2 True Positive Rate Determination

Another excellent approach that is used in several areas in order to quantify the performance of a system is the Receiver Characteristic Operator (ROC) curves and even the Area Under the Curve (AUC) of a ROC curve [33].

The ROC curve is a technique that is applicable for binary classification problems, which would be, in this case, the classification of a certain peak as being or not a target. It commonly plots on the horizontal axis the False Positive Rate (FPR) and the True Positive Rate (TPR) on the vertical axis, where the discrete values (illustrated in figure 4.18 through the five letters) for each iteration (where the threshold value is sequentially redefined) are linked, creating the ROC curve. The AUC exhibits the efficiency of a classifier to distinguish the target from noise and is used as a summary of the ROC curve.

In our case, remembering that in our simulator it is only considered a single target, it is tough to quantify the probability of true and false positives, making much more sense to calculate a curve that shows us what is the probability of detecting the target while taking into account the defined threshold as well as the SNR the radar signal will be subject.

To be able to determine these curves, a statistical analysis would have to be carried out with a large number of samples, so that the obtained results were as accurate as possible.

With this objective, it was created a script that makes use of the initially transmitted signal and the received signal without any added white Gaussian noise. Therefore, a range of SNR values was established, for which 101 discrete values

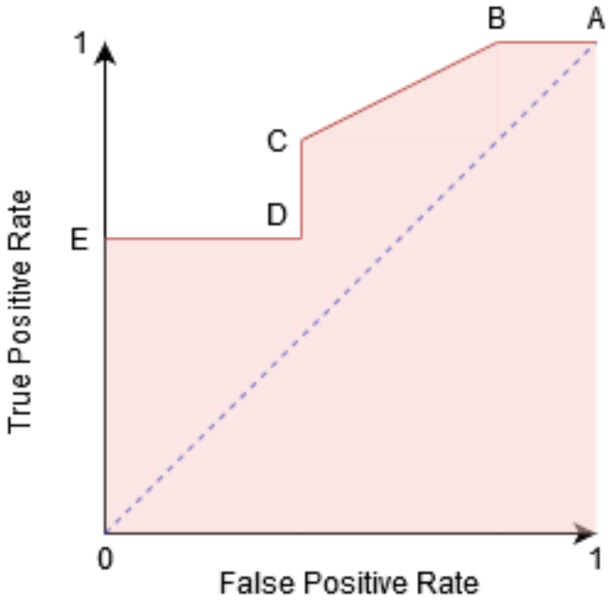

FIGURE 4.18: Receiver operator characteristic curve example.

were defined, and 1000 iterations were subsequently performed for each one of these discrete values, thus allowing a large amount of data to be analyzed.

Each of these iterations consisted of generating the white Gaussian noise in function of the SNR, adding it to the received signal and then performing the correlation with the transmitted signal. Since the noise will always have a different distribution, the zero-Doppler cut obtained will always have a different shape as well, thus making it possible to obtain the true positive rate, as some of the correlations will allow a clear distinction of the main peak, while others will not.

It is important to refer that for all of these simulations, we used higher values of PRF (described in table 4.1) in order to obtain received and transmitted signal arrays between 1000 and 2000 points. If we had simulated with the real values of PRF (ATLAS uses a maximum PRF of 30Hz [15]) we would have arrays with much more points, which would lead to better correlations between transmitted and received signal, resulting on higher TPR for lower SNR values.

TPR Simulation Data					
Pulse Compression Technique	Carrier Frequency	BW	PRF	Duty Cycle	Number of Pulses
LFM on ATLAS	5.56 GHz	80 MHz	200 kHz	100%	1
LFM on Flores SST	16.7 GHz	610 kHz	200 kHz	100%	1
LFM Train	5.56 GHz	80 MHz	1 MHz	40%	5
Stepped FM	5.56 GHz	80 MHz	1 MHz	40%	5
Barker5	5.56 GHz	-	200 kHz	100%	1
Barker13	5.56 GHz	-	200 kHz	100%	1
Unmodulated	5.56 GHz	-	10 kHz	100%	1

TABLE 4.1: TPR simulation data.

LFM on the ATLAS Case Scenario

In figure 4.19 it is shown the TPR for a LFM signal that is transmitted by ATLAS, computed for a carrier frequency of 5.56 GHz, with a bandwidth of 80 MHz, which demonstrates very satisfactory results, even when the noise power is 100 times higher than the received signal energy ($SNR = -20$dB), if a threshold value of 0.7 is considered, the target would be detected about 87% of the time.

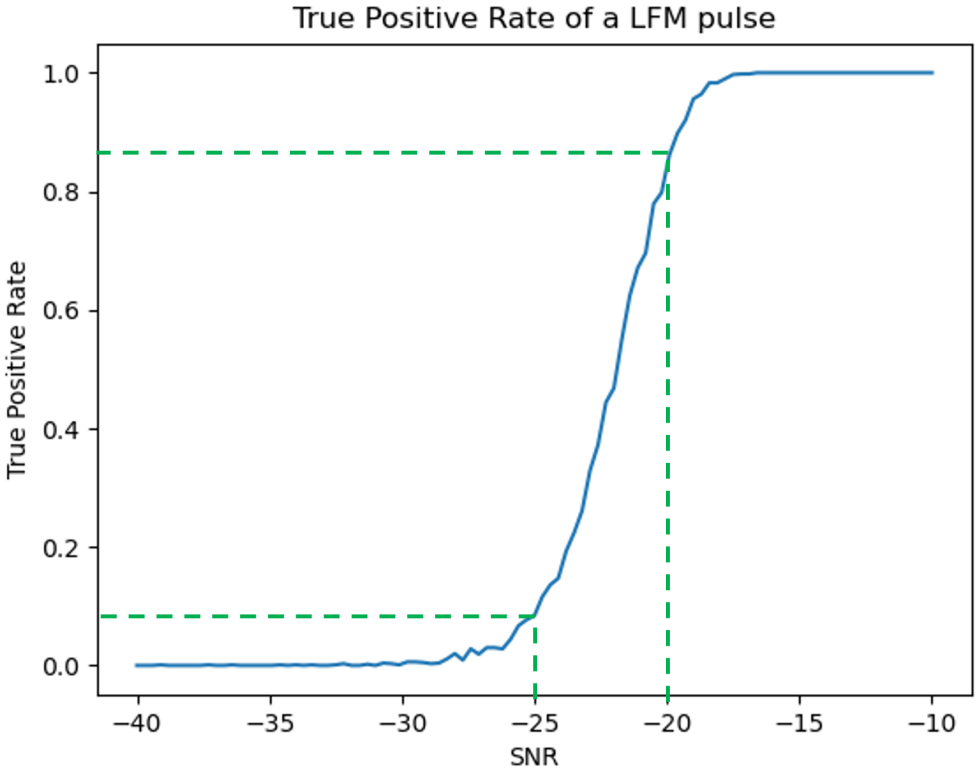

FIGURE 4.19: True Positive Rate for the ATLAS case scenario.

LFM on the Flores SST Case Scenario

On the other hand, for the Flores SST case, the obtained results for a LFM pulse with a carrier frequency of 16.7 GHz, with a bandwidth of 610 kHz, show less efficiency in detecting targets for lower SNR. As it is possible to see in figure 4.20, for the same value of $SNR = -20$dB and a threshold of 0.7, we will only have a TPR of 67%. This fact it is related to the fact that this radar has a narrowest bandwidth, which is a very important factor in signal correlation.

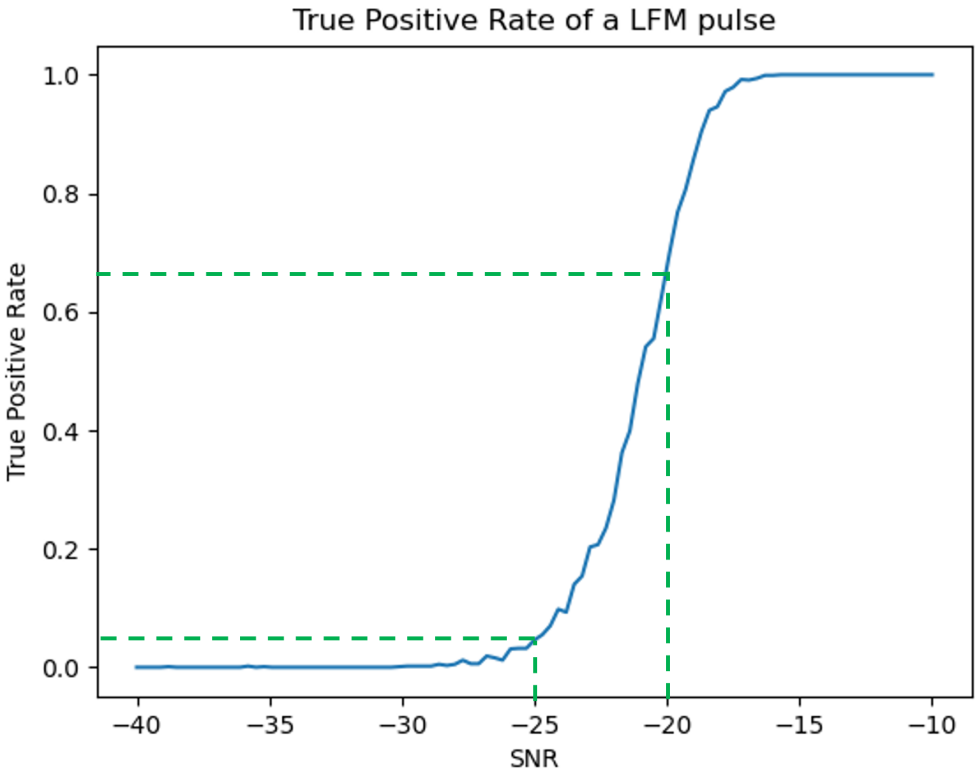

FIGURE 4.20: True Positive Rate for the Flores SST case scenario.

LFM on a Highly Attenuating Atmosphere Case Scenario

As would be expected, although there is a very strong attenuation during the propagation of the signal through the atmosphere to $f_c = 22$GHz, considering that during the determination of these curves we are forcing the SNR values, the TPR will only be dependent on the bandwidth used in the simulation. Since the transmitted signal was simulated for a bandwidth of 80MHz, as in the case of ATLAS, the curves are very similar, as it is possible to see in figure 4.21.

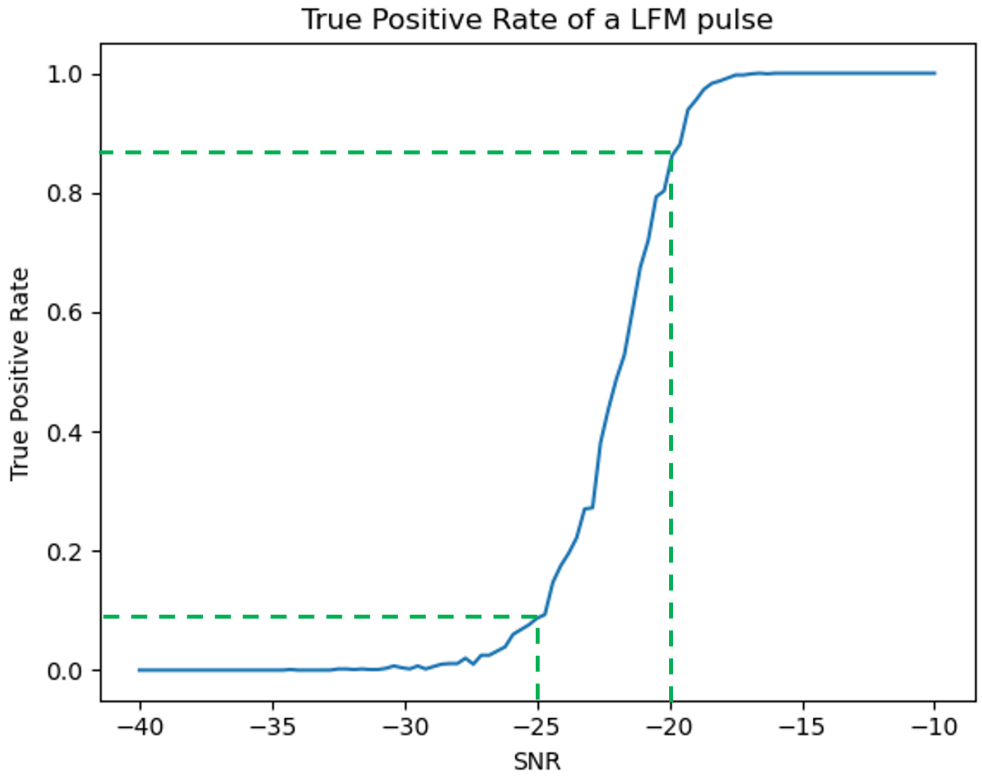

FIGURE 4.21: True Positive Rate for a highly attenuating atmosphere case scenario.

LFM Train Case Scenario

To calculate the TPR of an LFM train of 5 pulses with a carrier frequency of 5.56 GHz and a bandwidth of 80 MHz, and considering the zero-Doppler cut obtained with a higher SNR as shown in figure 4.12, a threshold of 0.7 was established and the bed of nails peaks were ignored, otherwise there would always be other peaks exceeding the threshold value, what would lead to wrong values of TPR.

As it is possible to see in figure 4.22, we have obtained slightly better results when comparing to a transmission of a single pulse (figure 4.19), as it would be expected.

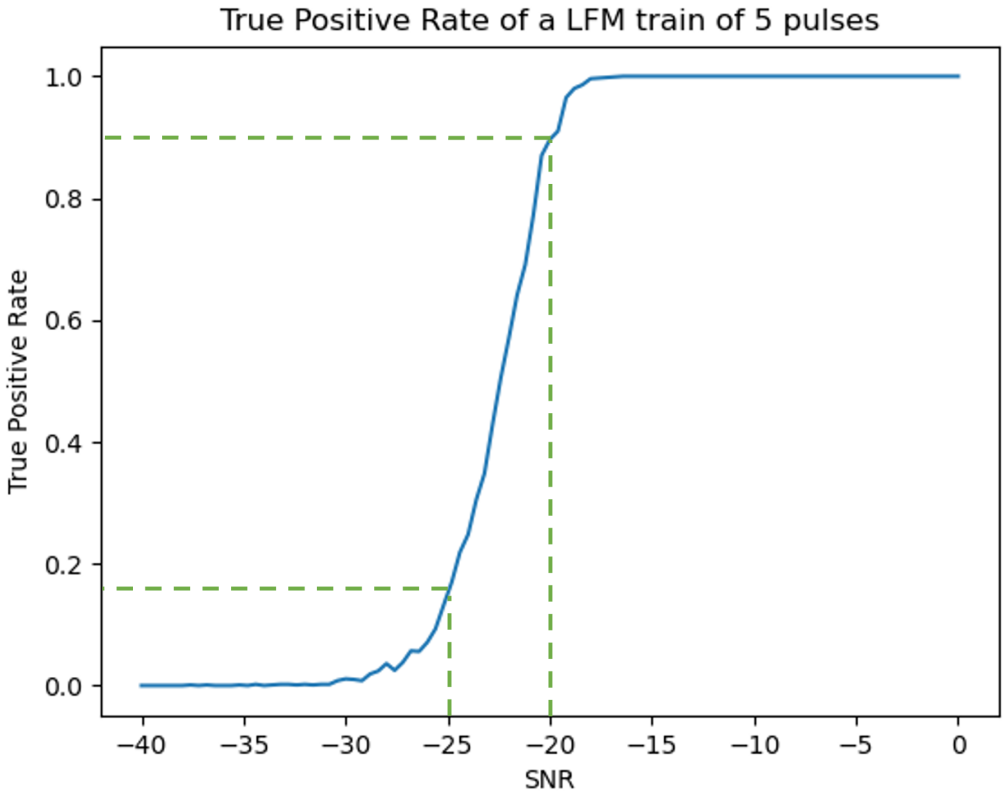

FIGURE 4.22: True Positive Rate for a LFM train of 5 pulses.

Stepped FM Case Scenario

For a Stepped FM signal with 5 pulses with a carrier frequency of 5.56 GHz and a bandwidth of 80 MHz, considering the zero-Doppler cut obtained with a higher SNR as shown in figure 4.14 that shows so many secondary peaks, in order to calculate the TPR it was established that we would have a detection if the higher peak would continue to be for time delay $\tau = 0$, which resulted on the TPR shown in figure 4.23, that also presents reasonable results for low SNR values.

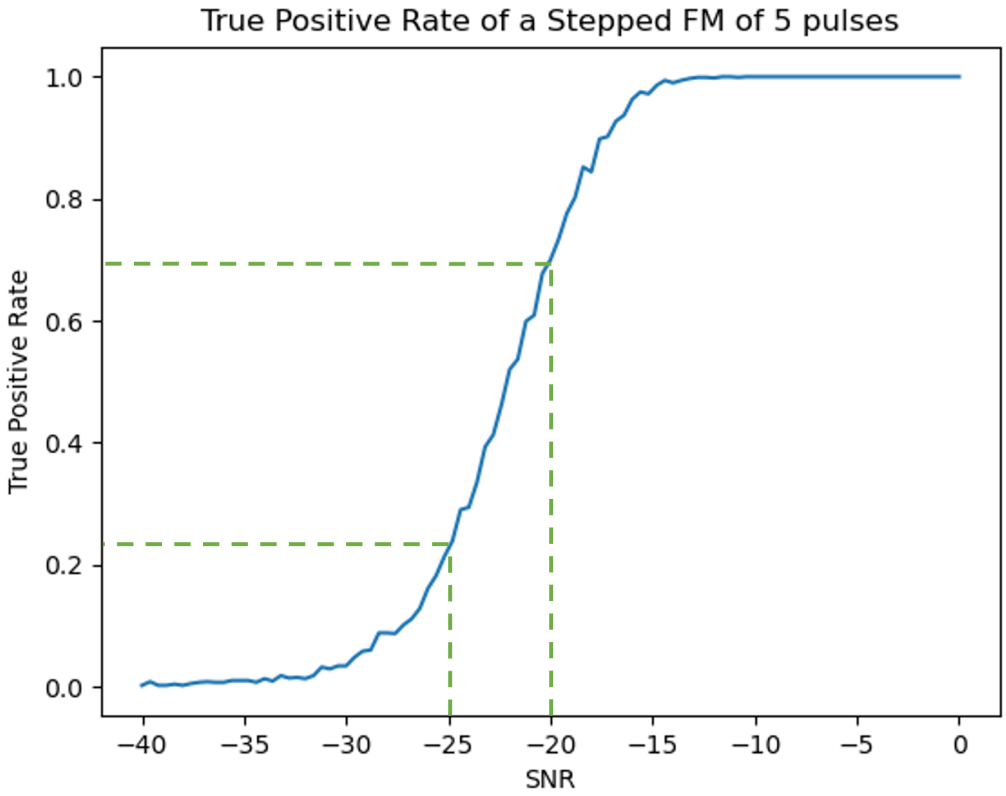

FIGURE 4.23: True Positive Rate for a Stepped FM of 5 pulses.

Barker Codes Case Scenario

The applied approach in order to calculate the TPR for a Barker code pulse, considering the zero-Doppler cut obtained with a higher SNR as shown in figure 4.16, was similar to the one applied for the Stepped FM signal. A detection would occur if the higher peak would continue to be for time delay $\tau = 0$, which resulted on the TPR shown in figure 4.24 for a Barker5 pulse and in figure 4.25 for a Barker13 pulse, showing that a Barker13 would have better results than a Barker5 as expected, nevertheless both presenting acceptable results for low SNR values.

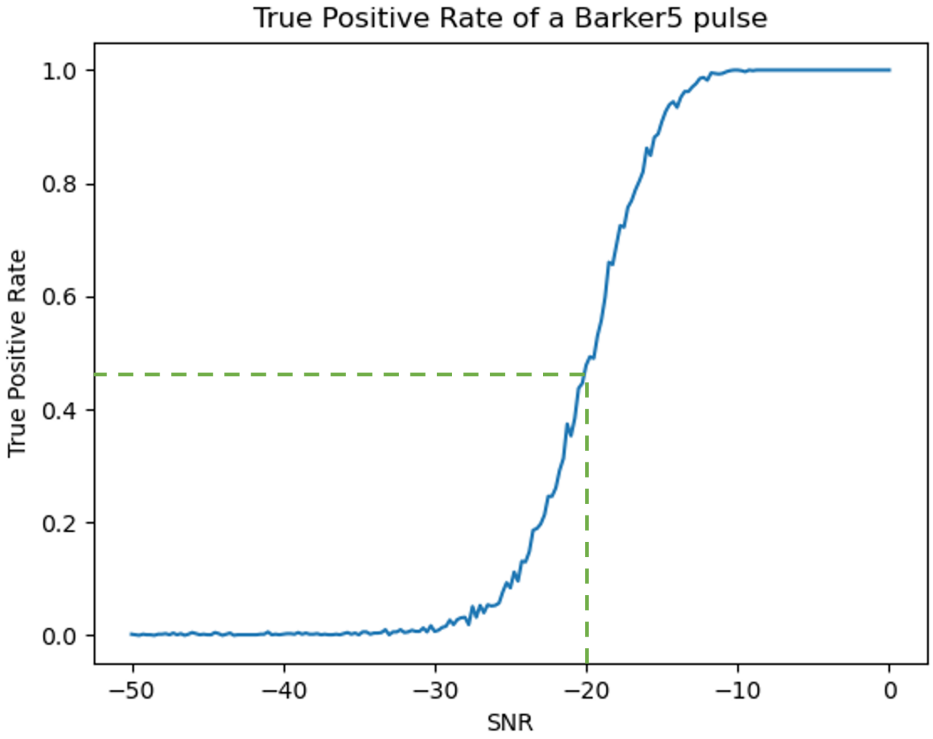

FIGURE 4.24: True Positive Rate for a Barker5 pulse.

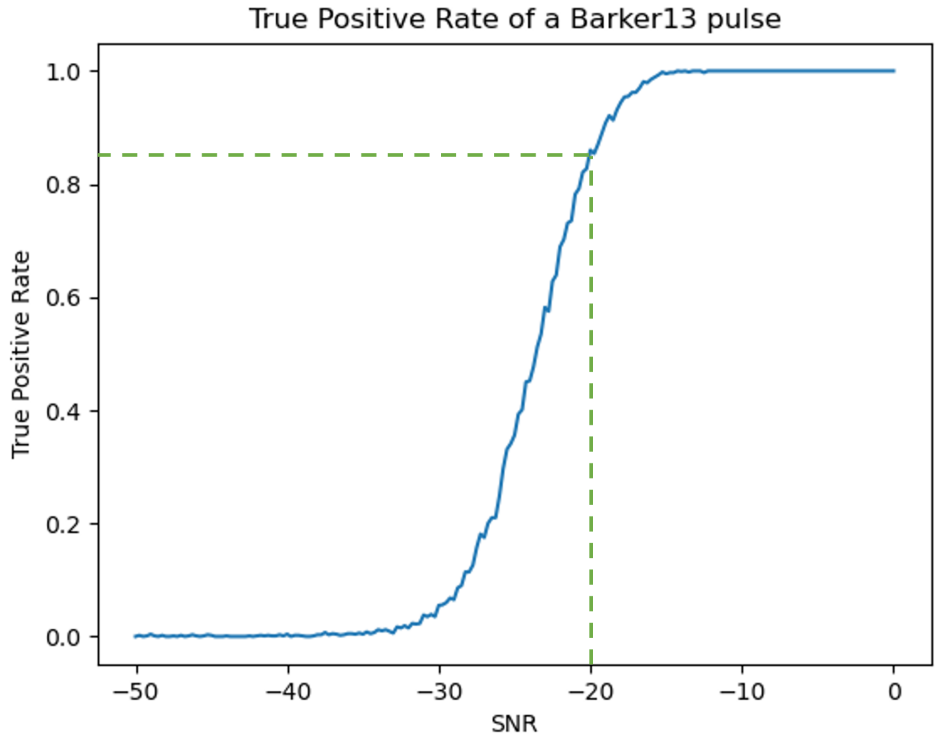

FIGURE 4.25: True Positive Rate for a Barker13 pulse.

Unmodulated Pulse Case Scenario

Lastly, for a unmodulated pulse with a carrier frequency of 5.56 GHz, and considering its zero-Doppler cut with a triangular shape, it was also established that a detection would occur if the higher peak would continue to be for time delay $\tau = 0$, which resulted on the TPR shown in figure 4.26.

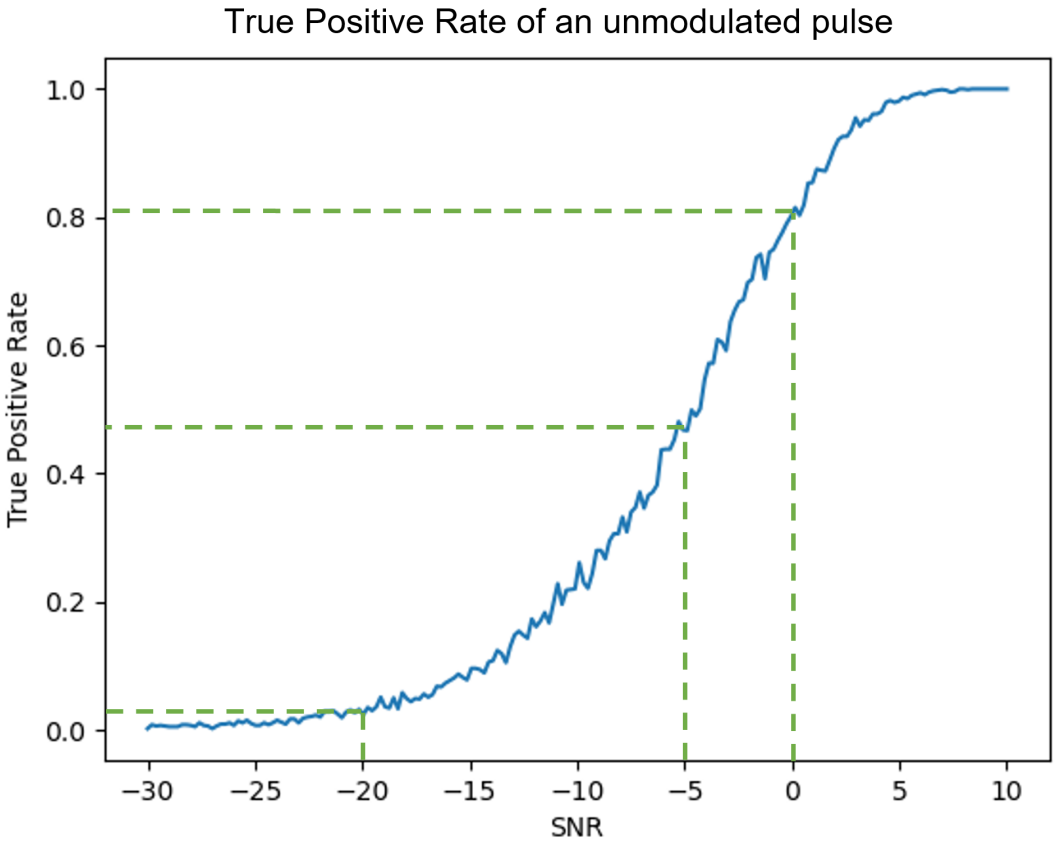

FIGURE 4.26: True Positive Rate for an Unmodulated pulse.

These results clearly show the low detection capabilities that an unmodulated pulse offer to a radar system, which only starts to present acceptable TPR when the energy power of the signal equals the energy power of noise (SNR = 0), and when comparing to a $SNR = -20$dB, that has been denoted in all of the previous TPR graphics, it is possible to see that for an unmodulated pulse, it has a TPR of 4% alternatively to the 47% presented for the Barker5, which was the lowest TPR value for a $SNR = -20$dB as described in table 4.2, proving once again the low efficiency of this signal.

TPR Results		
Pulse Compression Technique	SNR	True Positive Rate
LFM on ATLAS	-20 dB	87%
LFM on Flores SST	-20 dB	67%
LFM Train	-20 dB	91%
Stepped FM	-20 dB	71%
Barker5	-20 dB	47%
Barker13	-20 dB	85%
Unmodulated	-20 dB	4%

TABLE 4.2: TPR results.

Chapter 5

Conclusion

With the projection and consequent development of ATLAS, integrated on the expansion plan of the EUSST sensor network for detection and tracking of space debris, it was considered of high importance the creation of a simulator that would be able to determine with precision what we will predictably obtain from a detection of a target in LEO.

Following ITU-R recommendations, the Earth-space propagation simulator was created, being now necessary to conclude whether its operation and information that it is able to provide are correct and useful for ATLAS.

Considering all the simulator's features and presented results, we can affirm that it is a tool that can achieve a very good performance in predicting all effects that affect a radar signal during its propagation in the atmosphere. We were able to verify that for the ATLAS transmission frequency, it will not be the attenuation imposed by atmospheric gases during signal propagation that will affect the target detection effectiveness, but rather the distance and dimension of that target.

Focusing now on the tests from chapter 4.1, and considering that LEO heights go from 160km to 1000km [34], it is possible to verify that using the ATLAS we should be able to detect small targets in all LEO height range. As shown in figure 4.7, for a target with a RCS of 1 m^2, which was in a relative elevation of 90° to the antenna site and at 900 km of altitude it was possible to get a reasonable detection of the target, but if the antenna was not pointing to the zenith, we would get SNR values much smaller. For example, for the same propagation conditions, if we simply changed the relative elevation of 90° to 30°, we would get a SNR value of -38.62 dB instead of -26.25 dB, which would disable the ATLAS capability of detect a target for those conditions. Therefore, with the use of the Earth-space propagation simulator, we can accurately predict for which conditions we would achieve a good target detection.

Another characteristic that we consider to be very important to highlight is the fact that the Earth-space propagation simulator is able to demonstrate that for different atmospheres, where the vertical profiles of temperature, water vapor density and atmospheric pressure change, the radar signal will be attenuated differently, consequently changing the SNR with which we will receive it.

In addiction, with the results obtained in chapter 4.2, it is evident the achieved improvement on the target detection performance when the radar uses pulse compression techniques, with which we can obtain very good results even in the presence of very low SNR values (around -20 dB), contrarily to what would happen if the radar transmitted unmodulated pulses, where it would only be possible to achieve such good detecting results for positive SNR values.

5.1 Future Work

In terms of the work that may be developed in the future, it would be interesting to add other initial conditions, including natural phenomena that occasionally occur, such as rain, fog, snow, or even sporadic events at an ionospheric level, expressed into the occurrence of scintillations. Another type of initial conditions that could be added, outside the atmosphere domain, is the presence of buildings in the surroundings of the location where the radar site is located. Thus, the simulator would offer even more features in terms of the veracity of its simulation, so it would be much more adaptable to different environmental and geographic conditions.

As previously mentioned in 3.4.3, there is also the limitation of the TEC calculation, which led to the fixed setting of the geographic location data of the radar site, so that the simulation was as correct as possible for the ATLAS study case. In order to have the possibility of changing the location of the radar site, it would be necessary to adapt or implement new source code so that the NeQuick2 model was fully operational, allowing the calculation of the TEC for any scenario.

Finally, it would also be important to add other features to the target in order to produce a simulator even more capable of achieve a real detection scenario, namely the target's speed as well as its rotation.

Bibliography

[1] Tereza Pultarova. *Europe plans to launch space telescope to monitor orbital debris*. 2021. URL: https://www.space.com/orbiting-space-debris-telescope-esa (visited on 04/04/2021).

[2] UNOOSA. "Space Debris Mitigation Guidelines of the Committee on the Peaceful Uses of Outer Space". In: *United Nations* (2010), pp. 1–6. ISSN: 02784017. arXiv: SalesNo.E.99.I.17. URL: http://www.unoosa.org/pdf/publications/st%7B%5C_%7Dspace%7B%5C_%7D49E.pdf.

[3] Becky Ianotta. *U.S. Satellite Destroyed in Space Collision*. 2009. URL: https://www.space.com/5542-satellite-destroyed-space-collision.html (visited on 03/10/2021).

[4] Michael Cooney. *NASA identifies Top Ten Space Junk Missions*. 2010. URL: https://www.networkworld.com/article/2231453/nasa-identifies-top-ten-space-junk-missions.html (visited on 03/10/2021).

[5] Joseph N Pelton. *New Solutions for the Space Debris Problem*. Springer, 2015, pp. 1–102. ISBN: 9783319171500.

[6] *EUSST*. URL: https://www.eusst.eu/ (visited on 03/10/2021).

[7] Inigo del Portillo. *ITU-Rpy*. 2021. URL: https://github.com/inigodelportillo/ITU-Rpy (visited on 05/10/2021).

[8] Constantine A. Balanis. *Antenna Theory: Analysis and Design*. fourth. Wiley, 2016, pp. 1–1073.

[9] Matteo Losacco and Luca Schirru. "Orbit determination of resident space objects using the P-band mono-beam receiver of the Sardinia Radio Telescope". In: *Applied Sciences* 9 (2019), pp. 1–14. ISSN: 20763417. DOI: 10.3390/app9194092.

[10] Giacomo Muntoni et al. "Space Debris Detection in Low Earth Orbit with the Sardinia Radio Telescope". In: *Electronics* 6.3 (2017), pp. 1–15. ISSN: 20799292. DOI: 10.3390/electronics6030059.

[11] Carsten Schult et al. "Dual frequency measurements of meteor head echoes simultaneously detected with the MAARSY and EISCAT radar systems". In: *Icarus* 355.October 2020 (2021). ISSN: 10902643. DOI: 10.1016/j.icarus.2020.114137. URL: https://doi.org/10.1016/j.icarus.2020.114137.

[12] H. Wilden et al. "GESTRA-A phased-array based surveillance and tracking radar for space situational awareness". In: *IEEE International Symposium on Phased Array Systems and Technology* 0 (2016), pp. 2–6. DOI: 10.1109/ARRAY.2016.7832621.

[13] Nadav Levanon and Eli Mozeson. *Radar Signals*. Wiley, 2004, pp. 1–427. ISBN: 9786468600.

[14] Sneha H.L. *Basic Signal Operations in DSP: Time Shifting, Time Scaling, and Time Reversal*. 2017. URL: https://www.allaboutcircuits.com/technical-articles/basic-signal-operations-in-dsp-time-shifting-time-scaling-and-time-reversal/ (visited on 08/06/2021).

[15] João Pandeirada et al. "Development of the First Portuguese Radar Tracking Sensor for Space Debris". In: *Signals* (2021), pp. 1–16. ISSN: 00319228. DOI: 10.1063/1.2800252.

[16] Robert E. Collin. *Antennas and Radiowave Propagation*. McGraw-Hill Book Company, 1985, pp. 1–508.

[17] K.G. Budden. *The Propagation of Radio Waves: The theory of radio waves of low power in the ionosphere and magnetosphere*. Melbourne: Cambridge University Press, 1986, pp. 1–1448. DOI: 10.1126/science.232.4756.1448.

[18] International Telecommunication Union. "P.525-4: Calculation of free-space attenuation". In: 4 (Aug. 2019), pp. 1–6.

[19] Pedro Miguel da Silva Gaspar. "Modelos de Propagação Terra-Satélite na Banda Ka". PhD thesis. Universidade de Aveiro, 2008, p. 135.

[20] International Telecommunication Union. "P.676-12: Attenuation by atmospheric gases and related effects". In: (2019), pp. 1–32.

[21] Norman E. Gaut. *Studies of Atmospheric Water Vapor by Means of Passive Microwave Techniques*. Tech. rep. Massachusetts, 1968, pp. 1–118.

[22] International Telecommunication Union. "P.531-14: Ionospheric propagation data and prediction methods required for the design of satellite networks and systems". In: 10 (2019), pp. 1–25. URL: http://www.itu.int/ITU-R/.

[23] Flávio Jorge and Armando Rocha. "Modelos de Propagação Terra - Satélite e Separação das Contribuições para a Despolarização". In: *7.º Congresso do Comité Português da URSI – "Um mar sem fronteiras: desafios tecnológicos"* (2013), pp. 1–7.

[24] International Telecommunication Union. "P.834-9: Effects of tropospheric refraction on radiowave propagation". In: (2017), pp. 1–17. URL: https://www.itu.int/rec/R-REC-P.834/en.

[25] International Telecommunication Union. "P.619-4: Propagation data required for the evaluation of interference between stations in space and those on the surface of the Earth". In: 4 (2019), pp. 1–5.

[26] International Telecommunication Union. "P.453-14: The radio refractive index : its formula and refractivity data". In: 10 (2019), pp. 1–24.

[27] José Mendes. *Earth-Space Propagation Simulator*. 2021. URL: https://github.com/jofrmendes/propagationsimulator (visited on 08/31/2021).

[28] João Pandeirada. *Ambpy*. 2021. URL: https://github.com/j-pandeirada/ambpy (visited on 02/05/2021).

[29] International Telecommunication Union. "P.835-6: Reference standard atmospheres". In: 6 (2017), pp. 1–12.

[30] *NeQuick2 - Web Model*. URL: https://t-ict4d.ictp.it/nequick2/nequick-2-web-model (visited on 03/05/2021).

[31] Merrill I. Skolnik. *Radar handbook*. Third. The McGraw-Hill Companies, 2008, pp. 1–1352.

[32] Jason Earl Baptista Adams. "Análise e Simulação de um Radar Terrestre para Deteção de Detrito Espacial". PhD thesis. Universidade de Aveiro, 2018, pp. 1–46.

[33] Aniruddha Bhandari. *AUC-ROC Curve in Machine Learning Clearly Explained*. 2020. URL: https://www.analyticsvidhya.com/blog/2020/06/auc-roc-curve-machine-learning/ (visited on 08/02/2021).

[34] L. Boldt-Christmas. *Low Earth orbit*. URL: https://www.esa.int/ESA%7B%5C_%7DMultimedia/Images/2020/03/Low%7B%5C_%7DEarth%7B%5C_%7Dorbit (visited on 08/21/2021).

Appendix A - ATLAS tests

Chirp Nº	File	Freq. Carrier	BW	PRF	Duty Cycle	Azimuth	Elevation	Height	Season	Hour	RCS	SNR
Chirp1	0001	5.56GHz	20MHz	6103	100	210	90	900	Summer(1)	12	1	-26.25 dB
Chirp2	0002	5.56GHz	20MHz	6103	100	210	90	300	Summer(1)	12	1	-7.16 dB
Chirp3	0003	5.56GHz	20MHz	6103	100	210	90	900	Summer(1)	12	10	-16.25 dB
Chirp4	0004	5.56GHz	20MHz	6103	100	60	90	900	Winter(2)	6	1	-26.24 dB
Chirp5	0005	5.56GHz	20MHz	6103	100	60	90	300	Winter(2)	6	1	-7.16 dB
Chirp6	0006	5.56GHz	20MHz	6103	100	60	90	900	Winter(2)	6	10	-16.24 dB
Chirp7	0007	16.7GHz	0.61MHz	6103	100	210	90	900	Summer(1)	12	1	25.07 dB
Chirp8	0008	16.7GHz	0.61MHz	6103	100	210	90	300	Summer(1)	12	1	44.16 dB
Chirp9	0009	16.7GHz	0.61MHz	6103	100	210	90	900	Summer(1)	12	10	35.07 dB
Chirp10	0010	16.7GHz	0.61MHz	6103	100	60	90	900	Winter(2)	6	1	25.64 dB
Chirp11	0011	16.7GHz	0.61MHz	6103	100	60	90	300	Winter(2)	6	1	44.73 dB
Chirp12	0012	16.7GHz	0.61MHz	6103	100	60	90	900	Winter(2)	6	10	35.64 dB
Chirp13	0013	22GHz	20MHz	6103	100	210	90	900	Summer(1)	12	1	-45.09 dB
Chirp14	0014	22GHz	20MHz	6103	100	210	90	300	Summer(1)	12	1	-26.01 dB
Chirp15	0015	22GHz	20MHz	6103	100	210	90	900	Summer(1)	12	10	-35.09 dB
Chirp16	0016	22GHz	20MHz	6103	100	60	90	900	Winter(2)	6	1	-40.41 dB
Chirp17	0017	22GHz	20MHz	6103	100	60	90	300	Winter(2)	6	1	-21.33 dB
Chirp18	0018	22GHz	20MHz	6103	100	60	90	900	Winter(2)	6	10	-30.41 dB
LFMTrain1	0019	5.56GHz	20MHz	18310	80	210	90	900	Summer(1)	12	1	-21.48 dB
LFMTrain2	0020	5.56GHz	20MHz	18310	80	210	90	300	Summer(1)	12	1	-2.39 dB
LFMTrain3	0021	5.56GHz	20MHz	18310	80	210	90	900	Summer(1)	12	10	-11.48dB
LFMTrain4	0022	5.56GHz	20MHz	18310	80	60	90	900	Winter(2)	6	1	-21.47 dB
LFMTrain5	0023	5.56GHz	20MHz	18310	80	60	90	300	Winter(2)	6	1	-2.39 dB
LFMTrain6	0024	5.56GHz	20MHz	18310	80	60	90	900	Winter(2)	6	10	-11.47 dB
SteppedFM1	0025	5.56GHz	20MHz	18310	80	210	90	900	Summer(1)	12	1	-21.48 dB
SteppedFM2	0026	5.56GHz	20MHz	18310	80	210	90	300	Summer(1)	12	1	-2.39 dB
SteppedFM3	0027	5.56GHz	20MHz	18310	80	210	90	900	Summer(1)	12	10	-11.48 dB
SteppedFM4	0028	5.56GHz	20MHz	18310	80	60	90	900	Winter(2)	6	1	-21.47 dB
SteppedFM5	0029	5.56GHz	20MHz	18310	80	60	90	300	Winter(2)	6	1	-2.39 dB
SteppedFM6	0030	5.56GHz	20MHz	18310	80	60	90	900	Winter(2)	6	10	-11.47 dB
Barker5(1)	0031	5.56GHz	-	6103	100	210	90	900	Summer(1)	12	1	-33.24 dB
Barker5(2)	0032	5.56GHz	-	6103	100	210	90	300	Summer(1)	12	1	-14.15 dB
Barker5(3)	0033	5.56GHz	-	6103	100	210	90	900	Summer(1)	12	10	-23.24 dB
Barker5(4)	0034	5.56GHz	-	6103	100	60	90	900	Winter(2)	6	1	-33.23 dB
Barker5(5)	0035	5.56GHz	-	6103	100	60	90	300	Winter(2)	6	1	-14.15 dB
Barker5(6)	0036	5.56GHz	-	6103	100	60	90	900	Winter(2)	6	10	-23.23 dB
Barker13(1)	0037	5.56GHz	-	6103	100	210	90	900	Summer(1)	12	1	-33.24 dB
Barker13(2)	0038	5.56GHz	-	6103	100	210	90	300	Summer(1)	12	1	-14.15 dB
Barker13(3)	0039	5.56GHz	-	6103	100	210	90	900	Summer(1)	12	10	-23.24 dB
Barker13(4)	0040	5.56GHz	-	6103	100	60	90	900	Winter(2)	6	1	-33.23 dB
Barker13(5)	0041	5.56GHz	-	6103	100	60	90	300	Winter(2)	6	1	-14.15 dB
Barker13(6)	0042	5.56GHz	-	6103	100	60	90	900	Winter(2)	6	10	-23.23 dB

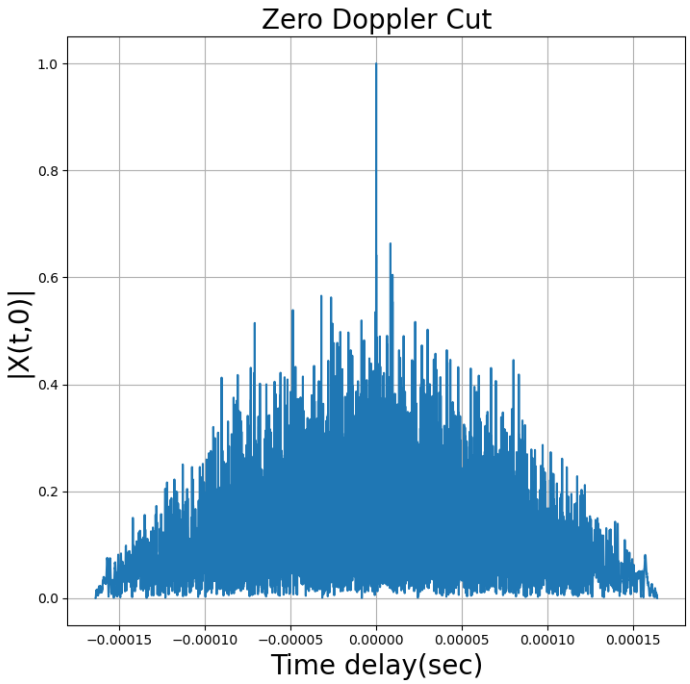

FIGURE A.1: Zero-Doppler cut of a LFM signal for the ATLAS case scenario with SNR = -26.25 dB.

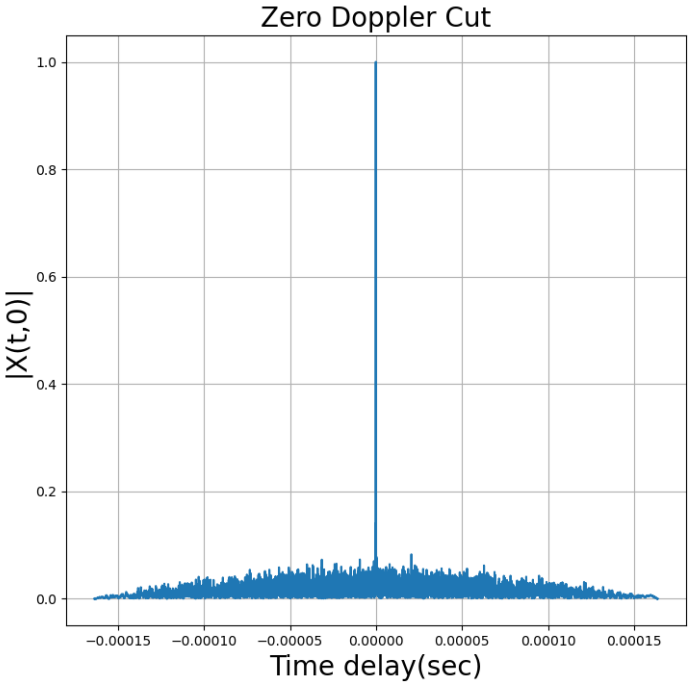

FIGURE A.2: Zero-Doppler cut of a LFM signal for the ATLAS case scenario with SNR = -7.16 dB.

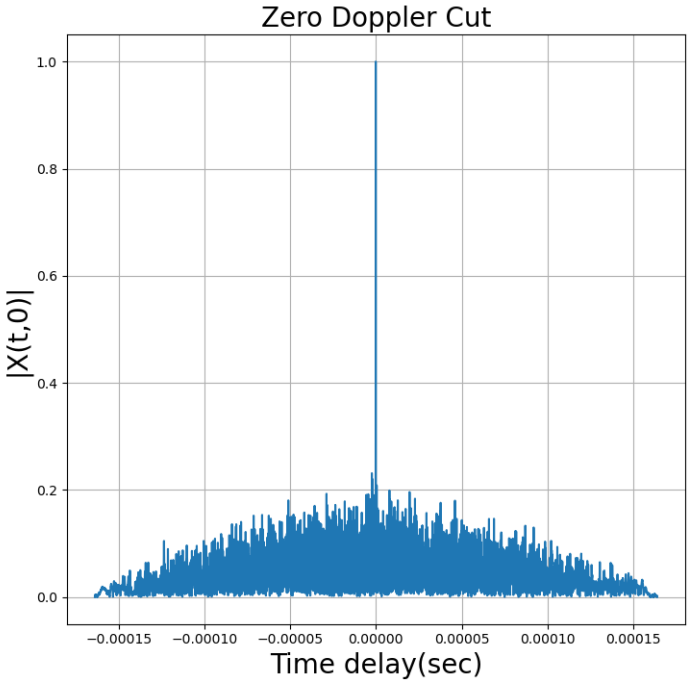

FIGURE A.3: Zero-Doppler cut of a LFM signal for the ATLAS case scenario with SNR = -16.25 dB.

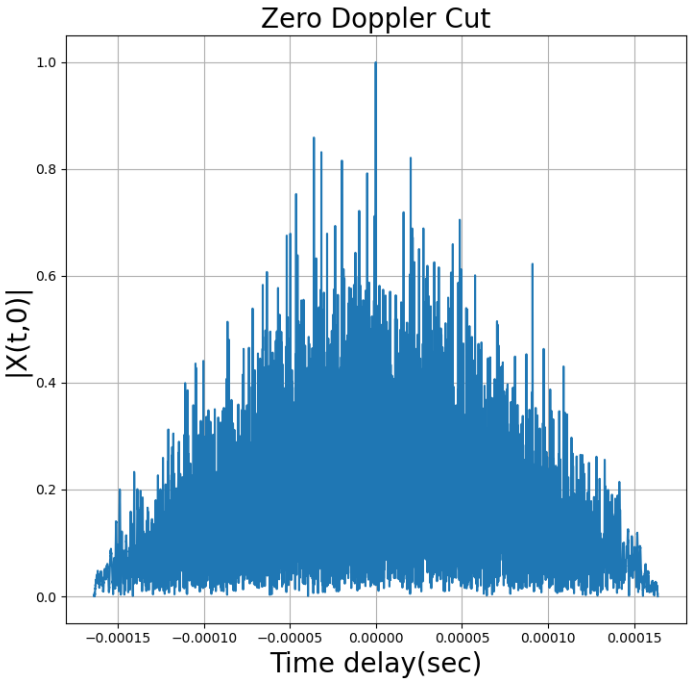

FIGURE A.4: Zero-Doppler cut of a LFM signal for the ATLAS case scenario with SNR = -26.24 dB.

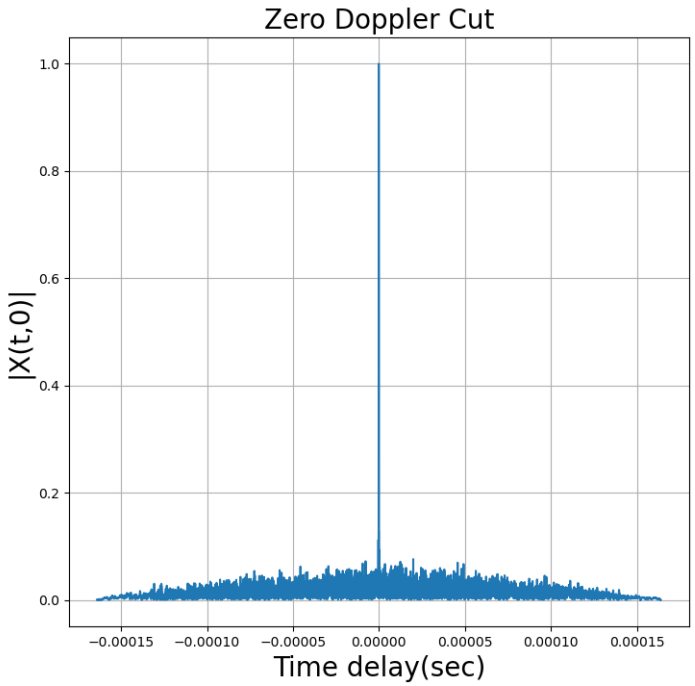

FIGURE A.5: Zero-Doppler cut of a LFM signal for the ATLAS case scenario with SNR = -7.16 dB.

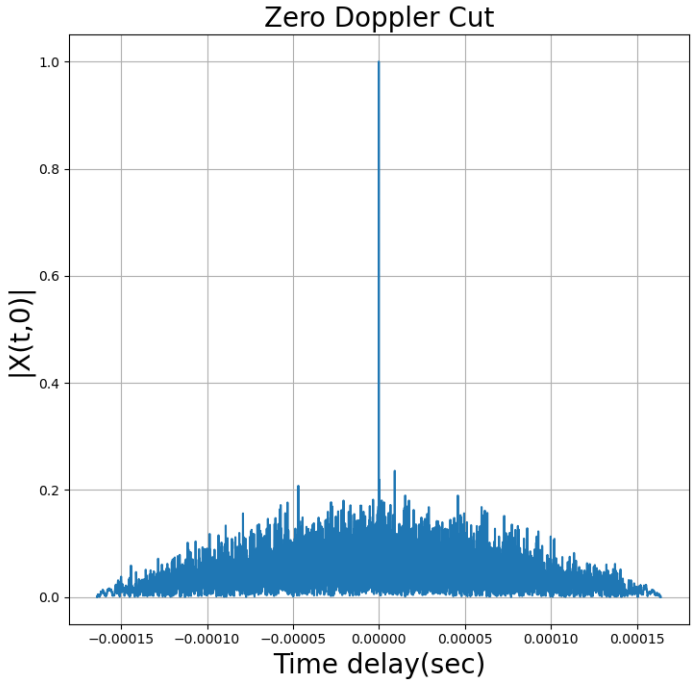

FIGURE A.6: Zero-Doppler cut of a LFM signal for the ATLAS case scenario with SNR = -16.24 dB.

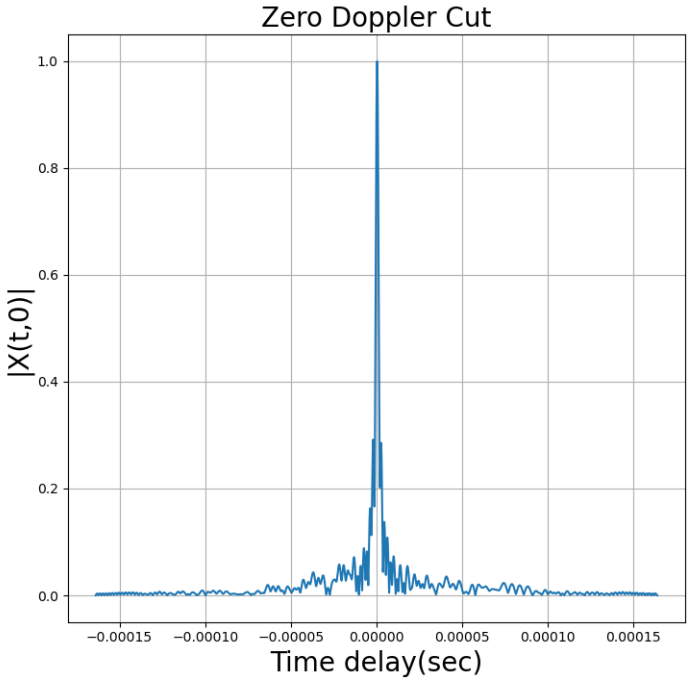

FIGURE A.7: Zero-Doppler cut of a LFM signal for the Flores SST case scenario with SNR = 25.07 dB.

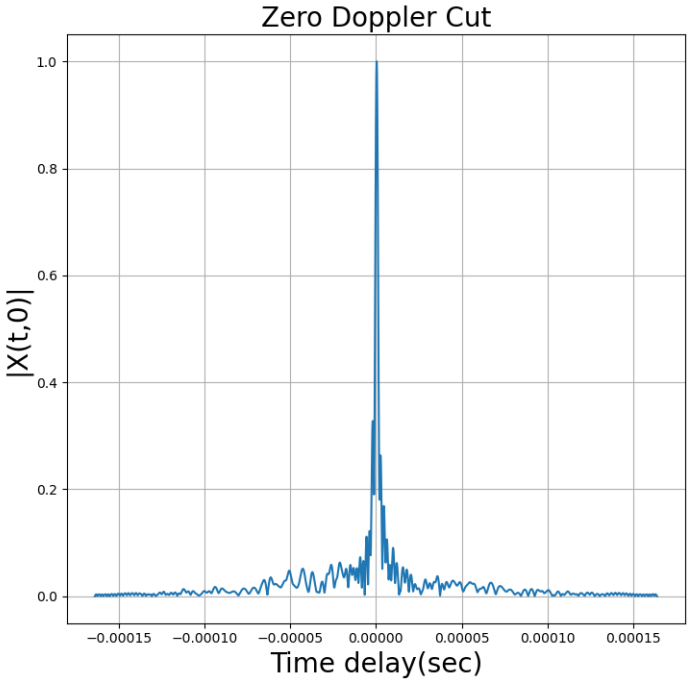

FIGURE A.8: Zero-Doppler cut of a LFM signal for the Flores SST case scenario with SNR = 44.16 dB.

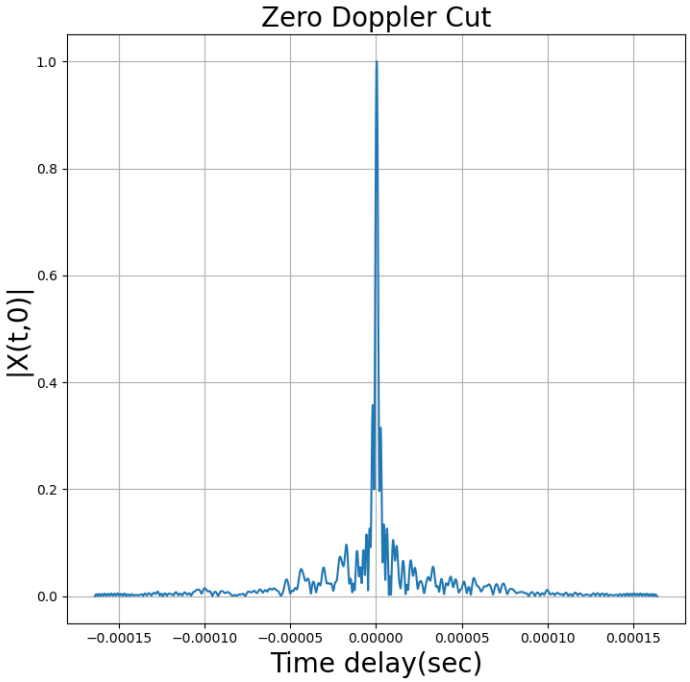

FIGURE A.9: Zero-Doppler cut of a LFM signal for the Flores SST case scenario with SNR = 35.07 dB.

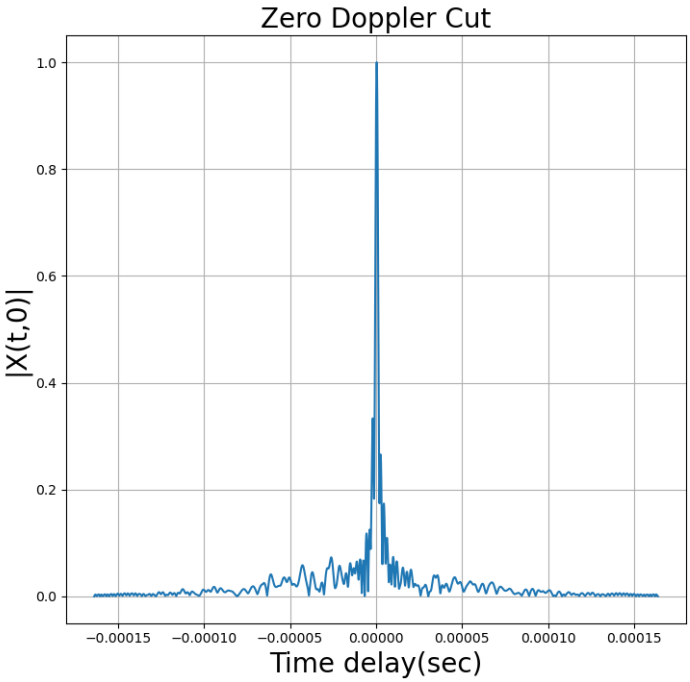

FIGURE A.10: Zero-Doppler cut of a LFM signal for the Flores SST case scenario with SNR = 25.64 dB.

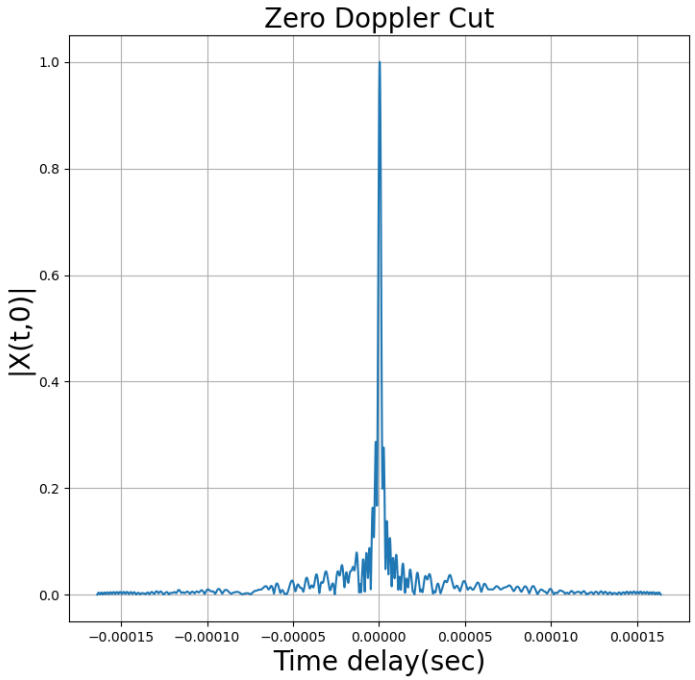

FIGURE A.11: Zero-Doppler cut of a LFM signal for the Flores SST case scenario with SNR = 44.73 dB.

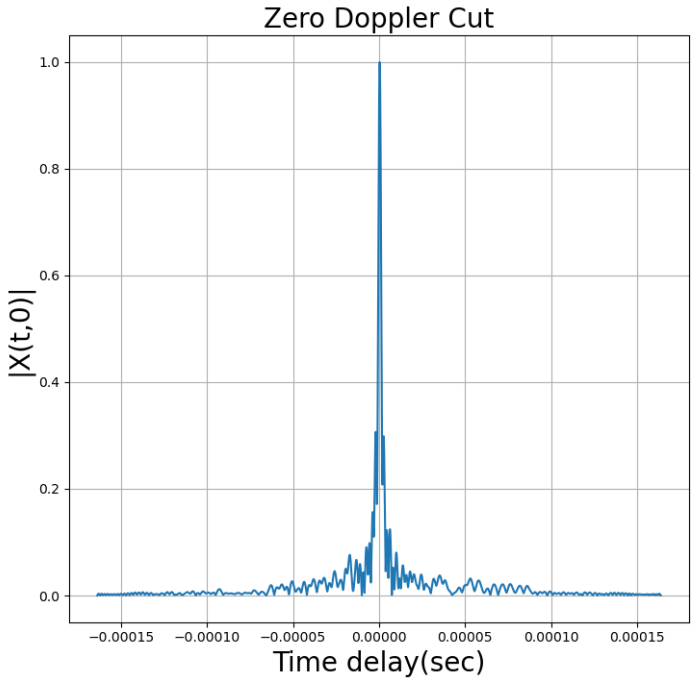

FIGURE A.12: Zero-Doppler cut of a LFM signal for the Flores SST case scenario with SNR = 35.64 dB.

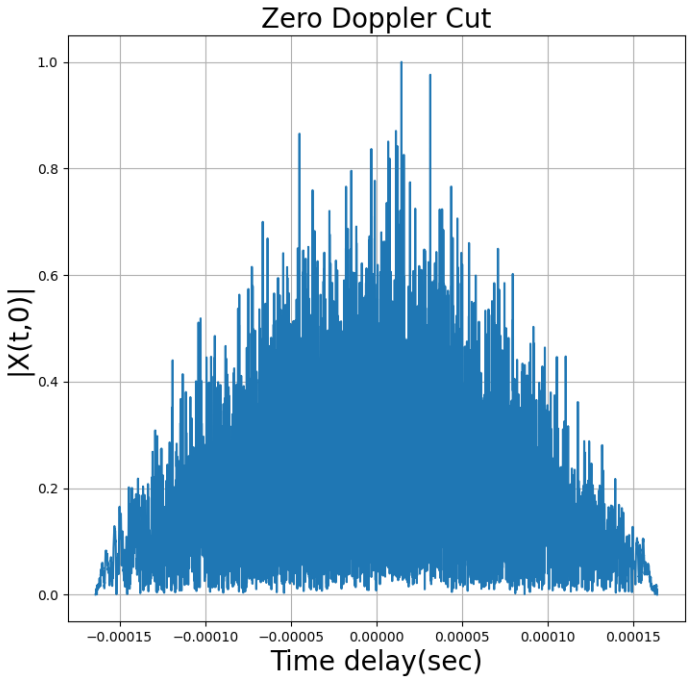

FIGURE A.13: Zero-Doppler cut of a LFM signal for a highly attenuating atmosphere case scenario with SNR = -45.09 dB.

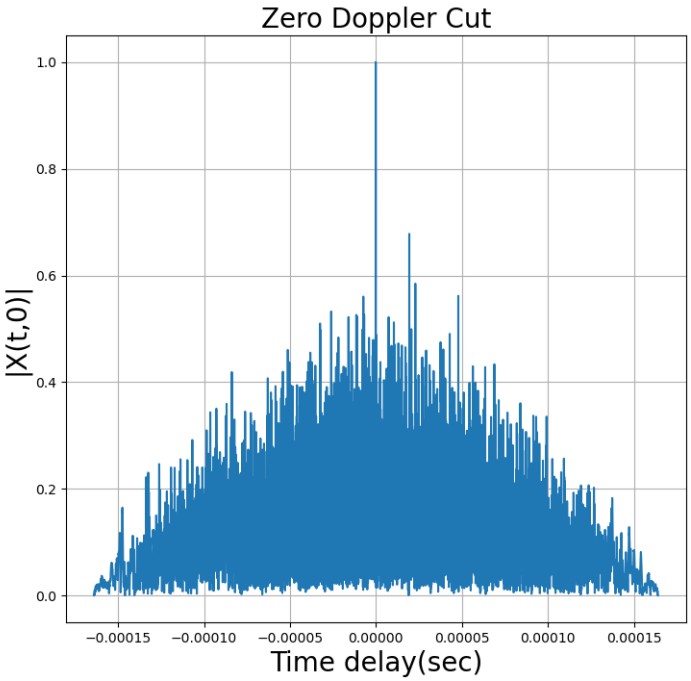

FIGURE A.14: Zero-Doppler cut of a LFM signal for the ATLAS case scenario with SNR = -26.01 dB.

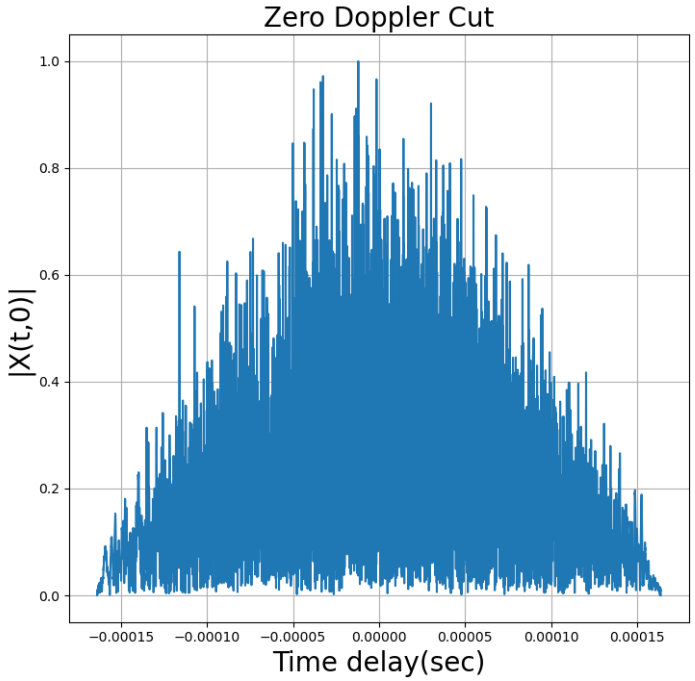

FIGURE A.15: Zero-Doppler cut of a LFM signal for the ATLAS case scenario with SNR = -35.09 dB.

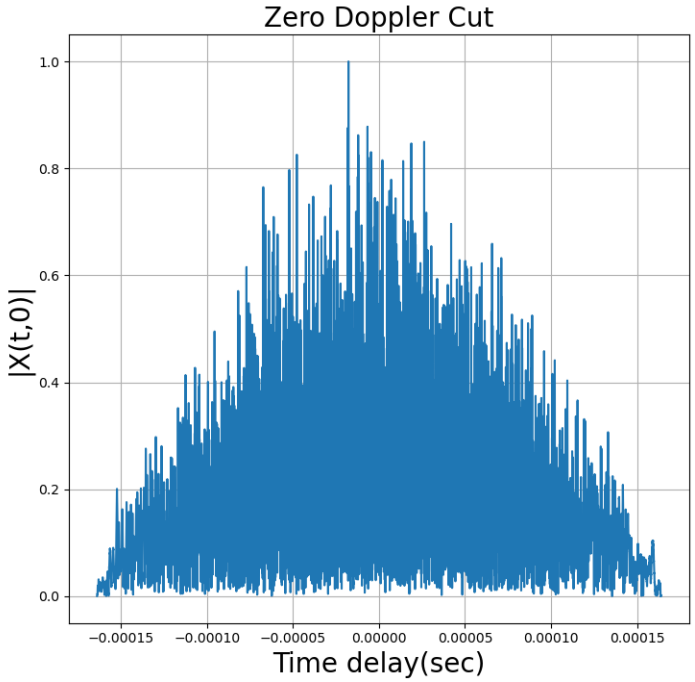

FIGURE A.16: Zero-Doppler cut of a LFM signal for the ATLAS case scenario with SNR = -40.41 dB.

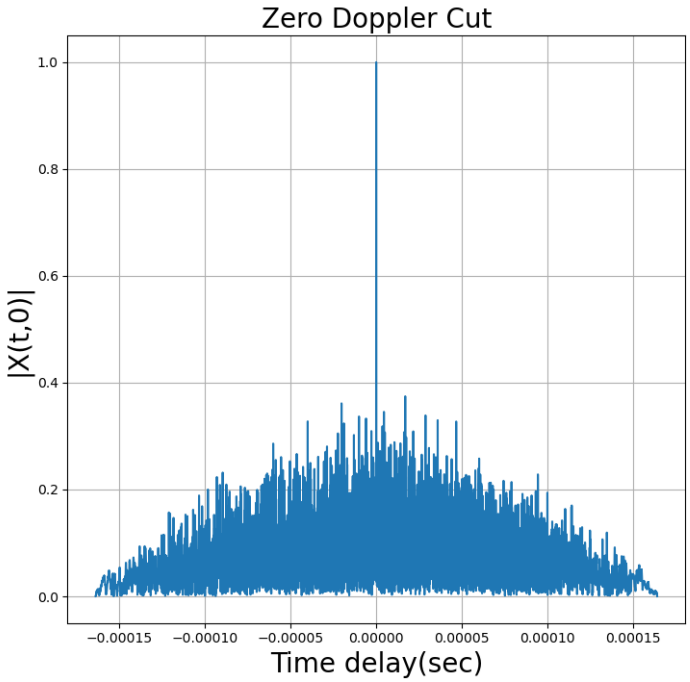

FIGURE A.17: Zero-Doppler cut of a LFM signal for the ATLAS case scenario with SNR = -21.33 dB.

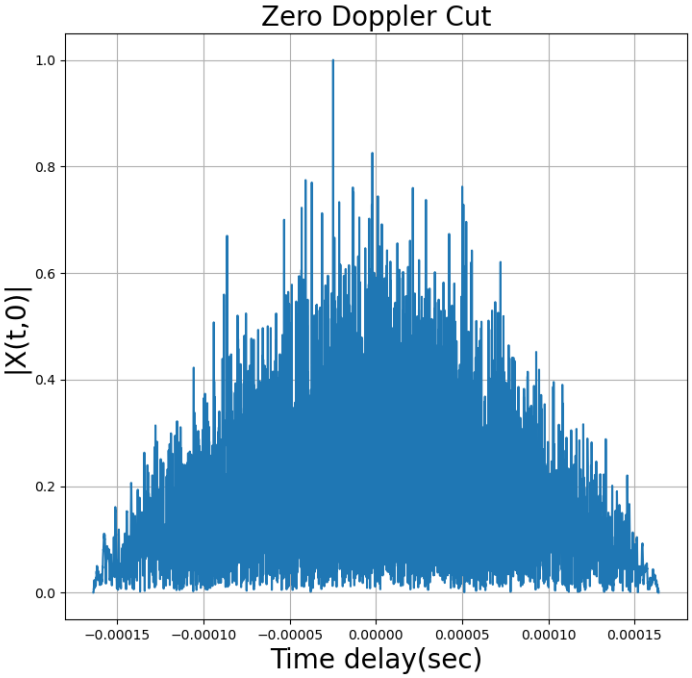

FIGURE A.18: Zero-Doppler cut of a LFM signal for the ATLAS case scenario with SNR = -30.41 dB.

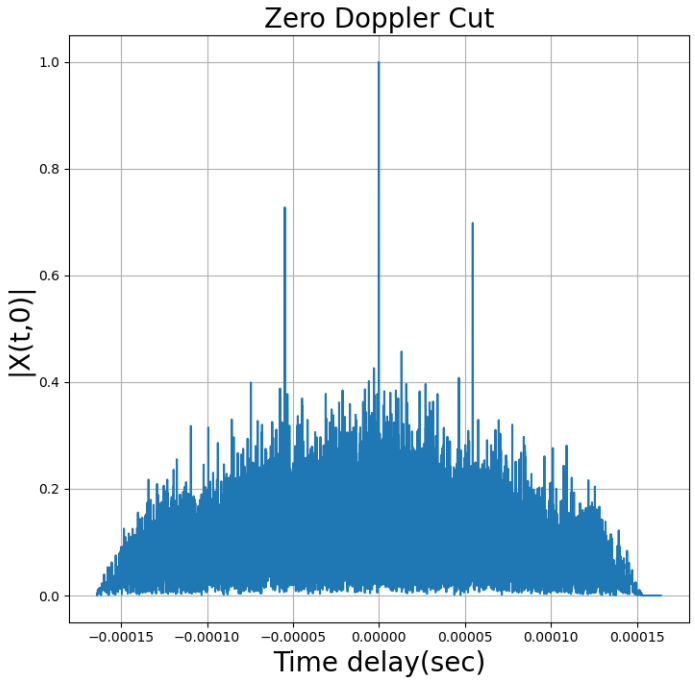

FIGURE A.19: Zero-Doppler cut of a LFM Train signal with SNR = -21.48 dB.

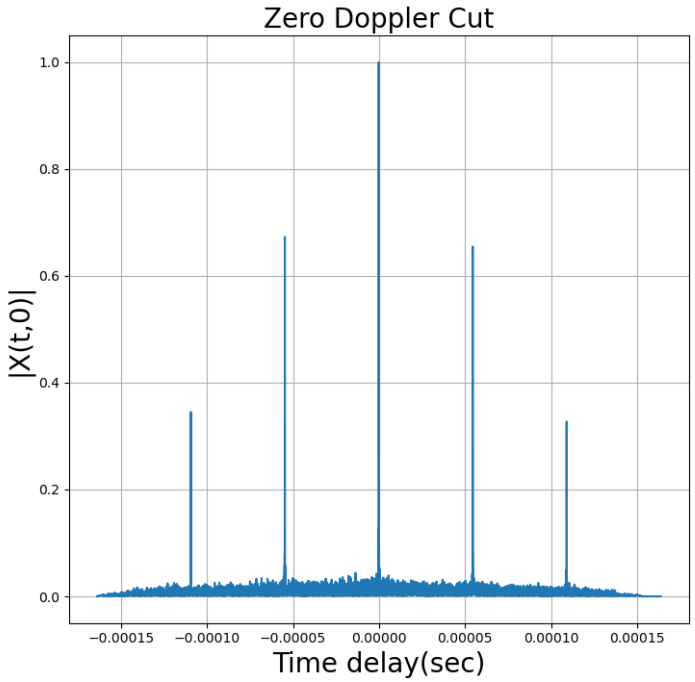

FIGURE A.20: Zero-Doppler cut of a LFM Train signal with SNR = -2.39 dB.

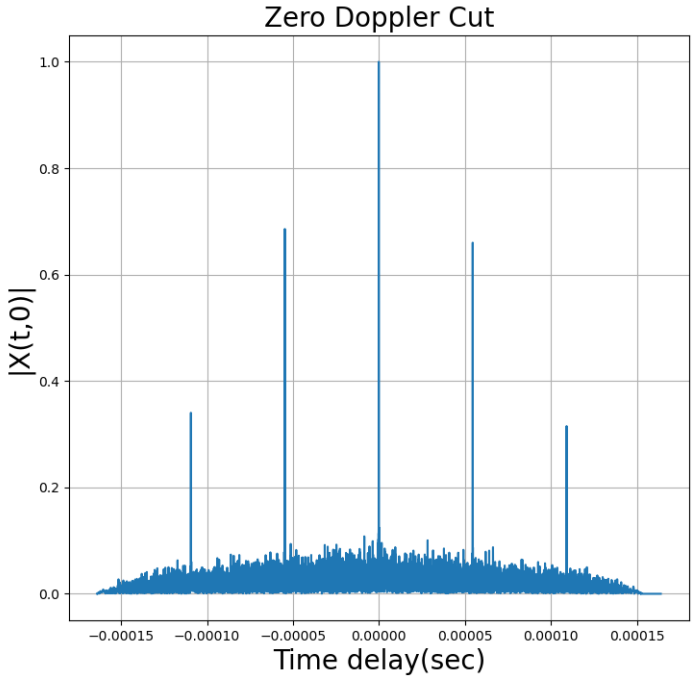

FIGURE A.21: Zero-Doppler cut of a LFM Train signal with SNR = -11.48 dB.

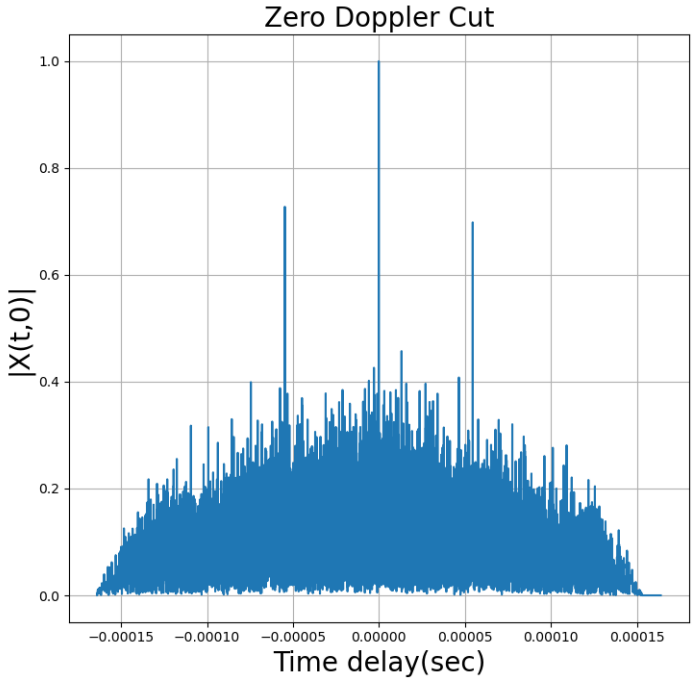

FIGURE A.22: Zero-Doppler cut of a LFM Train signal with SNR = -21.47 dB.

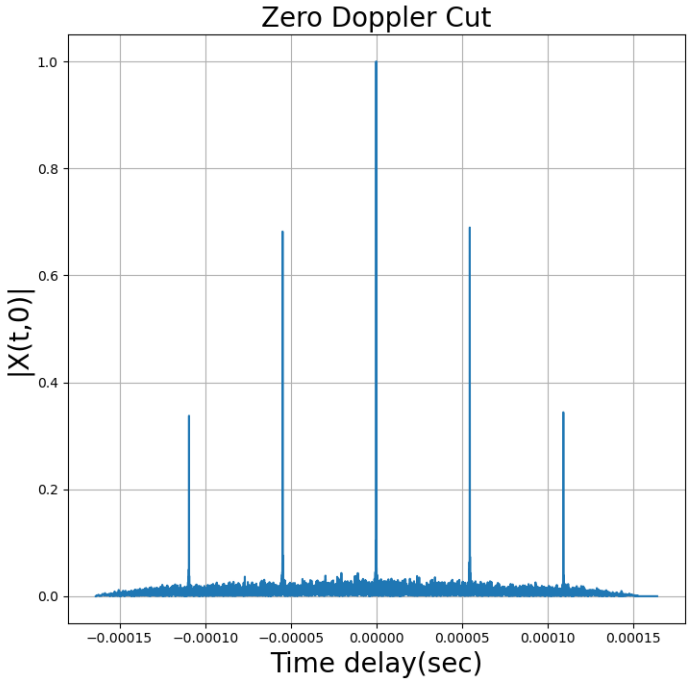

FIGURE A.23: Zero-Doppler cut of a LFM Train signal with SNR = -2.39 dB.

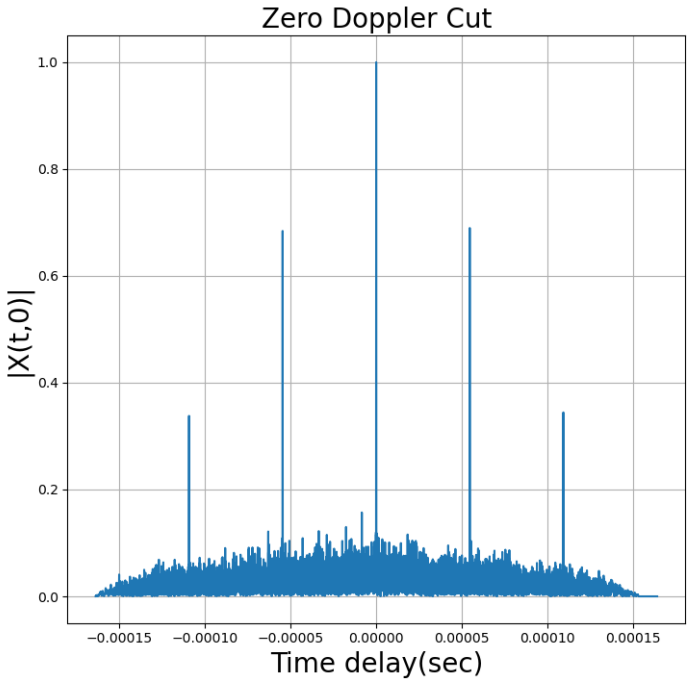

FIGURE A.24: Zero-Doppler cut of a LFM Train signal with SNR = -11.47 dB.

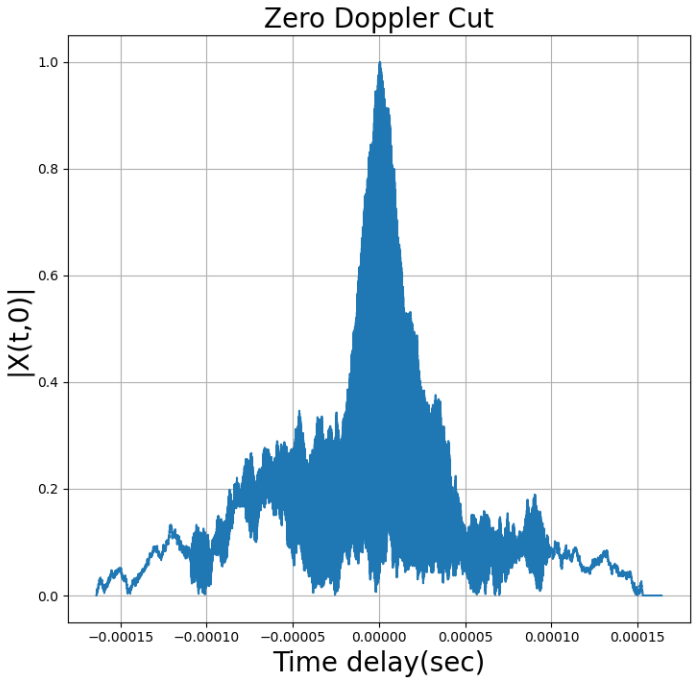

FIGURE A.25: Zero-Doppler cut of a Stepped FM signal with SNR = -21.48 dB.

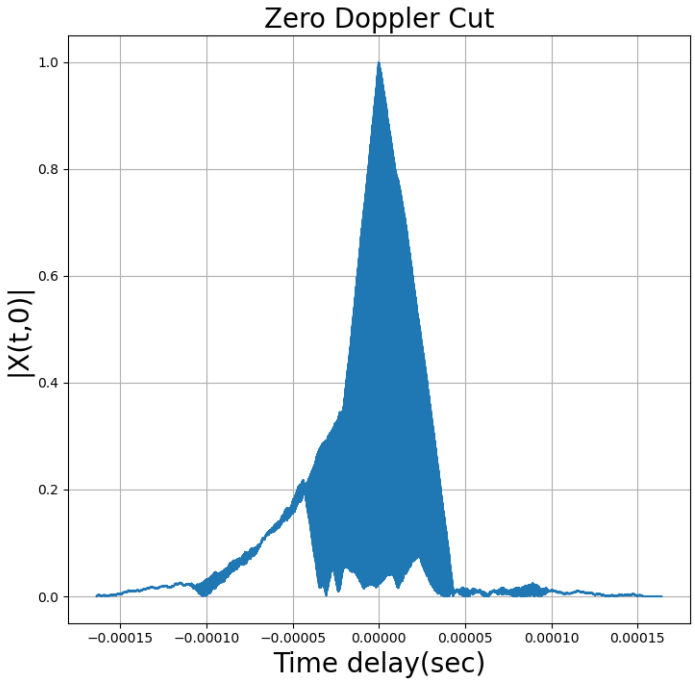

FIGURE A.26: Zero-Doppler cut of a Stepped FM signal with SNR = -2.39 dB.

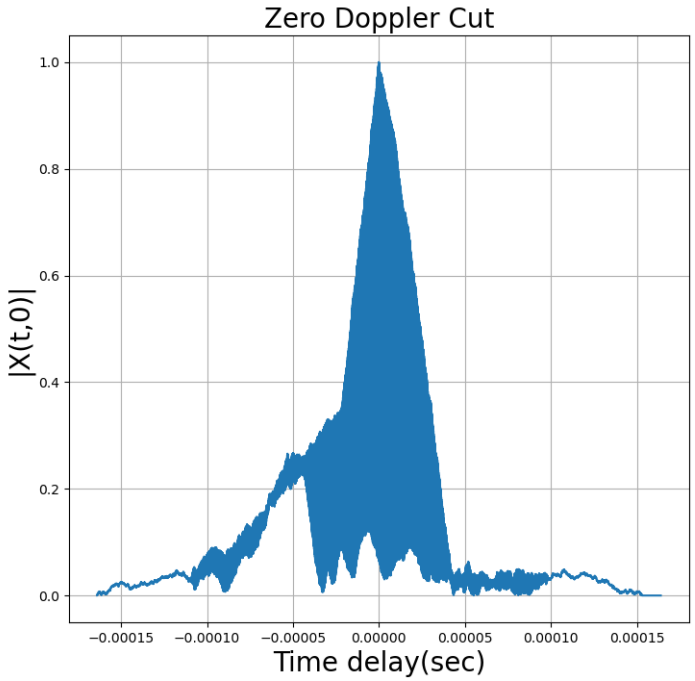

FIGURE A.27: Zero-Doppler cut of a Stepped FM signal with SNR = -11.48 dB.

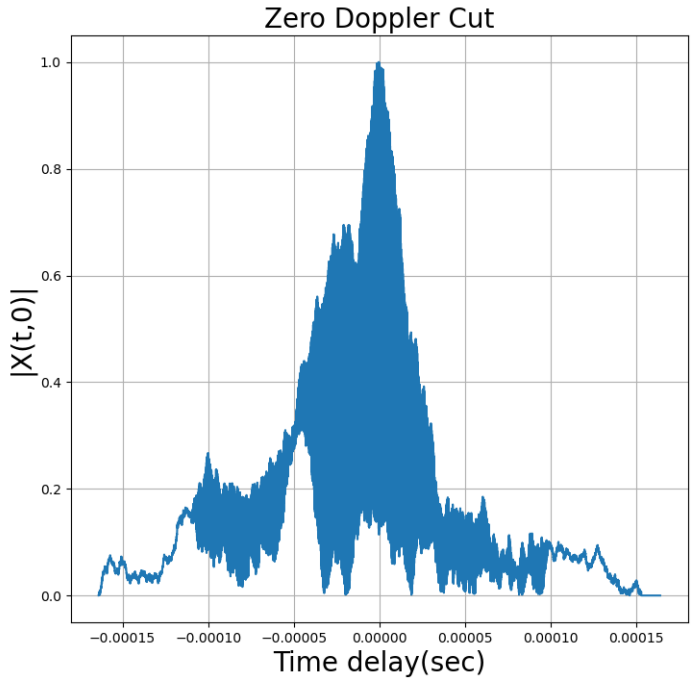

FIGURE A.28: Zero-Doppler cut of a Stepped FM signal with SNR = -21.47 dB.

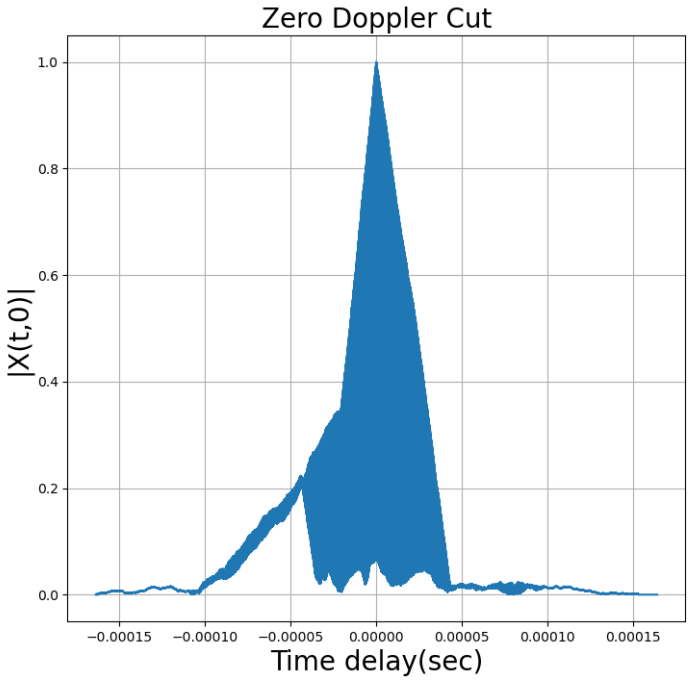

FIGURE A.29: Zero-Doppler cut of a Stepped FM signal with SNR = -2.39 dB.

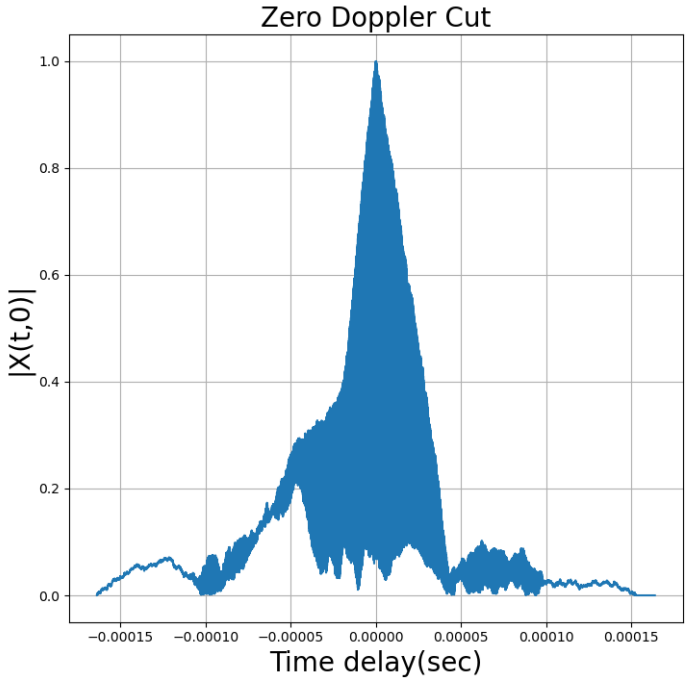

FIGURE A.30: Zero-Doppler cut of a Stepped FM signal with SNR = -11.47 dB.

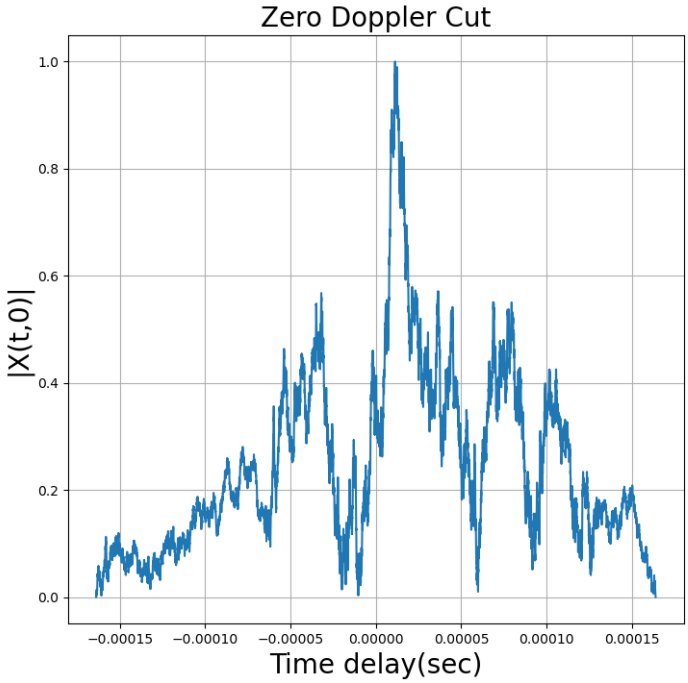

FIGURE A.31: Zero-Doppler cut of a Barker5 signal with SNR = -33.24 dB.

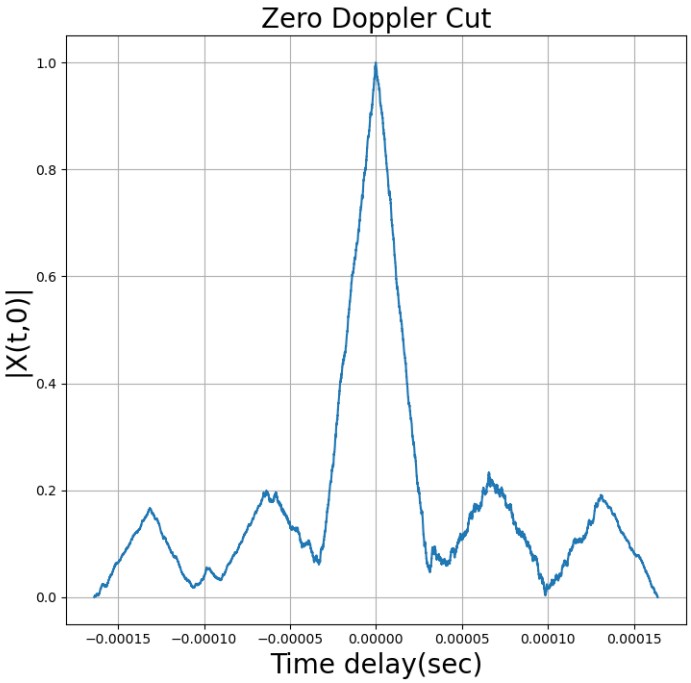

FIGURE A.32: Zero-Doppler cut of a Barker5 signal with SNR = -14.15 dB.

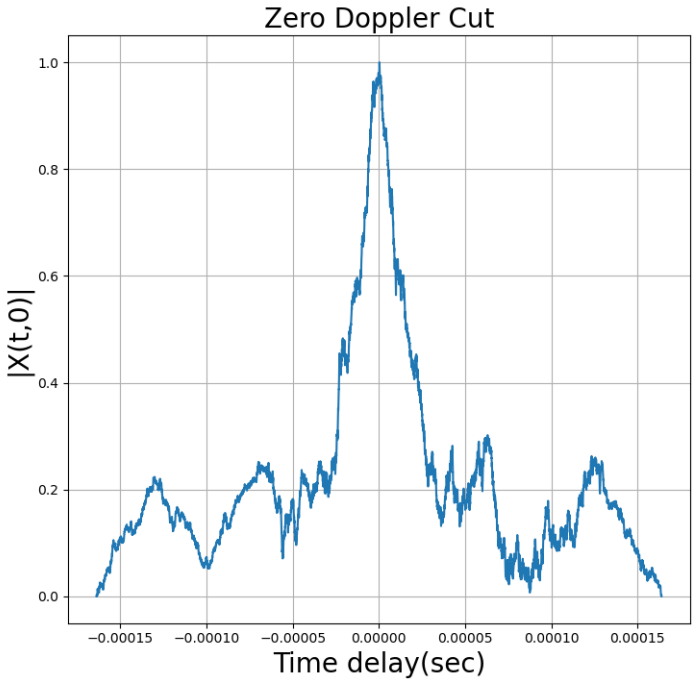

FIGURE A.33: Zero-Doppler cut of a Barker5 signal with SNR = -23.24 dB.

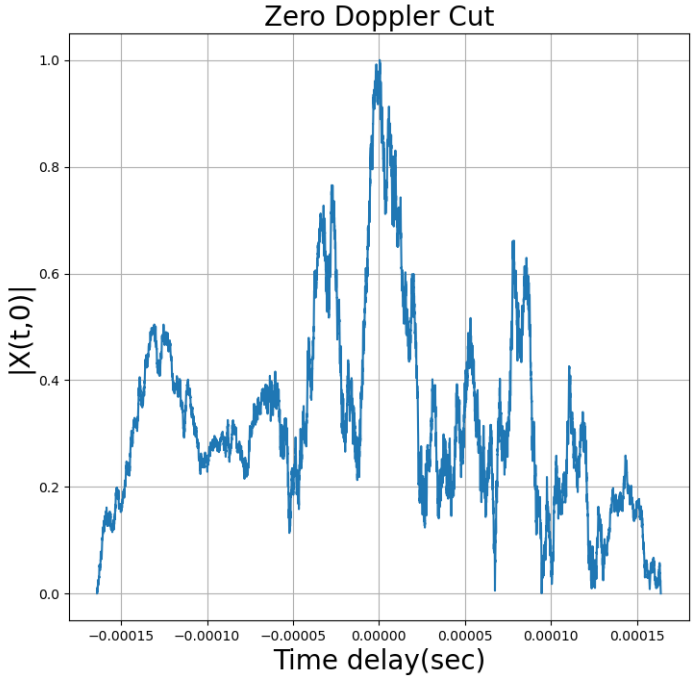

FIGURE A.34: Zero-Doppler cut of a Barker5 signal with SNR = -33.23 dB.

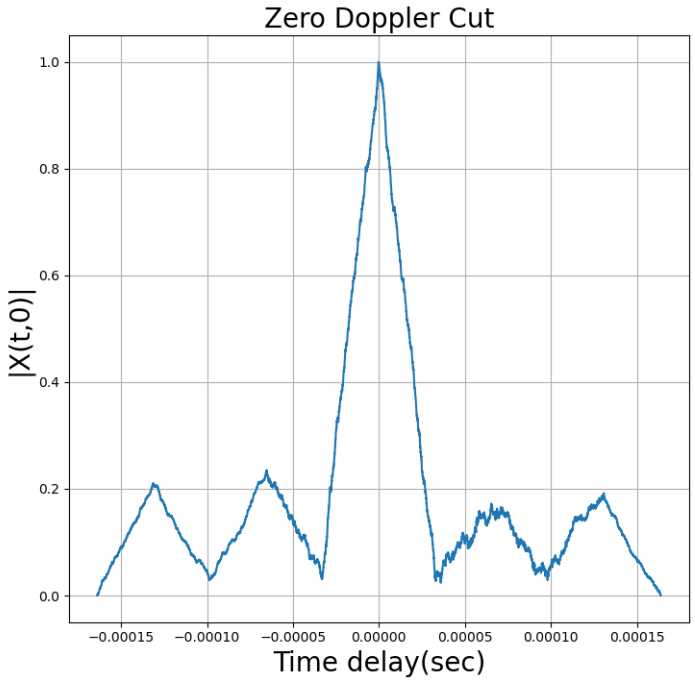

FIGURE A.35: Zero-Doppler cut of a Barker5 signal with SNR = -14.15 dB.

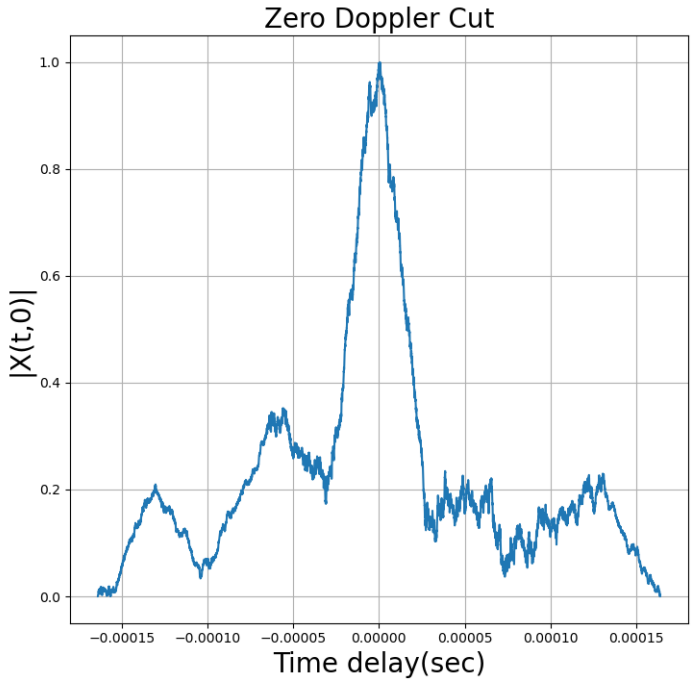

FIGURE A.36: Zero-Doppler cut of a Barker5 signal with SNR = -23.23 dB.

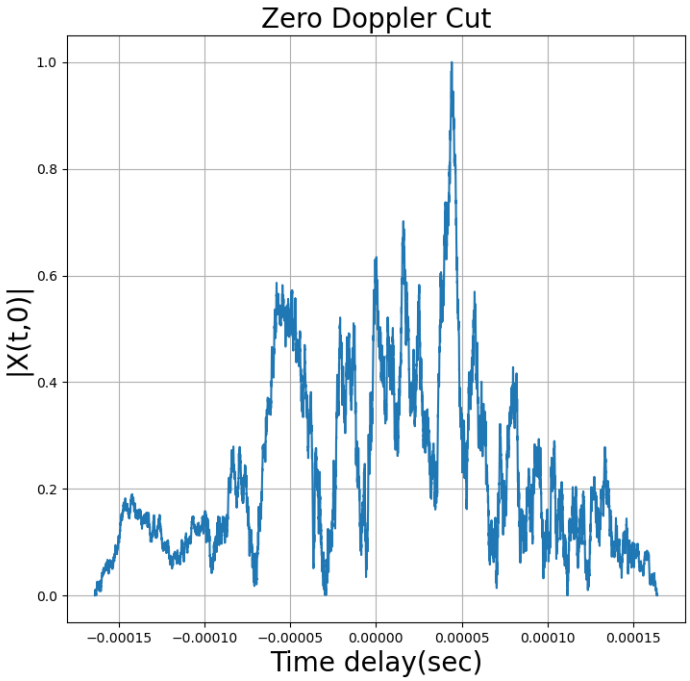

FIGURE A.37: Zero-Doppler cut of a Barker13 signal with SNR = -33.24 dB.

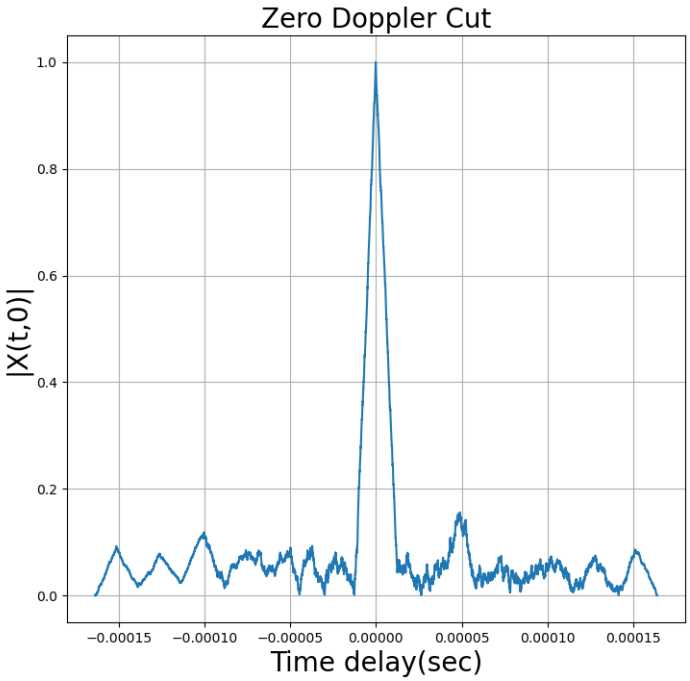

FIGURE A.38: Zero-Doppler cut of a Barker13 signal with SNR = -14.15 dB.

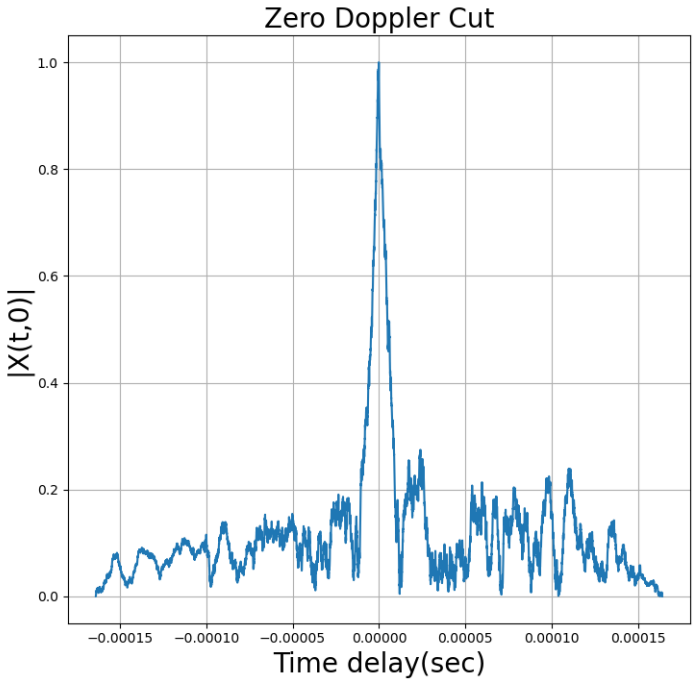

FIGURE A.39: Zero-Doppler cut of a Barker13 signal with SNR = -23.24 dB.

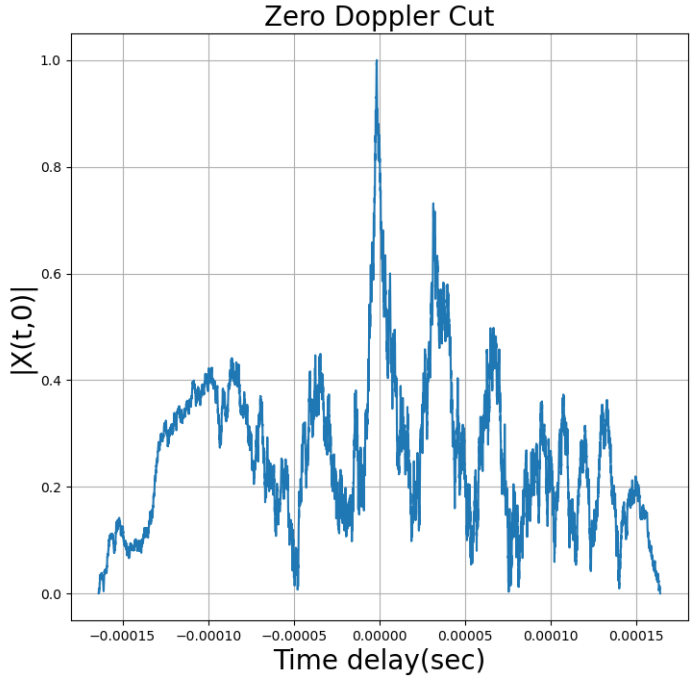

FIGURE A.40: Zero-Doppler cut of a Barker13 signal with SNR = -33.23 dB.

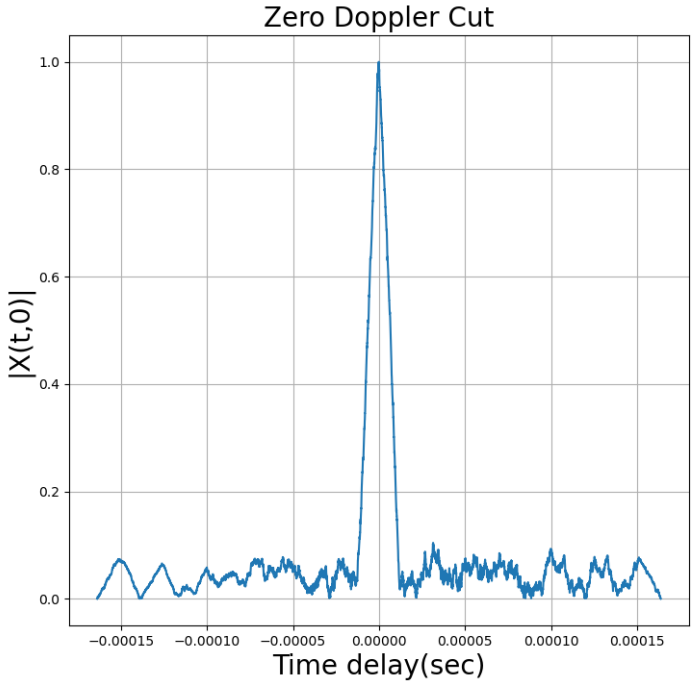

FIGURE A.41: Zero-Doppler cut of a Barker13 signal with SNR = -14.15 dB.

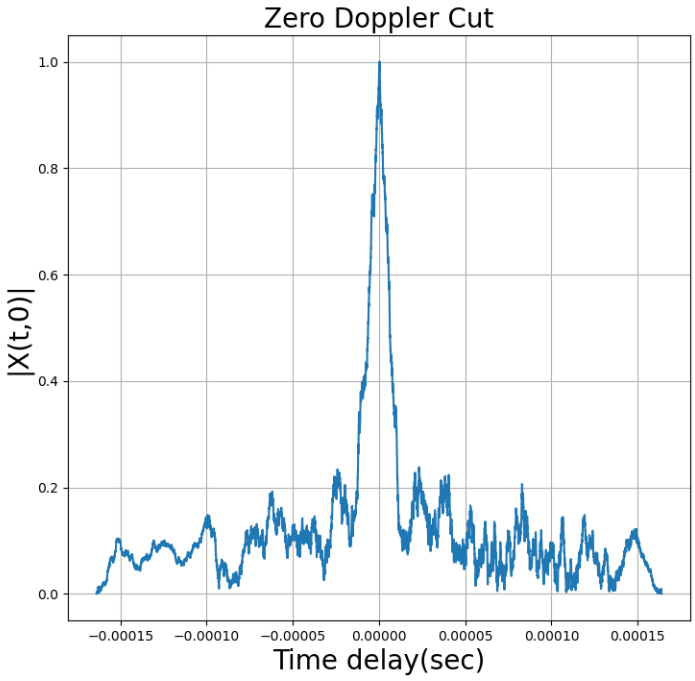

FIGURE A.42: Zero-Doppler cut of a Barker13 signal with SNR = -23.23 dB.

Annex I - Oxygen and Water Vapour Spectroscopic Data

Spectroscopic data for oxygen attenuation

f_0	a_1	a_2	a_3	a_4	a_5	a_6
50.474214	0.975	9.651	6.690	0.0	2.566	6.850
50.987745	2.529	8.653	7.170	0.0	2.246	6.800
51.503360	6.193	7.709	7.640	0.0	1.947	6.729
52.021429	14.320	6.819	8.110	0.0	1.667	6.640
52.542418	31.240	5.983	8.580	0.0	1.388	6.526
53.066934	64.290	5.201	9.060	0.0	1.349	6.206
53.595775	124.600	4.474	9.550	0.0	2.227	5.085
54.130025	227.300	3.800	9.960	0.0	3.170	3.750
54.671180	389.700	3.182	10.370	0.0	3.558	2.654
55.221384	627.100	2.618	10.890	0.0	2.560	2.952
55.783815	945.300	2.109	11.340	0.0	–1.172	6.135
56.264774	543.400	0.014	17.030	0.0	3.525	–0.978
56.363399	1331.800	1.654	11.890	0.0	–2.378	6.547
56.968211	1746.600	1.255	12.230	0.0	–3.545	6.451
57.612486	2120.100	0.910	12.620	0.0	–5.416	6.056
58.323877	2363.700	0.621	12.950	0.0	–1.932	0.436
58.446588	1442.100	0.083	14.910	0.0	6.768	–1.273
59.164204	2379.900	0.387	13.530	0.0	–6.561	2.309
59.590983	2090.700	0.207	14.080	0.0	6.957	–0.776
60.306056	2103.400	0.207	14.150	0.0	–6.395	0.699
60.434778	2438.000	0.386	13.390	0.0	6.342	–2.825
61.150562	2479.500	0.621	12.920	0.0	1.014	–0.584
61.800158	2275.900	0.910	12.630	0.0	5.014	–6.619
62.411220	1915.400	1.255	12.170	0.0	3.029	–6.759
62.486253	1503.000	0.083	15.130	0.0	–4.499	0.844
62.997984	1490.200	1.654	11.740	0.0	1.856	–6.675
63.568526	1078.000	2.108	11.340	0.0	0.658	–6.139
64.127775	728.700	2.617	10.880	0.0	–3.036	–2.895
64.678910	461.300	3.181	10.380	0.0	–3.968	–2.590
65.224078	274.000	3.800	9.960	0.0	–3.528	–3.680
65.764779	153.000	4.473	9.550	0.0	–2.548	–5.002
66.302096	80.400	5.200	9.060	0.0	–1.660	–6.091
66.836834	39.800	5.982	8.580	0.0	–1.680	–6.393
67.369601	18.560	6.818	8.110	0.0	–1.956	–6.475
67.900868	8.172	7.708	7.640	0.0	–2.216	–6.545
68.431006	3.397	8.652	7.170	0.0	–2.492	–6.600
68.960312	1.334	9.650	6.690	0.0	–2.773	–6.650
118.750334	940.300	0.010	16.640	0.0	–0.439	0.079
368.498246	67.400	0.048	16.400	0.0	0.000	0.000
424.763020	637.700	0.044	16.400	0.0	0.000	0.000
487.249273	237.400	0.049	16.000	0.0	0.000	0.000
715.392902	98.100	0.145	16.000	0.0	0.000	0.000
773.839490	572.300	0.141	16.200	0.0	0.000	0.000
834.145546	183.100	0.145	14.700	0.0	0.000	0.000

Source: Obtained from [20]

Spectroscopic data for water vapour attenuation

f_0	b_1	b_2	b_3	b_4	b_5	b_6
22.235080	.1079	2.144	26.38	.76	5.087	1.00
67.803960	.0011	8.732	28.58	.69	4.930	.82
119.995940	.0007	8.353	29.48	.70	4.780	.79
183.310087	2.273	.668	29.06	.77	5.022	.85
321.225630	.0470	6.179	24.04	.67	4.398	.54
325.152888	1.514	1.541	28.23	.64	4.893	.74
336.227764	.0010	9.825	26.93	.69	4.740	.61
380.197353	11.67	1.048	28.11	.54	5.063	.89
390.134508	.0045	7.347	21.52	.63	4.810	.55
437.346667	.0632	5.048	18.45	.60	4.230	.48
439.150807	.9098	3.595	20.07	.63	4.483	.52
443.018343	.1920	5.048	15.55	.60	5.083	.50
448.001085	10.41	1.405	25.64	.66	5.028	.67
470.888999	.3254	3.597	21.34	.66	4.506	.65
474.689092	1.260	2.379	23.20	.65	4.804	.64
488.490108	.2529	2.852	25.86	.69	5.201	.72
503.568532	.0372	6.731	16.12	.61	3.980	.43
504.482692	.0124	6.731	16.12	.61	4.010	.45
547.676440	.9785	.158	26.00	.70	4.500	1.00
552.020960	.1840	.158	26.00	.70	4.500	1.00
556.935985	497.0	.159	30.86	.69	4.552	1.00
620.700807	5.015	2.391	24.38	.71	4.856	.68
645.766085	.0067	8.633	18.00	.60	4.000	.50
658.005280	.2732	7.816	32.10	.69	4.140	1.00
752.033113	243.4	.396	30.86	.68	4.352	.84
841.051732	.0134	8.177	15.90	.33	5.760	.45
859.965698	.1325	8.055	30.60	.68	4.090	.84
899.303175	.0547	7.914	29.85	.68	4.530	.90
902.611085	.0386	8.429	28.65	.70	5.100	.95
906.205957	.1836	5.110	24.08	.70	4.700	.53
916.171582	8.400	1.441	26.73	.70	5.150	.78
923.112692	.0079	10.293	29.00	.70	5.000	.80
970.315022	9.009	1.919	25.50	.64	4.940	.67
987.926764	134.6	.257	29.85	.68	4.550	.90
1 780.000000	17506.	.952	196.3	2.00	24.15	5.00

Source: Obtained from [20]

Annex II - Vertical Profiles of the Atmosphere

For summer, the temperature T(K) at a height h(km) is given by:

- $T(h) = 294.9838 - 5.2159h - 0.0710h^2 \quad for \quad 0 \leq h < 13$
- $T(h) = 215.15 \quad for \quad 13 \leq h < 17$
- $T(h) = 215.15 \cdot exp[(h-17)0.008128] \quad for \quad 17 \leq h < 47$
- $T(h) = 275 \quad for \quad 47 \leq h < 53$
- $T(h) = 275 + [1 - exp((h-53)0.06)]20 \quad for \quad 53 \leq h < 80$
- $T(h) = 175 \quad for \quad 80 \leq h \leq 100$

For the dry air pressure P(hPa):

- $P(h) = 1012.8186 - 111.5569h + 3.8646h^2 \quad for \quad 0 \leq h \leq 10$
- $P(h) = P_{10} \cdot exp[-0.147(h-10)] \quad for \quad 10 < h \leq 47$
- $P(h) = P_{72} \cdot exp[-0.165(h-72)] \quad for \quad 72 < h \leq 100$

where P_{10} and P_{72} are the dry air pressures at 10km and 72km, respectively.

Lastly, the water vapour density $\rho(\mathrm{g\,m^{-3}})$ is given by:

- $\rho(h) = 14.3542exp[-0.4174h - 0.02290h^2 + 0.001007h^3] \quad for \quad 0 \leq h \leq 15$
- $\rho(h) = 0 \quad for \quad h > 15$

Similarly for winter, the temperature T(K) at a height h(km) is given by:

- $T(h) = 272.7241 - 3.6217h - 0.1759h^2 \quad for \quad 0 \leq h < 10$
- $T(h) = 218 \quad for \quad 10 \leq h < 33$
- $T(h) = 218 + (h-33)3.3571 \quad for \quad 33 \leq h < 47$
- $T(h) = 265 \quad for \quad 47 \leq h < 53$
- $T(h) = 265 - (h-53)2.0370 \quad for \quad 53 \leq h < 80$
- $T(h) = 210 \quad for \quad 80 \leq h \leq 100$

For the dry air pressure P(hPa):

- $P(h) = 1018.8627 - 124.2954h + 4.8307h^2 \quad for \quad 0 \leq h \leq 10$
- $P(h) = P_{10} \cdot exp[-0.147(h-10)] \quad for \quad 10 < h \leq 47$

- $P(h) = P_{72} \cdot exp[-0.155(h - 72)] \qquad for \quad 72 < h \leq 100$

  where P_{10} and P_{72} are the dry air pressures at 10km and 72km, respectively.

  Lastly, the water vapour density $\rho(\mathrm{g\,m^{-3}})$ is given by:

- $\rho(h) = 3.4742exp[-0.2697h - 0.03604h^2 + 0.0004489h^3] \qquad for \quad 0 \leq h \leq 10$
- $\rho(h) = 0 \qquad for \quad h > 10$